Master's thesis

NTNU
Norwegian University of Science and Technology
Faculty of Engineering
Department of Civil and Environmental Engineering

Sarah Theresa Heller

A Numerical Simulation of Permafrost Thermal Regime under a Heat Pump Chilled Foundation in Longyearbyen, Svalbard

Master's thesis in Civil Engineering and Cold Climate Engineering
Supervisor: Thomas Ingeman-Nielsen (DTU), Aleksey Shestov (UNIS), Rao Martand Singh (NTNU)

July 2021

NTNU
Norwegian University of Science and Technology

DTU Cold Climate Engineering
UNIS

Sarah Theresa Heller

A Numerical Simulation of Permafrost Thermal Regime under a Heat Pump Chilled Foundation in Longyearbyen, Svalbard

Master's thesis in Civil Engineering and Cold Climate Engineering
Supervisor: Thomas Ingeman-Nielsen (DTU), Aleksey Shestov (UNIS), Rao Martand Singh (NTNU)
July 2021

Norwegian University of Science and Technology
Faculty of Engineering
Department of Civil and Environmental Engineering

NTNU
Norwegian University of Science and Technology

Preface

This master's thesis is based on the knowledge and interest gained during the Nordic Master in Cold Climate Engineering. The study is conducted at the University Centre in Svalbard (UNIS) in collaboration with NTNU in Trondheim and DTU in Copenhagen. Three supervisors are part of this project, namely Aleksey Shestov (UNIS), Rao Martand Singh (NTNU) and Thomas Ingeman-Nielsen (DTU). The idea of studying the thermal regime under a heat pump chilled foundation was formed in discussions with Aleksey Shestov and Lars Olav Grande (Norconsult AS) in light of an ongoing construction project, implementing the largest cooling plate in Longyearbyen to date. The collaboration of many stakeholders, such as Longyearbyen Lokalstyre, Norconsult AS and CONSTO AS, have made this study possible.

Longyearbyen, 2021-07-20

Sarah Theresa Heller

Acknowledgment

I would like to thank my UNIS supervisor, Aleksey Shestov, for brainstorming the simulation approach and for valuable discussions during the development of the model. I would also like to thank my NTNU supervisor, Rao Martand Singh, for his support during the master's thesis. I am also grateful to Rainer-Helge Braun for providing access to project relevant data and for allowing me to access the construction site. Furthermore, my sincerest gratitude goes to Lars Olav Grande who made this project possible, provided encouragement and support along the way and always showed interest in this study.

My deepest gratitude goes to my DTU supervisor, Thomas Ingeman-Nielsen, who has opened up a new field of interest and enthusiasm for me during my studies. The motivation to conduct a master's thesis related to permafrost, is primarily due to his course, taught in Greenland at ARTEK, and the special course I conducted under his supervision at DTU. I also want to express my greatest appreciation to him for the possibility to assist Johanna Scheer's fieldwork in Greenland, which has allowed me to broaden my horizon and achieve a better understanding for frozen ground and the built environment. Overall, I would like to thank him for the support and guidance during the entire master's programme and lately during my thesis work, which has always turned my frustration into enthusiasm.

I cannot begin to express my thankfulness to Gunvor Marie Kirkelund, the head of studies of the Cold Climate Engineering master's programme. She has been a tremendous support during these past two years, which has made my studies as unique and valuable as I could possibly imagine them to be. At this point I would also like to highly acknowledge the endless support from Teit Groth during my time in Greenland at ARTEK. Especially during the often confusing times of a pandemic, the effort and time he spent to make the teaching and the entire experience in the Arctic so incredibly worthwhile and memorable has not gone unnoticed.

Also, the biggest possible thank you to Piitu and Renato for their endless support along the way and with whom I share so many profound memories of the Arctic. Thank you for countless hours spent in the office, for so many helpful discussions, for IT and mental support, for always looking out for me and for so much more.

And last but certainly not least, I would like to express my endless gratitude to my parents, Barbara and Ralf, and to my sister, Elena, for showing so much interest in my studies and for countless constructive discussions along the way. I want to express my sincerest appreciation for motivating me, supporting me, believing in me, especially when I stop believing,

and for the encouragement to go the extra mile. I want to especially highlight the efforts my mum made during these last months. This thesis could not be of the same quality without her critical scientific thinking, which lead to countless valuable discussions, and her constructive input regarding the structure of this report. Finally, I can not begin to express my gratitude to her for proof reading the entire thesis so thoroughly.

S.H.

Abstract

Climate change in the Arctic causes a critical warming of the permanently frozen subsoil. The livelihood of over 3 million people is affected by the projected degradation of permafrost until 2050. The sustainable development of permafrost regions must address the need for special foundation solutions to found structures on steadily warming ground. The thermal regime is disturbed when a structure is placed on permafrost. Heat loss through the floor of the building can cause major degradation of frozen ground. Tailored permafrost engineering solutions are available to mitigate the effects of climate change and local human-induced warming on the subsoil. Modern solutions aim to maintain the thermal regime in the subsoil and thus mitigate frost heave and thaw settlements in the ground. Freeze-thaw action can lead to a loss of structural integrity as the soil's strength highly decreases upon thawing and pore water expands 9% upon freezing.

An attractive foundation solution in view of climate change lies in the active cooling of the subsoil under a structure. The ground source heat pump technology, widely used in milder climates as a source of renewable energy, is adapted to permafrost application to permanently keep the ground frozen. A heat-pump powered system extracts heat from the ground via ground loops and a heat carrier fluid. The heat lost through the floor of the building can be extracted from the ground and the soil can further be cooled to a desired temperature. The active control of the systems enables to adapt the system to changing climatic conditions.

This study focuses on a current heat-pump cooling project in Longyearbyen, the largest settlement in Svalbard. A foundation area of 3 400 m² is permanently cooled during the lifetime of the building. A verified 3D model is built to simulate the ground's thermal regime under a cooling plate. The results identify the corner area close to the ocean as the most critical area with the warmest ground temperatures. A cooling temperature of -5 °C is risky, especially in view of climate warming and it is found that a temperature of -10 °C is more suitable for the project. An estimate of annual operational expenses concludes that the cost lies between 16 000 and 54 000 NOK, dependent on the heat-pump efficiency and the cooling temperature. A well-controlled monitoring system is an integral part of this technology to avoid undetected power failure which is found to warm the ground by 4 °C in one year.

The technology can be optimized in different ways. The study of seasonal operation shows that the ground remains frozen also when the cooling system is turned off for three consecutive months in winter. This implies that the system can be turned off during some

months in the darker seasons and powered with solar energy in warmer seasons. These results consequently highlight the development possibility to a self-sustained cooling system which can be coupled with a renewable energy source, such as solar energy, to power the system.

Contents

Preface i

Acknowledgment ii

Abstract iv

Table of Contents vi

List of Figures xv

List of Tables xvii

1 Introduction **1**

1.1 Aim and Objectives 3

1.2 Approach 4

1.3 Limitations 4

1.4 Structure of the Report 5

2 Background **6**

2.1 Permafrost in Svalbard 6

2.2 Permafrost Ground Thermal Regime 8

2.3 Permafrost Warming and its Effects 17

2.4 Heat Pump Cooled Foundations 22

2.5 Summary and Research Gaps 30

3 Methodology **32**

3.1 Finite Element Analysis 32

3.2 Verification and Validation of Models 36

4 Main Characteristics of the Study Site Miljøstasjon in Longyearbyen **39**

4.1 Project Overview 39

4.2 Temperature Data 44

4.3 Climate Data 51

4.4 Summary 55

5 Calibration and Operational Validation of the Model 57

5.1 1D Model: Soil Properties 57

5.2 2D Model: Geometry, Forcing Data and Initial Condition 63

5.3 3D Model 76

5.4 Summary 86

6 Numerical Simulations of Relevant Scenarios 88

6.1 General 89

6.2 Behaviour of the Ground under a Cooling Plate 91

6.3 Seasonal Cooling of the Plate 102

6.4 Power Failure 105

6.5 Effects of Climate Change 108

6.6 Limitations 116

7 Summary and Conclusions 118

7.1 Discussion 119

7.2 Recommendations for Further Work 121

A Acronyms 122

B Additional Information 124

B.1 Thermal Properties from Literature 124

B.2 Construction Drawings 125

B.3 Calibration of Soil Properties 127

B.4 Thermal Model Days 129

B.5 Model Performance in the Upper 5 Metres 135

B.6 Temperature Regime for a Cooling Temperature of -5 °C 140

Bibliography 142

List of Figures

2.1 Spatial permafrost distribution in the Northern Hemisphere (Jaroslav et al., 2019). 7
2.2 Map of permafrost distribution in Svalbard archipelago; shaded grey areas are underlain by permafrost (Humlum et al., 2003). 8
2.3 The valley Longyeardalen in which Longyearbyen is located, confined by mountain plateaus and Larsbreen and Longyearbreen glacier (Hanssen-Bauer et al., 2019). 9
2.4 (a) A schematic representation of the thermal regime in permafrost and its parameters (Burke et al., 2020); (b) Simplified representation of the seasonal sinusoidal trend of air temperature and the grounds response showing the delay of the ground response to the surface temperature (Andersland and Ladanyi, 2004). 10
2.5 Three types of heat transfer; ϑ stands for temperature and $\dot{Q}$ for heat flow (Boeckh and Wetzel, 2018). 12
2.6 Heat transfer processes in soils dependent on the degree of saturation and soil type (Vieira et al., 2017). 13
2.7 Long-term time series of mean annual air temperature from numerous weather stations around Svalbard showing a consistent warming trend (Hanssen-Bauer et al., 2019). 19
2.8 Mean annual ground temperatures for various permafrost monitoring locations on Svalbard showing a warming trend (Hanssen-Bauer et al., 2019). 19
2.9 Results from an experimental investigation showing the differences in permafrost distribution in the ground over a period of 26 years (Linell, 1973). 20
2.10 Illustration of a heat-pump system in heating mode coupled with a heat distribution system showing the integral parts of the system and the ongoing cycle to extract the heat from the HCF (QWare, nd). 23

2.11 Exemplary foundation designs in previous projects on Svalbard. 26
2.12 Photos of existing heat-pump cooling projects in Longyearbyen. They are all in operation except the house shown in (a) which is abandoned. 28

4.1 Overview of project site and conceptual illustration of the new environmental station. 40
4.2 Location of boreholes and thermistor strings respectively in relation to the foundation area marked by the blue rectangle. 41
4.3 Construction process of the foundation system, part 1; (photos retrieved online from the Interaxo database with the permission of Rainer-Helge Braun, Longyearbyen Lokalstyre). 42
4.4 Construction process of the foundation system, part 2 (photos retrieved online from the Interaxo Project Hotel with the permission of Rainer-Helge Braun, Longyearbyen Lokalstyre). 43
4.5 Photos of the thermistor string location in February 2021. The embankment at H1 was partially built at the time of the picture. 45
4.6 GeoPrecision thermistor string; data logger is integrated in the metal casing and thermistors are placed in variable spacing along the string (GeoPrecision, nd). 45
4.7 Contour plot of recorded temperature versus time with H2 (west) on top, H1 (east) in the middle and H4 (north) on the bottom. It is visible that the permafrost temperature at H2 and H1 are colder than at H4. 47
4.8 Estimation of active layer thickness and depth of zero annual amplitude in H2. 48
4.9 Temperature profiles in H2. 48
4.10 Estimation of active layer thickness and depth of zero annual amplitude in H1. 49
4.11 Thermal profile in H1. 49
4.12 Thermal profile in H4. 50
4.13 Comparison of maximum and minimum annual envelopes for H1 and H2 show that the ground thermal regime at H2 is colder than at H1 and DZAA and ALT are similar. 51
4.14 The comparison of measured air temperature from thermistor 1 in each borehole in blue, red and green respectively and air temperature recorded at the Svalbard Airport weather station in yellow. 52

4.15 Temperature measurements for the first, second and third sensor respectively at H2; it is concluded that it is reasonable that the second sensor is placed on the ground surface as the temperature variation is less pronounced than for the first sensor but also not fully smoothed, like sensor 3, indicating ground temperature. 53
4.16 Cumulative degree days for air and ground surface temperature with an indication for minimum and maxima in autumn 2019, spring 2020 and autumn 2020 respectively. 53
4.17 Measured ground surface temperature (GST) for the calibration period plotted against estimated GST using a n-factor modifier function. The r2 is 0.89 for the site, the modelled and estimated values agree well in thawing period. In freezing season a larger scatter is observed. 54

5.1 Spline function of measured ground surface temperature in H2, applied as upper boundary condition to calibrate soil properties. 58
5.2 1D model domain with initial condition set to temperature profile from 1st of October 2019 as measured on site. 59
5.3 Comparison of modelled temperature profile (green) and measured temperature profile (grey) for the first of each month for calibration analysis v08 (Oct 2019 - Feb 2020). 61
5.4 Comparison of modelled temperature profile (green) to measured temperature profile (grey) for the first of each month for calibration analysis v08 (Mar 2020 - Oct 2020). 62
5.5 Thermal functions for parameter set v08. 63
5.6 Illustration of the terrain and the simplified geometry for the model domain. . 64
5.7 Mean annual temperature variation for summer (Jul-Sep) and winter (Jan-May) in Isfjorden for the time period 1987-2017 (Skogseth et al., 2020). The upper numbering represent different sampling locations along a transect in Isfjorden and number 34 is situated close to Longyearbyen. 65
5.8 Adopted yearly sea temperature step function for the ocean bed boundary. Here depicted from Jan-Dec. The step function is adapted to the respective starting dates of an analysis. 66
5.9 Location of the two respective boreholes, TRT Measurements and Dh4-CO2-07, in relation to the project site. 68

5.10 (a) measurements for the TRT project show a warming effect in about 80 metres depth; (b) a negative heat flux is present until approximately 110 meter depth, a warming effect is observed below 120 metres (Midttoemme et al., 2015). . . . 69
5.11 2-dimensional geometry of the modelled cross-section; a finer mesh in the upper layer avoids numerical issues related to complex simulation of phase change. 70
5.12 Temperature field in the 2D domain after running a steady-state simulation. . . 71
5.13 Step function applied as upper ground surface boundary condition consisting of an average ground surface temperature dataset from 2014-2019. 72
5.14 Initial condition for the simulation compared to recorded temperature profiles in H2 and H1 respectively; the average root means squared error is 0.19 °C. . . . 73
5.15 Temperature distribution in the initial condition for 01 October 2019. 73
5.16 Step functions for the upper boundary condition forcing air and ground surface temperature for the three different scenarios. 74
5.17 Comparison of modelled (orange) and measured (red) annual temperature trumpets for location H2. 76
5.18 Illustration of the simplified foundation system for the simulation. 78
5.19 Conceptual sketch of 3D geometry and its dimensions, the upper sketch depicts a cross-section from west to east, the lower depiction is a bird view of the model domain with the sea in blue and the cooling plate in turquoise. 79
5.20 3D geometry in TEMP/W with respective mesh in each region. 79
5.21 Temperature field in the ground for the steady-state analysis and the subsequent warming in the transient analysis to establish the initial condition for 01 October 2019. 80
5.22 Mean monthly measured and modelled temperature profile for October 2019 until September 2020. 81
5.23 Comparison of modelled (green) and measured (black) mean monthly ground temperature profiles at H2 (Oct 19 - March 20). 82
5.24 Comparison of modelled (green) and measured (black) mean monthly ground temperature profiles at H2 (Apr 20 - Sept 20). 83
5.25 Comparison of modelled (green) and measured (black) mean monthly ground temperature profiles at H2 (Oct 20 - Dec 20). 84
5.26 Comparison of modelled (green) and measured (black) mean monthly ground temperature profiles at H1 (Oct 19 - March 20). 85

5.27 Comparison of modelled (green) and measured (black) mean monthly ground temperature profiles at H1 (Apr 20 - Sept 20). 86
5.28 Comparison of modelled (green) and measured (black) mean monthly ground temperature profiles at H4 (Apr 20 - Sept 20). 86

6.1 Conceptual sketch of the reference points relative to the foundation area. . . . 89
6.2 Applied forcing data for the land surface (left) and generated initial thermal regime for the natural terrain in December 2020 (right). 90
6.3 Comparison of the temperature profile used as initial condition for the model in December 2020. 91
6.4 Definitions for the numerical simulation of the ground's behaviour under a cooling plate. 92
6.5 Ground thermal regime after one year of cooling and ten years of cooling shows the development of the freezing front under the foundation area. 93
6.6 Temperature development in the ground under the plate in chosen depths for a cooling temperature of -5 °C. The highest fluctuation can be observed in P6 and P4, at the corner of the foundation area. P6 indicates that the corner facing the ocean, is the warmest area under the plate. P2 is cooled continuously, without influence from the ambient air, which results in a almost constant ground temperature close to -5 °C. 94
6.7 Annual temperature profile in P2 at T_p= -5 °C shows that the ground has already adapted to the cooling temperature in year 3. The longer the cooling is run, the more linear the temperature profile becomes, which is evident when comparing year 3 and year 10. The plate is indicated in grey until 1 metre depth. 95
6.8 Temperature profiles for at T_p= -5 °C; the plate is indicated in grey until 1 metre depth. 95
6.9 Ground temperature development under the foundation over time in chosen depths for a cooling temperature of -10 °C. The temperature at P2 cools constantly, a higher cooling effect can be observed at the start of the cooling until the ground. 97
6.10 Temperature profiles for T_p= -10 °C. The plate is indicated in grey. 98

6.11 Monthly temperature profiles at P2 for T_p=-10 °C for chosen years. (a) shows that the ground is still adjusting to the cooling temperature in year 03; after year 03 it becomes more stable with a steady cooling effect from the cooling temperature; the plate is indicated in grey. 98
6.12 Conceptual sketch of the foundation system on the underlying soil; Q_{tot} symbolizes the total heat extracted by the cooling system; Q_1 is the heat flowing from the building (T_i) towards the cooling plate (T_G), Q_2 is the heat flowing towards or away from the cooling pipes dependent on the season and thermal regime in the ground T_G. 99
6.13 Heat rate at the cooling pipe surface for T_p=-5 °C and -10 °C respectively. The negative sign shows that heat must be extracted. 100
6.14 Yearly operational cost dependent on the COP of the heat pump system for T_p=-5 °C and -10 °C. The price increases with decreasing cooling temperature. . 101
6.15 Difference in boundary condition for the seasonal cooling scenario. 103
6.16 Temperature evolution under the plate for different depths; 1 metre depth is at the bottom of foundation. The seasonal cooling is started at year 5 when a fluctuation in temperature can also be observed at P2 in the centre of the plate. 104
6.17 Temperature distribution in the model domain just before the cooling is turned off and turned back on again. 104
6.18 Cumulative energy transfer for a constant operation (orange) and a seasonal operation (yellow) shows that energy is saved during seasonal operation. 105
6.19 Temperature regime in P2 and P6 respectively during power failure of the heat-pump cooling system. 107
6.20 Temperature regime for the entire model domain in a power failure scenario for the cooling system. 107
6.21 Historic and projected mean annual air temperature for Svalbard Airport for different representative concentration pathways until 2072. The 30-year mean projection shows a warming up to 0 °C mean annual air temperature until 2072. 110

6.22 Projected mean monthly temperatures for RCP2.6 and RCP8.5 for different years at Svalbard Airport. The effect of natural variability is evident, e.g. July 2020 is warmer then July 2050. Also it is noticeable that the natural variability is repeated, e.g. variability from 2020 is repeated in 2040 and 2060, so every 20 years, as the temperature from the past 20 years is taken as a base and projected for the next decades. 111
6.23 Step function of mean monthly air temperature applied for the simulation from 2021-2072. 111
6.24 Projected change in monthly sea surface temperature for March in RCP4.5 scenario from 2010-2019 to 2060-2069 (Hanssen-Bauer et al., 2019). 112
6.25 Temperature profile in H2 for different years of the simulation shows extensive warming until 2072. 113
6.26 Minimum (left) and maximum (right) envelope in H2 for 2021 and 2072 shows that greater warming is experienced in winter than summer. 113
6.27 Thermal regime in 2026 and 2072 respectively; substantial warming of the adjacent ground is evident in winter and summer season. 114
6.28 Temperature profiles at P6 show that the most critical temperatures are experienced in August in the ground about half a meter under the plate. 115

B.1 Foundation design (retrieved online from the Interaxo project database with permission from Braun, R.-H.). 125
B.2 Foundation design (retrieved online from the Interaxo project database with permission from Braun, R.-H.). 125
B.3 Cooling pipe layout in the foundation design (retrieved online from the Interaxo project database with permission from Braun, R.-H.). 126
B.4 Modelled versus recorded ground temperature for the upper 5 metres in H2 (Oct 19 - Mar 20). 135
B.5 Modelled versus recorded ground temperature for the upper 5 metres in H2 (Apr 20 - Sep 20). 136
B.6 Modelled versus recorded ground temperature for the upper 5 metres in H2 (Oct 20 - Dec 20). 137
B.7 Modelled versus recorded ground temperature for the upper 5 metres in H1 (Oct 19 - Mar 20). 138

B.8 Modelled versus recorded ground temperature for the upper 5 metres in H2 (Apr 20 - Jul 20). 139
B.9 Modelled versus recorded ground temperature for the upper 5 metres in H4 (Nov 20 - Dec 20). 139
B.10 Visualization of the temperature field at different points in time from January to June after 10 years of cooling at -5 °C. 140
B.11 Visualization of the temperature field at different points in time from July to December after 10 years of cooling at -5 °C. 141

List of Tables

2.1 Values for n-factors measured in Arctic Alaska and Canada (Smith, 1996) 12
2.2 Heat pump cooling foundations in Svalbard with respective permafrost temperature extracted from Instanes and Rongved (2009). 26

3.1 Input parameters for TEMP/W for the respective thermal models, where n is porosity and T is temperature. 34

4.1 Placement of thermistors along the string: first sensor measures air temperature, second sensor measures ground surface temperature and ground temperature is measured down to 20 metres below top of the terrain. 46
4.2 Timeline of ground temperature measurements from thermistor strings in respective boreholes. 46
4.3 Comparison of the ALT, DZAA and ground temperature for the three temperature profiles at the project site. 51

5.1 Summary of constant thermal properties for the silty sand adopted from (Andersland and Ladanyi, 2004) and assumed saturation of the soil. 60
5.2 Calibration of soil properties with different combinations of soil properties; v08 shows the best fit;the simulation for v08 was rerun including a surface layer which improved the RMSE. 60
5.3 Set of soil properties for parameter set v08 resulting in the most accurate model results. 63
5.4 Initial condition chosen for further modelling shows 0.19 C error between modelled and recorded temperature. 73
5.5 Comparison of measured and modelled ALT, DZAA, MAGT and MMGT at location H2. 75
5.6 Input parameters for foundation layers in the simulation. 78

5.7 Quantification of the model accuracy in respect to ALT, DZAA and MAGT at -20 metres for the indicated duration at the respective location. 81
5.8 Summary of produced RMSE for the total depth and for the upper 5 metres in respect to recorded mean monthly ground temperature for each location. . . . 82

6.1 Comparison of energy transfer and heat rate for a cooling temperature of T_p=-5 °C and -10 °C respectively. 100
6.2 Heat rate at different cooling temperatures; the negative sign indicates that heat is extracted from the ground; $\dot{Q}_{tot}$ is the total heat rate, $\dot{Q}_1$ is the fraction of heat rate caused by the building above and $\dot{Q}_2$ is the fraction caused by the adjacent ground. 101
6.3 Cost comparison for a 24-hour per day operation of the heat pump for T_p=-5 °C and -10 °C at different COPs. 102
6.4 Projected annual and seasonal temperature changes for 60 years from 1971-2000 from ESD for medium percentile at Svalbard Airport, values are taken from Hanssen-Bauer et al. (2019). 109
6.5 Calculated projected annual and seasonal temperature changes per 20 years from 1971-2000. 110
6.6 Average energy transfer and heat rate under climate warming for a simulation until 2072 and the difference in heat rate to conditions nowadays. 115

B.1 Selected thermal properties from literature shows a wide variation of thermal properties. 124
B.2 Thermal properties for soil parameter set v08. Temperature is given in positive values below freezing point of 0 °C. 127
B.3 List of days used for the thermal modelling (1/6). 129
B.4 List of days used for the thermal modelling (2/6). 130
B.5 List of days used for the thermal modelling (3/6). 131
B.6 List of days used for the thermal modelling (4/6). 132
B.7 List of days used for the thermal modelling (5/6). 133
B.8 List of days used for the thermal modelling (6/6). 134

Chapter 1

Introduction

In the Arctic region, the mean annual ground surface temperature is warming three times as fast as the global average, the ground surface temperature is projected to be as high as 10 °C for a high-emission scenario by 2100 (AMAP, 2021). Arctic permafrost has experienced a warming of 2 to 3 °C since the 1970s and the seasonally thawed top layer continues to extend deeper (AMAP, 2021; Hanssen-Bauer et al., 2019; Francis et al., 2017). In Svalbard, an archipelago situated in the Arctic Ocean with its islands ranging from 74 to 81° north, the impact on frozen ground is obvious as permafrost temperature is steadily increasing since 2000 (Hanssen-Bauer et al., 2019). Approximately 5 million people live on permafrost in the Arctic and around 70 % of infrastructure in the Arctic is situated in permafrost areas of high potential for degradation by 2050, which equals a number of 3.6 million affected people (Hjort et al., 2018).

But not only climate change, also human induced changes to the ground surface alongside construction of poorly designed and maintained structures and infrastructure lead to warming of permafrost. This in turn effects the structural integrity of buildings and infrastructure on permafrost (Sheshpari and Khalilzad, 2016). The majority of problems occur in areas of ice-rich, thaw unstable permafrost and areas of discontinuities in the frozen ground (Clarke, 2007). Special foundation solutions for permafrost regions need to address these issues. The appropriate solution depend on various factors such as soil type, permafrost condition, design loads and service life time to only name a few (Sheshpari and Khalilzad, 2016). The foundation techniques range from gravel pads, elevated buildings on pile foundations, passive thermosyphons cooling systems to active cooling systems (Perlshtein et al., 2001). Modern techniques aim to maintain the thermal regime in the ground and avoid thawing of permafrost. In light of climate change, for buildings with a long service life time

and high loads on warm, ice-rich and thaw-unstable permafrost, foundations with active cooling systems are found to be a technical and economical advantageous solution (Instanes and Rongved, 2019; Zarling and Yarmak, 2007; Instanes and Rongved, 2009). A heat pump cooling system, used since the 1980s in the Arctic (Goodrich and Plunkett, 1990), artificially freezes the ground by extracting heat. The extracted heat can further be utilized to heat the building itself.

Since 1986, heat pump cooling systems have been implemented at approximately six projects in Svalbard (Instanes and Instanes, 2008). Svalbard is underlain by continuous permafrost, thus infrastructure and buildings must be founded on frozen ground. Svalbard's largest settlement and administrative centre, Longyearbyen, developed from a coal-mining settlement, founded in the early 19th century, to an open community with around 2400 inhabitants in 2021 (Statistics Norway, nd). A large case history of damaged infrastructure and buildings on permafrost caused by improper design and/or climate change exists in Longyearbyen (Rongved and Instanes, 2012; Instanes and Rongved, 2019; Instanes, 2016; Instanes and Anisimov, 2008; Instanes and Mjureke, 2005; Statsbyg, nd).

Currently a new environmental station is constructed in Longyearbyen. In order to mitigate the effects of ground disturbance and ensure a stable foundation for the service lifetime the foundation is designed with a heat pump cooling system. The construction site is situated on a peninsula named Hotellneset, within 50 metres off the Adventfjord coastline. The area is characterized by warm, saline and ice-rich permafrost (Molmann et al., 1998). The thermal design for the building is very minimal and no modelling of the ground thermal regime has been done. The design cooling temperature is based on temperature readings from two thermistors installed prior to construction. The vicinity to the sea side can influence the temperature distribution under the plate as water bodies act as major heat sources (Van Huissteden, 2020; Humlum et al., 2003). Furthermore, the design service lifetime for the building is 50 years, but the behaviour of the ground under projected climate warming has not been studied. These reasons point out the necessity to investigate the ground thermal regime for this project in more detail.

This study becomes even more relevant in light of the new strategy announced by the Norwegian government to implement a comprehensive energy plan in the Svalbard Budget 2022. This includes the transition to a climate-friendly energy solution and a focus on energy optimization and efficiency in Longyearbyen. The long-term goal is to transition to renewable energy as the major source of energy for the town (Regjeringen, 2021). Currently

an EU funded pilot project for further development of the heat pump cooling system is under way in Longyearbyen. Its goal is to power the heat pump system with solar energy and couple it with means for energy storage for excess heat. The long-term aim is to develop an integrated system, that can be made available for other permafrost regions. However, insufficient knowledge about design, maintenance protocols and temperature measurements for existing projects are available for further development (Husdal, D.A., personal correspondence, 26 February 2021). In order to adapt the cooling temperature and transition the system to a more energy efficient solution, increased knowledge and measurements are needed (Mathisen, 2020).

All the aforementioned reasons make the heat pump cooling system a focus point for the future development and energy optimization strategy in Longyearbyen.

1.1 Aim and Objectives

The aim of this study is to simulate the ground thermal regime under the cooling plate of the Miljøstasjon project in Longyearbyen to provide an increased knowledge base for the operation and further development of heat-pump cooling systems. The behaviour of the ground under a cooled foundation plate as well as the performance under climate change scenarios for the service lifetime of 50 years for this project will be investigated. The overall aim is to contribute to the further development of this technology and the proper operation of the plate. The main objectives to achieve these goals are:

1. Provide an overview of permafrost thermal regime and its sensibility to climatic and human induced change and further introduce permafrost engineering solutions with a special focus on heat pump cooling systems.

2. Compile a data base containing project specific information such as soil properties, climate data, foundation design, etc. as a base for numerical modelling.

3. Build a verified finite element model validated by in-situ recorded ground temperature data.

4. Use the validated model to conduct numerical simulations of different scenarios. The aim is to investigate the ground's thermal behaviour in each scenario. Further on, the estimation of a minimum heat pump capacity and operational cost for some scenarios is proposed. Overall, the scenarios shall provide insight in the ground's thermal behaviour in view of a suitable cooling temperature and to identify important parameters

for the development towards a sustainable, energy efficient heat pump cooling technology for permafrost regions.

1.2 Approach

A desk study forms the base of this study to gather relevant project specific information such as climate data, soil properties, geometry of the foundation plate, elevation profile of the surrounding areas, etc. In combination with the desk study, meetings with the project leader, Rainer-Helge Braun from Lokalstyre, the design consultant, Lars Olav Grande from Norconsult AS, the operation engineer for Real Estates at Lokalstyre, Dag Arne Husdal, are held to gain access to project related data such as construction drawings, field investigation report, thermistor measurements, etc. Additionally, site visits are made to gather the recorded ground temperature data at the construction site, which is always performed in compliance with the contractor on site, CONSTO AS, and the project leader Rainer-Helge Braun from Lokalstyre. Numerical simulations are conducted based on all gathered information and verified by using the recorded ground temperature data. A sensitivity analysis is performed to identify the suitability of estimated seasonal n-factors to link air temperature to ground surface temperature. Further on, different scenarios are studied based on the verified model to determine a suitable cooling temperature for the plate. Also, a total power failure of the system will be modelled to investigate the effects on the ground. Particularly in view of sustainable development, an energy efficient cooling scheme will be investigated with possible 'no cooling' durations. Finally, a recommendation for cooling temperature of the plate incorporating future climate warming scenarios in the model will be given.

All figures adopted from other sources will be specified with its respective source. If no reference is given, the figure is produced by the author.

1.3 Limitations

Simplifications and assumptions need to be made in order to build the numerical model. Some originate from the nature of modelling, where real life situations need to achieve a reasonable computational time, and others are caused by the lack of site specific data. Also, uncertainties in projected future climate scenarios are inevitable and the projections in this study are further limited by its methodology, since climate data from climate models are not available to the author.

1.4 Structure of the Report

The report is structured as follows: Chapter 2 gives an introduction to heat transfer in soils, permafrost, its ground thermal regime as well as permafrost warming and its effects and implication for engineering. Further on, permafrost engineering in Longyearbyen is introduced, challenges and solutions are shortly discussed. Finally, the heat pump cooling system is reviewed in more detail and experiences from previous projects in Longyearbyen are summarized before pointing out research gaps in this field of research. Chapter 3 presents the methodology for the study as well as the validation and verification process for the model. Also, the implemented numerical software is discussed in more detail. Chapter 4 focuses on the key study and project relevant details such as its location, site conditions, foundation design, ground temperature records and available climate data are included. Chapter 5 addresses the calibration of the model, which includes the choice of geometry, soil properties, boundary conditions, the establishment of an initial condition and finally the testing of the model's performance. Chapter 6 presents the studied scenarios using the verified model and its results. The scenarios include optimal cooling temperature of the plate, seasonal cooling, power failure and climate warming scenarios. Chapter 7 summarizes the results of this study and gives an outlook and recommendations for further work to develop the heat pump cooling technology in the future.

Chapter 2

Background

This chapter introduces permafrost and its characteristics in Svalbard. Then, the theory of physical processes in the ground related to the permafrost thermal regime are presented. Further on, the causes and consequences of the disturbance of the thermal regime in the ground are discussed. Subsequently, implications of permafrost warming for engineering, its challenges and applied solutions for frozen ground are presented. The focus then lies on the heat pump cooling system and its previous application in Svalbard. At the end of the chapter research gaps are highlighted.

2.1 Permafrost in Svalbard

Permafrost or perennial frozen ground underlies a large extent of land and sea in the Northern Hemisphere (Brown et al., 1997; Jaroslav et al., 2019). Its distribution is classified in continuous and discontinuous permafrost zones as shown in Figure 2.1. A commonly used definition describes permafrost as the thermal condition in soil or rock of having temperatures below 0°C persist(ing) over at least two consecutive winters and the intervening summer (Brown and Kupsch, 1974). Also, the mean annual air temperature (MAAT) must be below 0 °C to secure the existence of permafrost.

Svalbard is situated in the continuous permafrost zone, although recent studies have raised concerns about degrading permafrost, creating local discontinuous zones in coastal areas of western Spitsbergen and in areas of lowland valleys (Jaroslav et al., 2019). Mean annual ground temperature in Svalbard lies between - 2.5 °C in coastal western areas and - 5 °C in central areas, resulting in the warmest permafrost at this latitude (Hanssen-Bauer et al., 2019). The permafrost distribution on Spitsbergen, the largest island of the Svalbard archipelago, is shown in Figure 2.2, around 60% of the land area is glaciated and apart from

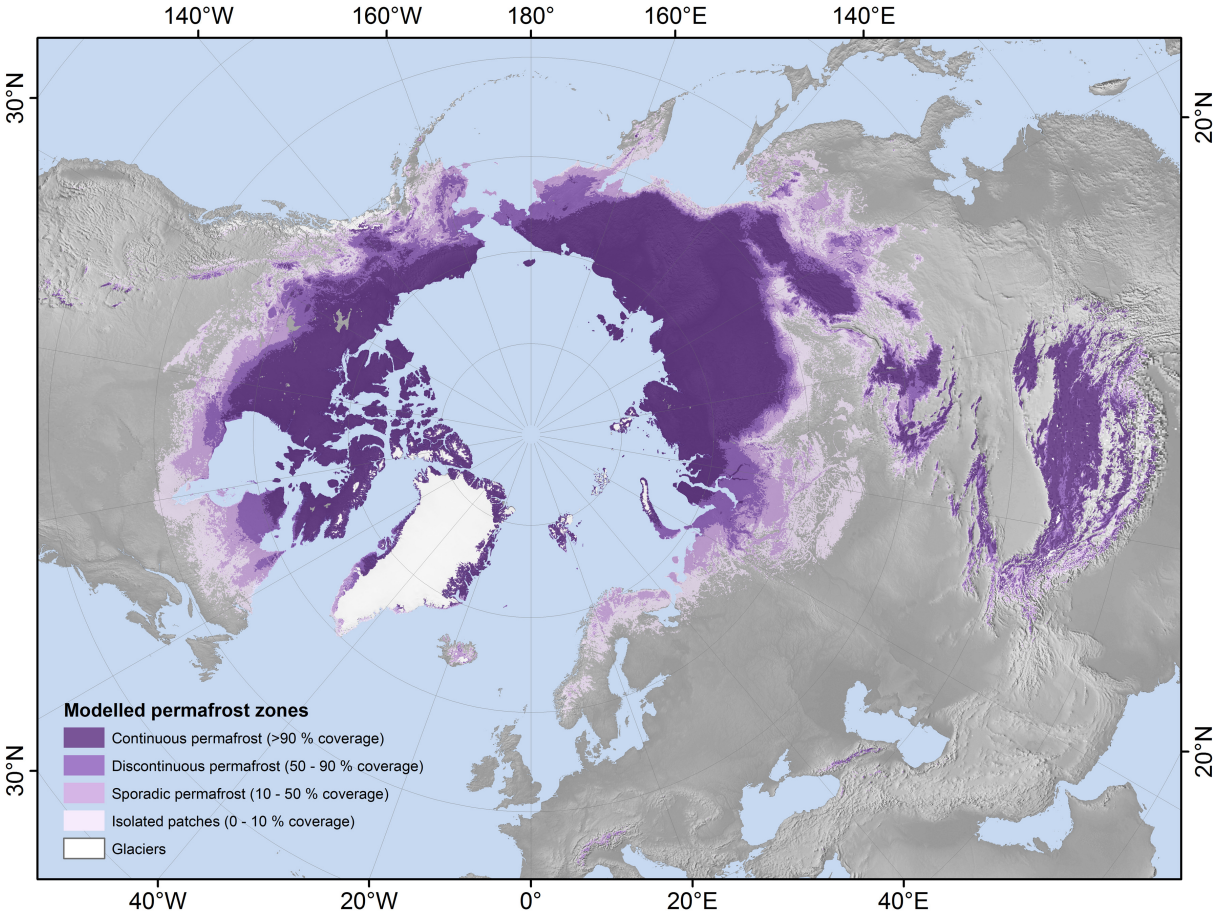

Figure 2.1: Spatial permafrost distribution in the Northern Hemisphere (Jaroslav et al., 2019).

some coastal areas, the ice-free land area is underlain by permafrost. The permafrost thickness ranges from 500 meters thickness in high mountain areas to less than 100 meters close to the sea, as water bodies are a large heat source (Humlum et al., 2003). The average thickness of the seasonally thawed top layer, or active layer, varies between 1.0 to 2.0 metres (Hanssen-Bauer et al., 2019). An unfrozen layer underlies the permafrost in sufficient depth caused by the heat generated in the earth's interior. The geothermal gradient varies between 0.3 and 1.1 °C per 30 meters for different locations on earth (Andersland and Ladanyi, 2004). Studies show that the average geothermal gradient lies at around 0.02 °C per meter (Instanes and Rongved, 2019) or the average geothermal heat flux at 70 mW/m² (Midttoemme et al., 2015).

Longyearbyen is situated on Spitsbergen, along the coast of Adventfjorden. It is located in a deeply eroded valley named Longyeardalen, constraint by mountain plateaus and glaciers and the Longyearelva river passing through, as shown in Figure 2.3. Due to the spatial constraint of the town, an extensive part of infrastructure and buildings in Longyearbyen are located in hazard prone areas subjected to avalanches, rock falls, mud or debris flow and

Figure 2.2: Map of permafrost distribution in Svalbard archipelago; shaded grey areas are underlain by permafrost (Humlum et al., 2003).

solifluction (Hanssen-Bauer et al., 2019). Additionally, all buildings and infrastructures are built on permafrost and the depth to bedrock is up to 100 metres in the middle of the valley (Instanes and Rongved, 2019). The permafrost is known to be ice-rich, with pore ice, segregated ice layers and buried glacial ice with an abundance of silt and clay dominated marine sediments (Hanssen-Bauer et al., 2019). Also, salt concentration in pore water is high at around 40 ppt (parts per thousand) in coastal area and decreases to 0 ppt at around 50 metres above sea level. To set this number in context, fresh water has a salinity of under 1 ppt (Swenson and Baldwin, 1965). These conditions of frost-susceptible sediments, warm permafrost and high salinity pose a challenge for construction and maintenance of infrastructure and buildings.

2.2 Permafrost Ground Thermal Regime

Permafrost dynamics are dependent on the surface energy balance, the geothermal gradient and the thermal properties of soil. The ground thermal regime of permafrost is commonly described by the mean annual ground temperature (MAGT), the maximum thickness of the seasonally thawed top layer or active layer (ALT) and by the depth of zero annual amplitude

Figure 2.3: The valley Longyeardalen in which Longyearbyen is located, confined by mountain plateaus and Larsbreen and Longyearbreen glacier (Hanssen-Bauer et al., 2019).

(DZAA). The DZAA is defined as the depth where maximum and minimum annual variations are less then 0.1 °C (Harris et al., 2017). A simplified representation of the ground regime after Burke et al. (2020) is shown in Figure 2.4a. The mean annual air temperature (MAAT) controls the existence of permafrost and for it to exist it must be below 0 °C. The surface offset is the temperature difference between air and surface temperature due to climatic variables, this will be explained in more detail in subsection 2.2.1. The thermal offset in the representation below is a commonly used variable in permafrost modelling, it is the difference between mean annual temperature at top of the permafrost (TTOP) and the mean annual ground surface temperature (MAGST). Burn and Smith (1988) found that permafrost exists and can also grow with MAGST above 0 °C. The thermal offset will not be discussed further in this study, but the existence of it is acknowledged here as it is an important feature in the thermal regime and temperature distribution. Further on, the geothermal heat flux controls the lower boundary of the permafrost, illustrated by a thawed soil layer in sufficient depth. It is important to note is that the representation is not to scale and permafrost can be several hundred meters thick.

As pointed out, air temperature influences the ground thermal regime in permafrost. Air temperature fluctuates over a given time scale, e.g. day, month or year. Its variation can be approximated with a sinusoidal fluctuation and this is reflected in the ground subsurface temperatures. Consequently the variation of temperature in the ground is also sinusoidal but its amplitude decreases over depth until the temperature becomes constant, or in other words until DZAA is reached. The maximum amplitude in the subsurface in relation to the ground surface is smaller and shifted to the right as illustrated in Figure 2.4b. The time difference for the ground to experience the same temperature as the ground surface at any given time t is defined as lag time. Hence, the ground thermal regime takes time to adapt to

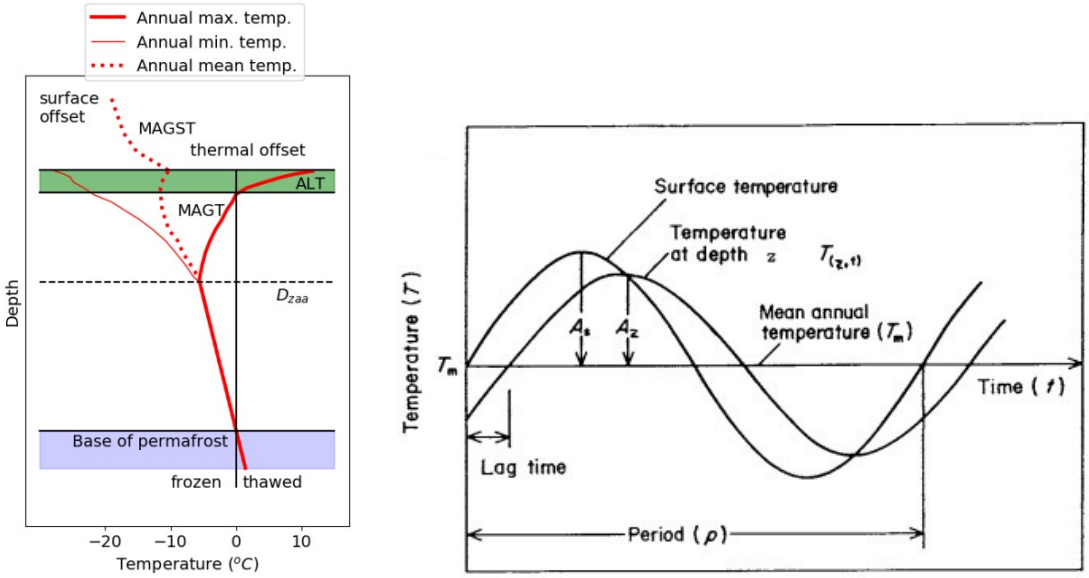

(a) (b)

Figure 2.4: (a) A schematic representation of the thermal regime in permafrost and its parameters (Burke et al., 2020); (b) Simplified representation of the seasonal sinusoidal trend of air temperature and the grounds response showing the delay of the ground response to the surface temperature (Andersland and Ladanyi, 2004).

climatic conditions.

2.2.1 Surface Energy Balance

The surface energy balance varies over respective time scales, e.g. yearly, daily. Climatic factors such as surface radiation, convective heat flow between air and ground, and heat flow due to evaporation or condensation alter the ground surface temperature. Its energy balance Q, at the ground surface, is composed of energy gains and losses (Hartmann, 2015):

$$\frac{\partial Q}{\partial t} = SW_{net} + LW_{net} - SH - LH - GH - G_{melt} \tag{2.1}$$

where SW_{net} and LW_{net} denote the net solar shortwave and longwave radiation fluxes, SH is sensible heat flux, LH is latent heat flux, GH stands for the exchange of energy between surface and the underlying ground and G_{melt} is energy flux due to phase change of water and ice in the surface layer.

The net solar radiation is the major source of incoming heat (Van Huissteden, 2020). Shortwave stands for direct radiation from the sun, longwave for diffuse radiation scattered by clouds and atmosphere. The net solar radiation is a balance of incoming absorbed and reflected shortwave and longwave radiation. The incoming shortwave radiation depends on topography, latitude and season. The radiation contributing to warming of the surface is governed by the surface albedo. The albedo differs for surface conditions, e.g. albedo of

fresh snow is 0.9 whereas albedo of water is 0.1 (Van Huissteden, 2020). Sensible and latent heat fluxes at the surface are a result of evaporation or condensation of water and convective heat transport by wind. Further on, heat conduction in or out of the ground and latent heat for freezing of water or thawing of ice in the surface layer contribute to the energy balance (Hartmann, 2015).

Often a detailed representation of the surface energy balance is not available. For modelling purposes an empirical based n-factor approach to simulate the complex relation of air temperature and climate is commonly used, when insufficient site-specific data is available (Riseborough et al., 2008; Instanes, 2016). This approach requires to define a transfer function to link air and ground surface temperature in thawing and freezing season respectively. For engineering studies n-factors have been used since the 1960s to parametrize the temperature at the ground surface (Klene et al., 2001).

The seasonal surface n-factor is the ratio between the air and surface freezing index (I_{af}, I_{sf}) or thawing index (I_{at}, I_{st}) respectively. The indices are defined for the respective season by degree-days [$°C \cdot days$]. Freezing degree-days are defined as days with a mean daily temperature below 0 °C, whereas thawing degree-days are days with a mean daily temperature above 0 °C. The freezing index, is the sum of degree-days between the maximum (autumn) and minimum (spring) point on a curve of time versus cumulative degree-days. The thawing index is the sum of degree-days from the minimum point to the next maximum point in the following autumn. Finally, the mathematical formulation of the surface n-factor can be written after Andersland and Ladanyi (2004):

$$n_f = \frac{I_{sf}}{I_{af}} \tag{2.2}$$

$$n_t = \frac{I_{st}}{I_{at}} \tag{2.3}$$

Surface n-factors rely on the surface condition in each location, which can change over time. However, Shur and Slavin-Borovskiy (1993) found that site-specific n-factors are stable for continental arctic areas with inter-annual changes of less than 10 %. A summary of n-factors from literature is shown in Table 2.1, where it is visible that the thawing n-factor is higher and increases for darker surfaces as more heat is absorbed.

Table 2.1: Values for n-factors measured in Arctic Alaska and Canada (Smith, 1996)

Surface [-]	nt [-]	nf [-]
Concrete	1.5 to 2.1	0.6 to 0.8
Gravel road	1.4 to 1.9	0.75 to 0.9
Dark gravel	1.3 to 1.7	-
Snow	-	0.8 to 1.0
Grass	0.8 to 1.0	0.5

2.2.2 Ground Heat Flux

In soil, heat transfer occurs due to three main physical processes as shown in Figure 2.6: conduction, convection and radiation. Heat conduction describes thermal conduction between solids, whereas heat convection describes thermal conduction with a mobile fluid. Radiation describes the phenomenon that every body above absolute zero omits energy from their surface. Convection is thus associated with mass transfer, conduction and radiation are not (Boeckh and Wetzel, 2018). Heat transfer can be quantified in heat flow Q or heat flux q. Heat flow describes how much heat is transferred per unit time, hence its unit is [J/sec] or commonly used [W]. Heat flux describes the heat flow per unit area and its unit is [(J/sec)/m^2] or [W/m^2] .

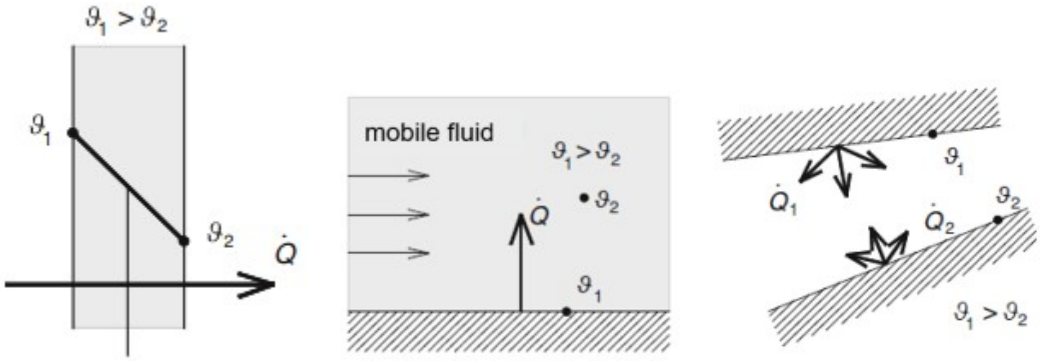

(a) Heat conduction process in a solid body or stationary fluid.

(b) Heat conduction between a solid surface and a mobile fluid (Convection).

(c) Heat exchange by radiation between two surfaces.

Figure 2.5: Three types of heat transfer; ϑ stands for temperature and $\dot{Q}$ for heat flow (Boeckh and Wetzel, 2018).

However, conduction is the dominant process in soils, although dependent on soil type and saturation, different processes become more important as illustrated in Figure 2.6. For engineering practice, subsurface temperatures are often found by solving the general heat conduction equation and including convective and radiative effects as boundary conditions (Esch, 2004), this dismisses the fact of groundwater occurrence especially present in discontinuous permafrost or areas of seasonal frozen ground. This study assumes no groundwater flow in the soil and solely focuses on heat conduction as the governing process for changes

in the ground thermal regime. For steady-state problems, the thermal conductivity of the soil is the governing parameter. For transient or time-dependent problems the thermal diffusivity, or in other words the ratio of thermal conductivity to volumetric heat capacity, and in situations of phase change, the latent heat of fusion are dominating parameters (Williams and Smith, 1989).

The presence of ice and water as volume fraction of pore water, influence the thermal properties of soil drastically. Large changes of thermal properties are thus observed for small temperature variations around the freezing point of the soil. When water changes phase, the thermal conductivity increases by factor 4, the mass heat capacity decreases by half and heat equivalent to raising the temperature of an equivalent volume of rock by 150 °C is released (Williams and Smith, 1989). This energy release is defined as latent heat of fusion.

Soil is a composite material, thus alongside the temperature dependency, thermal properties depend on its mineral composition, organic content, density, moisture content in form of water, vapour or ice (Farouki, 1981). Consequently a distinct value can not be specified for thermal properties of a specific soil, but only a function of effective thermal property dependent on temperature.

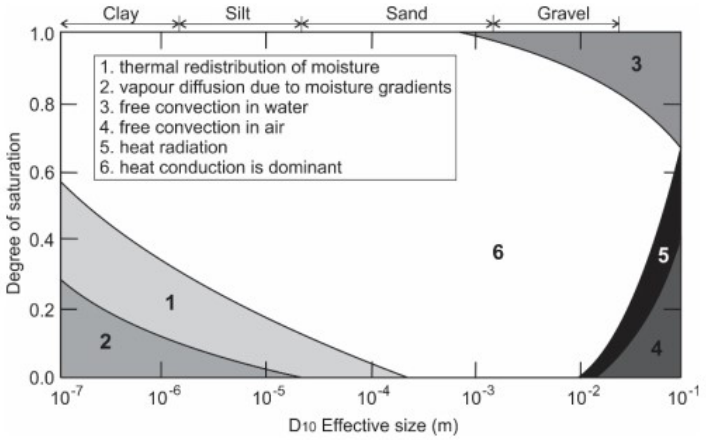

Figure 2.6: Heat transfer processes in soils dependent on the degree of saturation and soil type (Vieira et al., 2017).

For heat transfer problems the first law of thermodynamics applies, which defines the conservation of total internal energy. Applied on a layer of soil, it means the heat flow into a soil layer must be equal to the heat flow out of the layer plus the change in heat content (Boeckh and Wetzel, 2018). In frozen soils, the release and absorption of latent heat of fusion for soil undergoing freezing and thawing processes as well as the temperature dependency of thermal conductivity dominate the heat flow in the ground (Riseborough et al., 2008). Therefore for permafrost modelling the consideration of latent heat of fusion and temperature depen-

dency of thermal conductivity is crucial. Also, in vicinity to the ocean, a freezing point depression in the soil pore water is often observed and can influence the thermal properties, e.g. unfrozen water content.

Thermal Conductivity

Energy transfer between molecules caused by a temperature gradient is defined as heat conduction. The internal energy is transferred between particles of different temperature by vibrating and colliding molecules. The flux of energy in the direction of temperature decrease is proportional to the temperature gradient in flow direction and the material's thermal conductivity. For a homogenous body, this is described by Fourier's law:

$$q = \frac{Q}{A} = -k\nabla T \tag{2.4}$$

where q [W/m²] is the heat flux and Q [W] is the heat flow respectively, A [m²] is the area perpendicular to the flow direction, k [W/(m.°C)] is thermal conductivity and ∇T is the temperature gradient in flow direction [°C/m]. The negative sign indicates heat flow from warmer to colder temperature regimes. Also, Equation 2.4 shows that for a given temperature gradient, more heat flows through a material of higher conductivity.

The thermal conductivity of soil is dependent on its constituents including solid particles, air, and pore water and/or ice in frozen ground. Its effective thermal conductivity k can be computed as a weighted geometric mean using Johansen's thermal parametrization (Johansen, 1977):

$$k_{eff} = k_s^{1-n} \cdot k_i^{nS_w(1-\Phi)} \cdot k_w^{nS_w\Phi} \cdot k_a^{n(1-S_w)} \tag{2.5}$$

where the subscripts s stands for soil, i for ice, w for water and a for air respectively, S_w [-] is the degree of water saturation, n is porosity and Φ [-] the volumetric fraction of unfrozen water content. There are different formulations for the particle conductivity available, here a formulation to determine a geometric mean of conductivities is used (Johansen, 1977):

$$k_s = k_q^q k_0^{1-q} \tag{2.6}$$

where q stands for the fraction of quartz and o for other minerals and k_q is 7.7 W/(m.°C) and k_0 is 2.0 W/(m.°C).

Heat Capacity

The heat content of a soil can be described by knowing its heat capacity. Specific heat capacity c_p [kJ/(kg ·°C)] describes the amount of energy needed to raise the temperature of 1 kg of soil by 1 °C. The changes in temperature are greater for a material with low heat capacity for the same amount of supplied energy. The specific heat capacity of a material increases with increasing temperature (Kersten, 1949). Also, with increasing density the heat capacity of a given soil increases. Furthermore, the heat capacity increases as the moisture content increases. This can be explained by comparing the specific heat capacity of water which is 4.2 [MJ/(m³·°C)] to most dry soils which have a heat capacity between 1 and 1.5 [MJ/(m³·°C)] around 0 °C (Abu-Hamdeh, 2003).

Commonly used in engineering practice, is the volumetric heat capacity C [MJ/(m³·°C)] which is obtained by multiplying the specific heat capacity with the material's bulk density. This removes the parameters dependency on porosity and values for different materials can be compared more effectively. The volumetric heat capacity of unfrozen and frozen mineral soils can be estimated after Andersland and Ladanyi (2004) stated in Equation 2.7 and 2.8.

$$C_{vu} = \frac{\rho_d}{\rho_w}\left(0.17 + 1.0\frac{w}{100}\right) \cdot C_{vw} \tag{2.7}$$

$$C_{vf} = \frac{\rho_d}{\rho_w}\left(0.17 + 1.0\frac{w_u}{100} + 0.5\frac{w - w_u}{100}\right) \cdot C_{vw} \tag{2.8}$$

where ρ_d [g/cm³] is dry density of the material, ρ_w [g/cm³] is density of water, C_{vw} is the volumetric heat capacity of water at 0 °C and 0.17, 1.0 and 0.5 correspond to specific heats of soil, water and ice. w and w_u respectively stand for water content and unfrozen water content for temperatures below the soil's freezing point. The effective heat capacity C_e can be estimated as an arithmetic mean of frozen and unfrozen heat capacities weighted by the fraction of unfrozen water Φ in the soil:

$$C_{eff} = C_{vf}(1 - \Phi) + C_{vu}\Phi \tag{2.9}$$

Latent Heat of Fusion

The effects of latent heat of fusion are often included in an apparent heat capacity. This includes the heat capacity and the latent heat of fusion of the soil and represent the heat storage term of the energy balance equation. This results from the fact that when water

changes to ice, latent heat is released corresponding to the volume of pore water that freezes. This added heat warms the soil and thus must be removed in order to cool the soil again. This mirrors the effects of heat capacity of soil which in the case of cooling describes the amount of heat that needs to be removed to cool the ground by 1 °C. The latent heat of fusion L [kJ/m³] for a given soil can be estimated by (Andersland and Ladanyi, 2004):

$$L = \rho_d L' \frac{w - w_u}{100} \tag{2.10}$$

where L' is the latent heat of fusion for water [kJ/kg], ρ_d dry density [kg/m³], w [%] the total water content and w_u [%] the unfrozen water content.

Unfrozen Water in Frozen Soil

The presence of water in sub zero temperature majorly impacts the soil thermal behaviour. Numerous factors are connected to the unfrozen water content such as water migration to the freezing front, hysteresis effects in freeze-thaw cycles and dependency of thermal properties on the proportion of water and ice (Esch, 2004). Here, the focus lies on the latter mentioned impact, the dependence of thermal properties on the amount of unfrozen water in frozen soil. Pore water freezes at its specific freezing point. This freezing point is ultimately dependent on the salinity of the respective soil. Saline soils have a lower freezing point than non-saline soils. Proximity to the sea results in a large variation of the salinity profile and concentration of salinity increases with depth due to a change of pore fluids from fresh water to seawater.

The unfrozen water content is a soil specific parameter varying for a temperature range below the respective freezing point. Particles in fine-grained soils adsorb more water to a higher specific surface. Thus the unfrozen water content increases with increasing specific surface of soil particles. The unfrozen water is found as a thin film on the grain's particles.

The gravimetric fraction of unfrozen water w_u [%] content in soils can be approximated by an empirical method (Andersland and Ladanyi, 2004):

$$w_u = \alpha \Theta^{\beta} \tag{2.11}$$

where Θ [°C] stands for temperature in positive values below the freezing point of the soil and α and β are empirical soil specific parameters (Andersland and Ladanyi, 2004). Adopting α and β from other soils can lead to a wrong estimation of unfrozen water content since these parameters are soil specific. Tice et al. (1976) describe a method to estimate soil specific α

and β values by its water content values for 25 and 100 blows respectively in liquid limit tests.

In engineering practice, the normalized volumetric unfrozen water content (or fraction of unfrozen water) Φ [-] of soil is often used. It ranges from 0.0 to 1.0 and can be estimated by solving for the gravimetric fraction of unfrozen water as proposed in Equation 2.11, and then obtaining the normalized volumetric unfrozen water content by solving Equation 2.12 to 2.14 as following:

$$w_u = \frac{m_{uw}}{m_s} = \frac{V_{uw}\rho_w}{V_{tot}\rho_d} = \frac{\frac{m_{uw}\rho_w}{\rho_w}}{\frac{m_s\rho_d}{\rho_d}} = \Theta_u\frac{\rho_w}{\rho_d} \tag{2.12}$$

$$\Theta_u = \frac{w_u}{100}\cdot\frac{\rho_d}{\rho_w} \tag{2.13}$$

$$\Phi = \frac{\Theta_u}{n\cdot S_w} \tag{2.14}$$

where ρ_d [m³/kg] is dry density of soil, ρ_w [m³/kg] is density of water, Θ_u [m^3_{water}/m^3_{soil}] is volumetric unfrozen water content, n is porosity [-] and S_w is the degree of water saturation of the soil.

2.3 Permafrost Warming and its Effects

Sustainable development of Arctic communities is challenged by perennial frozen ground (Ramage et al., 2021; Hjort et al., 2018). Climate change, human-induced changes as well as the industrial development of the Arctic coast can evoke changes in the thermal regime of permanently frozen soils leading to thaw subsidence, coastal erosion, increased creep rates and loss of strength in the soil (Instanes and Rongved, 2019; Instanes, 2016). Shur and Goering (2009) found that extensive thaw of permafrost is often caused by inappropriate design or maintenance of structures and infrastructure with climatic conditions unchanged.

2.3.1 Climate Change

A recent study by AMAP (2021) found that the mean annual surface temperature in the Arctic between 1971 and 2019 increased three times as much as the global mean during the same period. The average global surface temperature is projected to rise to 3.3-10 °C by 2100 under different emission scenarios. Also, extreme cold events are decreasing and an increase in extreme high temperatures is observed. Arctic communities, their safety, well-being, socio-

economic development, infrastructure and livelihood is affected by climate. The cryosphere is experiencing extreme changes including changes in extent and seasonality of sea ice and snow cover and substantial loss of permafrost and Greenland ice sheet which also affects the cycling of carbon and greenhouse gas and potentially affects the global atmospheric greenhouse gas concentration (AMAP, 2021). Permafrost melt can turn the Arctic into a carbon source rather than a carbon sink for the atmosphere, which means that the Arctic would feed into the warming of the atmosphere and an unstoppable cycle is entered. This is caused by the release of greenhouse gas (GHG) from permafrost upon thawing. These GHGs, namely methane and carbon dioxide, absorb solar heat rather than reflect it and therefore amplify the warming of the globe (Schaefer, 2021).

Increase of ground surface temperature consequently leads to a rise of deeper ground temperature and thawing of ground ice, overall it leads to a reduction of the global permafrost extent (Smith et al., 2005). Since 2000, record-high mean annual ground temperatures have been measured in permafrost regions of Alaska, Canada and Svalbard (Romanovsky et al., 2010). Recent studies for Svalbard found that air temperature is increasing, surface and ground temperature are climbing and winters are warming faster than summers. The active layer thickness is consequently deepening as permafrost is thawing (Gjermundsen et al., 2021; Hanssen-Bauer et al., 2019; Christiansen et al., 2019; Foerland et al., 2011). Hanssen-Bauer et al. (2019) state that *near-surface permafrost is projected to thaw in coastal and low altitude areas for the high emission scenario [until 2100].* Also, frequency and intensity of rainfall is increasing, with projected heavy rainfall events even during winter. The total days of snow cover on Svalbard is projected to decrease (Hanssen-Bauer et al., 2019). The mean annual air temperature between 1971 and 2017 warmed by 3 to 5 °C, varying for different locations on Svalbard (see Figure 2.7). In winter, the air temperature has warmed by 5 to 8 °C (Hanssen-Bauer et al., 2019). Figure 2.8 shows the steady increase of subsurface temperature in the upper 20 meters of the ground in the past 20 years on Svalbard.

2.3.2 Engineered Warming

The thermal equilibrium of the ground can be disrupted by human activities, which can consequently lead to thawing of permafrost (Brown et al., 1997; Instanes, 2006; Shur and Goering, 2009; Burke et al., 2020). Construction of buildings and infrastructure, removal or change of surface conditions, snow ploughing, asphalting and numerous other activities alter the energy balance at the ground surface. An experimental study over a period of 26 years,

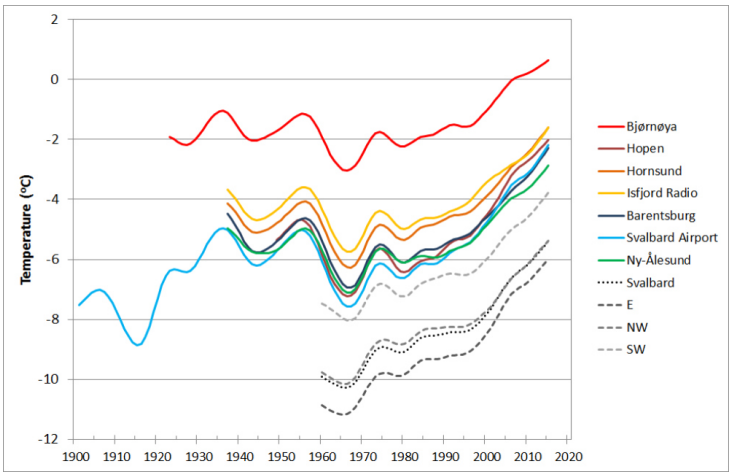

Figure 2.7: Long-term time series of mean annual air temperature from numerous weather stations around Svalbard showing a consistent warming trend (Hanssen-Bauer et al., 2019).

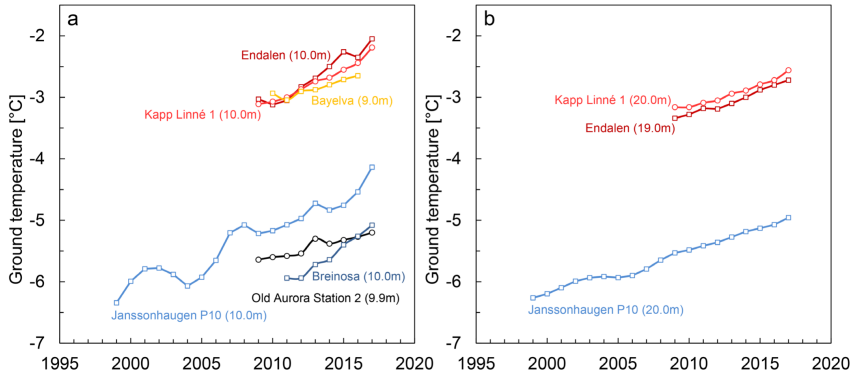

Figure 2.8: Mean annual ground temperatures for various permafrost monitoring locations on Svalbard showing a warming trend (Hanssen-Bauer et al., 2019).

demonstrates the difference in permafrost extent due to removal of vegetation (Linell, 1973). The result of the study is illustrated in Figure 2.9 and visualizes the induced changes in temperatures below the ground surface. Additionally, structures placed on permafrost can lead to deeper freezing of the ground in winter and thawing in summer (Smith et al., 2005), which can lead to significant deformation of the ground (Brown, 1970).

A major factor leading to warming of permafrost is the conductive heat transfer through the floor of a building to the adjacent ground. In permafrost regions, this heat transfer can lead to a significant change in the ground thermal regime. For rough estimates a steady-state heat flow can be assumed through the building floor to the ground (Goodrich and Plunkett, 1990; Andersland and Ladanyi, 2004). A foundation system is often made up of different layers and the heat flow through different layers can be computed by estimating the thermal

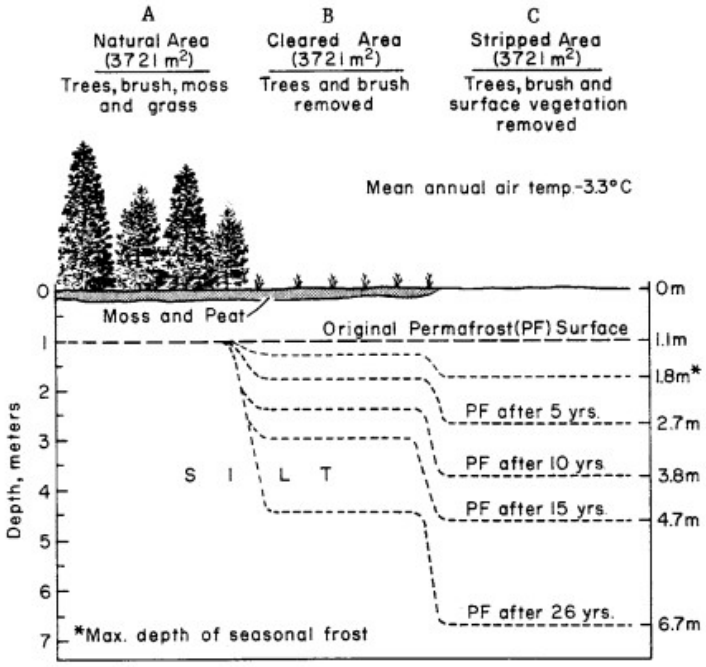

Figure 2.9: Results from an experimental investigation showing the differences in permafrost distribution in the ground over a period of 26 years (Linell, 1973).

resistance R. A steady heat flow Q [W] through a building floor can be written as following:

$$Q = \frac{\Delta T}{R} = \frac{T_2 - T_1}{\left(\frac{x}{k \cdot A}\right)} \tag{2.15}$$

where ΔT is the temperature gradient in the direction of the heat flow, T_2 [°C] is the inside temperature of the floor and T_1 [°C] is the ground temperature at the base of the foundation. The thermal resistance R [W/K] depends on the thickness and thermal conductivity of the layer. Therefore heat flow decreases with an increasing thermal resistance. If a system is composed of multiple layers the total thermal resistance can be estimated as:

$$R = \sum_{i}^{n} \frac{x_i}{k_i} \tag{2.16}$$

2.3.3 Coastal Warming

Humlum et al. (2003) points out that water bodies such as oceans, lakes or rivers are major heat sources. Permafrost closer than 100 metres to a water body is likely to be affected by it. This can also be observed in Svalbard, where coastal permafrost is starting to show discontinuities compared to continuous permafrost situated inland (Hanssen-Bauer et al., 2019). Already Lachenbruch (1970) found that mean surface temperature at the Arctic coast was increasing significantly compared to the past 100 years. The energy balance for water bod-

ies differs greatly from land surface due to numerous reasons which will not be explained here in great detail but are discussed in Van Huissteden (2020). Also, freezing point depression in saline soils found close to the ocean, can leave the ground unfrozen even at ground temperatures below 0 °C.

2.3.4 Implications for Permafrost Engineering

As discussed, permafrost is very sensible to changes of ground surface condition and air temperature. Hence warming can be amplified if the ground surface is disturbed or the air temperature warms.

The strength of frozen soil and the bearing capacity is dependent on the ice content in the soil which decreases with increasing ground temperatures. Soil which pose the largest risk are thaw-unstable or frost-susceptible soils which are characterized by volume change and development of excess pore pressure and decrease of shear strength upon thawing (French, 2007). Frost susceptible soils are characterized by permeability and capillary rise. A problem in regards to construction is ice segregation in the ground which occurs under high permeability and low capillary rise in the ground. Gravel is coarse-grained, has a high permeability but low capillary rise which allows water to flow through the soil, but the surface tension of the grains is too low to keep excess water. Therefore no excess ice will form and frost heave is usually not critical. Clay has a low permeability but high capillary rise which means in clean clay layers water will not accumulate. Silt has a high permeability and a high capillary rise making it a very frost-susceptible type of soil. Water can flow through the soil and surface tension of grains is high and draws water in and allows excess ice to form at freezing temperatures.

When temperature in the ground increases and ice starts to thaw, differential settlements can introduce stability issues and cracks in the footing and structure. The bearing capacity of the soil is lowered upon thawing as water has no shear strength. Thaw unstable soils are characterized by a significant loss of strength upon thawing below normal values of thawed soils. Thaw unstable soils, in presence of large ice lenses, present a risk of sudden surface subsidence and water ponding on the ground surface upon thawing. Water ponding changes the heat balance, as water allows more heat to flow into the ground.

For engineering structures not only thawing by itself but also the interplay between thawing and freezing of the soil is problematic. Deeper freezing in winter and amplified warming in summer can lead to greater frost action, defined as “the process of alternate freezing and

thawing of moisture in soil, rock and other materials, and the resulting effects on materials and on structures placed on, or in, the ground“ (NSIDC, 2020). A volume increase of about 9% (Harris et al., 2017) can result in a significant lift, or frost heave, of the ground upon freezing.

Special foundation techniques are required for ice-rich permafrost to ensure thermal stability during the service lifetime of the building. Most structures are designed for a service lifetime of 30 to 50 years in the Arctic (Instanes, 2016, 2010). Instanes (2006) states that it is inevitable for permafrost engineers to adopt innovative solutions to preserve infrastructure foundations under projected climate conditions. As pointed out before, ground in its frozen state develops favourable properties for construction such as high strength and low permeability. Hence, modern solutions for permafrost engineering aim to maintain the thermal equilibrium of the ground and preserve the ground's temperature dependent properties (French, 2007).

Several foundation methods, ranging from passive to active cooling systems, pile foundations and elevation of buildings are used to prevent or minimize the change of the thermal regime. In ice-rich, saline permafrost in light of climate change a suitable solution is the artificial cooling of the ground to maintain the mechanical and thermal stability of foundations (Instanes, 2010). A heat pump cooling system is a cost-effective cooling solution as heat is extracted from the ground and can be reused to heat the building above. Some cases of heat pump cooled foundations are found in Canada (Stenbeak-Nielson and Sweet, 1975; Goodrich and Plunkett, 1990; Zhang and Horne, 2012) and Svalbard as described in the following section.

2.4 Heat Pump Cooled Foundations

The concept of heat pump cooling systems for foundations is adjusted from ground source heat pump application for milder climates. In milder climates ground source heat pump technology has been successfully implemented in a variety of underground structures as a renewable and sustainable heat source (Brandl, 2013; Singh et al., 2019). A ground source heat pump system is commonly composed of a ground loop, a heat pump and a heat distribution system. The ground loop is composed of pipes in the ground transferring energy to a so called heat carrier fluid (HCF) which constantly circulates. The heat pump unit is a mechanical system that extracts the energy from the HCF and is run on electricity to raise the temperature of the HCF to a higher temperature. The heat distribution system distributes

the heat to a building space.

A heat pump is typically composed of an evaporator, compressor, condenser and expansion valve. The working fluid or heat carrier fluid (HCF) is pumped through the ground loops by a circulating pump at a temperature colder than the adjacent ground. That results in heat flowing to the colder regime, so towards the working fluid in the ground loops. The HCF warms up in the process and is pumped back to the heat pump by a circulating pump. The heat exchange in the heat pump takes place in the evaporator. The heat is passed from the working fluid to a liquid refrigerant in the heat pump loop which consequently evaporates into gas (evaporator). The compressor draws the evaporated refrigerant in and compresses it, raising the pressure and consequently the temperature. In the condenser heat is extracted from the refrigerant causing the gas to condense back into liquid. The expansion valve reduces the pressure and lowers the temperature of the refrigerant fluid to its original state and the cycle starts from the beginning.

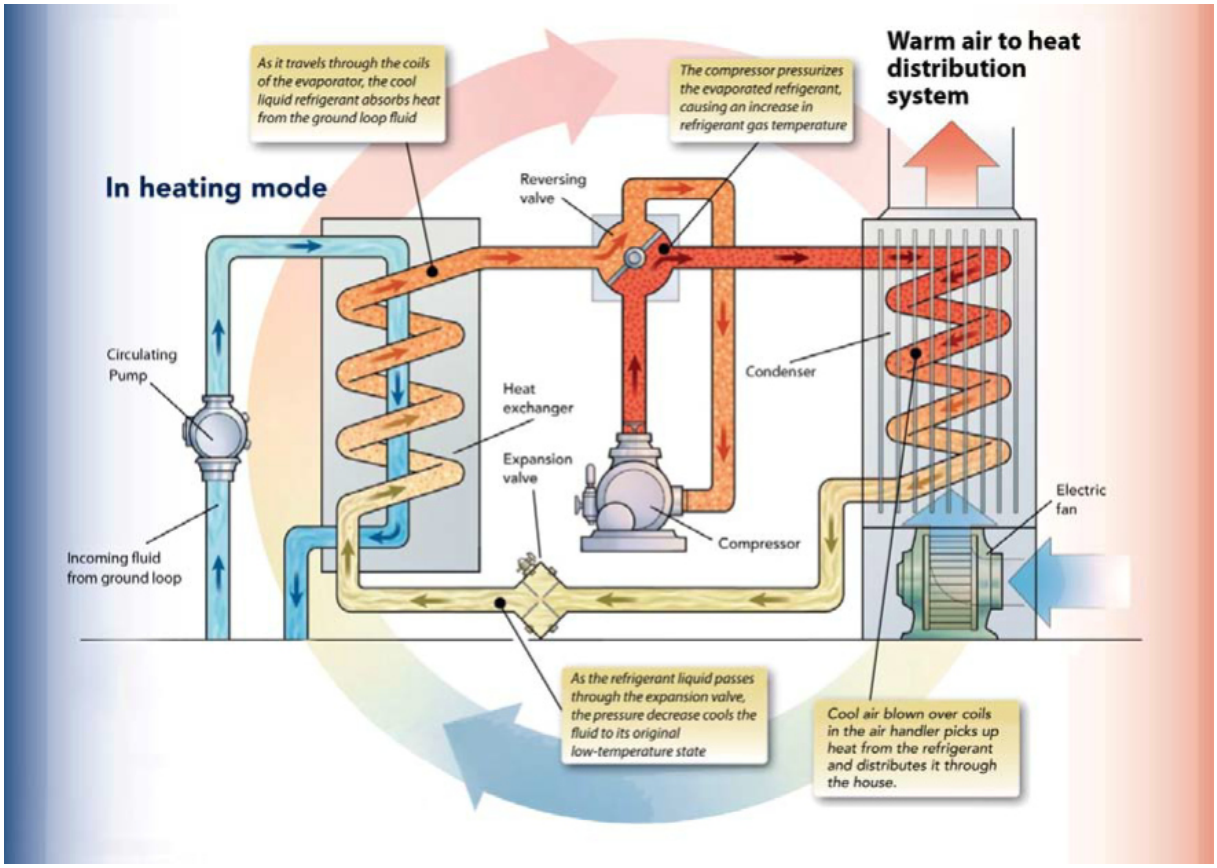

Figure 2.10: Illustration of a heat-pump system in heating mode coupled with a heat distribution system showing the integral parts of the system and the ongoing cycle to extract the heat from the HCF (QWare, nd).

For heating purposes, the efficiency of a heat pump system can be described by Equation 2.17. The coefficient of performance (COP) is the ratio of the amount of usable energy extracted

from the ground E_{out} [kW] to the amount of electrical energy needed E_{in} [kW] to run the system. Heat pumps for heating have a COP greater than 1.0 since the energy delivered from the system is greater than the energy required to run the system. In heating operations a COP of 4.0 is desirable (Singh et al., 2019).

$$COP = \frac{E_{out}}{E_{in}} = \frac{G+E}{E} \tag{2.17}$$

where G [W] is the rate of ground heat extraction and E [W] the electrical power consumed (Goodrich and Plunkett, 1990). Goodrich and Plunkett (1990) state that a COP of 2.3 to 2.5 at entering fluid temperature from -10 to -5 °C is typical for ground source heat pumps and the Meyer et al. (2011) found that a COP between 2 and 3 is reasonable for cold climates. The efficiency of the heat pump is highly dependent on the temperature of the heat source, i.e. the ground, and the heat sink, i.e. the air or heat distribution system. A low temperature gradient between the source and sink leads to a higher efficiency. Thus, if the inlet temperature is low and the desired outlet temperature is low, the efficiency is higher.

The application of ground source heat pumps in colder climate was developed with the intention to maintain the permafrost thermal regime after construction, rather than creating a renewable energy source for heating. Therefore, it is designed to artificially keep the ground frozen. The principle for permafrost application is simple, the excess heat, which is transferred through the floor of a building to the underlying ground, can be extracted from the ground and thaw beneath the building can be limited. The system can also be designed to heat the building above but most cases in permafrost regions show no such design. The reasons are not stated and very little literature and studies are available on ground source heat pump applications for maintaining the permafrost and heating the building above.

Ground source systems can be designed with open or closed-loop heat exchangers and horizontal or vertical layouts. For permafrost application the horizontal closed loop system is relevant. Closed-loop systems circulate a heat carrier fluid (HCF) through a network of pipes installed in the foundation plate through a circulating pump. The heat in the ground flows in direction of the ground loops as the HCF is colder than the adjacent ground temperature. Commonly, several loops are fitted in the concrete slab so each loop can be individually checked and adjusted and offers more safety in view of malfunction as loops can then be individually disconnected in case of defects (Singh et al., 2019).

2.4.1 Existing Heat-Pump Cooling Foundations in Longyearbyen

In Longyearbyen, a large case history of damages to infrastructure and buildings caused by permafrost degradation is present. Cases range from deformation of the Svalbard Airport runway (Instanes and Mjureke, 2005), flooding of the Global Seed Vault in 2017 (Statsbyg, nd), deformation of roads in town, evacuation of residential buildings (Dickie, 2021) and several foundation reconstruction for buildings, including Sysselmannsgården (the houses of the Governor of Svalbard), the Telegraph building and Sysselmannsgården (Rongved and Instanes, 2012). The importance of special foundation techniques is obvious, as older buildings in Longyearbyen placed directly on permafrost either do not exist any more or had to be reconstructed. Exemplary, the thaw depth under Sysselmannsgarden reached 7 metres compared to a natural active layer thickness of 1 metre in this area (Rongved and Instanes, 2012).

Especially in regards to climate change, buildings founded on piles are subjected to increasing settlement damage and frost jacking. A study by Instanes and Anisimov (2008) found that pile capacity has been reduced by 12.5 % from 1977 to 2007. Wooden pile foundation have shown numerous cases of settlement due to severe rot in warm and thawing permafrost and should be avoided in the future due to ongoing warming climate (Rongved and Instanes, 2012; Instanes and Rongved, 2019). Nowadays, foundation solutions in Longyearbyen include elevated buildings on steel or concrete piles founded in the permafrost, elevated buildings on end bearing steel piles founded on the bedrock, soil replacement in areas of shallow depths to bed rock and artificial heat pump cooling systems (Instanes, 2010).

The heat pump cooling technique is primarily applied for buildings with heavy loads on ice-rich permafrost, for industrial buildings where access for vehicles must be ensured, for buildings with low tolerance of differential settlements or for reconstruction of failed foundations (Instanes, 1988; Rongved and Instanes, 2012). A list of previous projects on Svalbard is taken from Instanes and Rongved (2009) and presented in Table 2.2. Pictures of the existing buildings are shown in Figure 2.12. Exemplary previous designs from Svalbard are shown in Figure 2.11.

Table 2.2: Heat pump cooling foundations in Svalbard with respective permafrost temperature extracted from Instanes and Rongved (2009).

Building [-]	Year [-]	Area [m²]	Permafrost temperature [°C]
Lagerbygg (Svea)	1986	900	-6.0
Næringsbygget	1989-92	1200	-5.5
Svalbardbutikken	1990	1200	-5.5
Sysselmannsgården	1991	100	-5.0
ISS-bygget	2006	600	-3.5
Kulturhuset	2010	800	-4.0

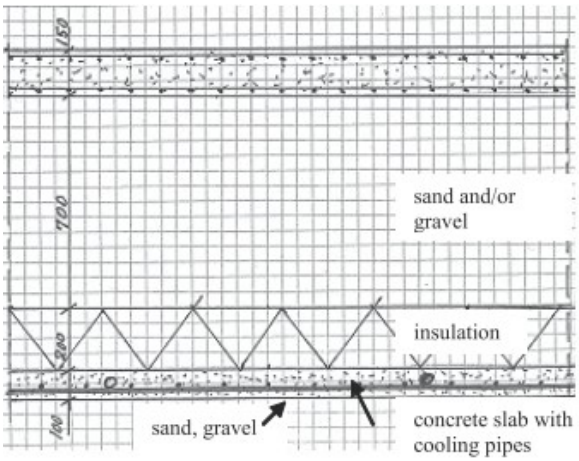

(a) Foundation design of storage building in Sveagruva (Instanes and Instanes, 2008).

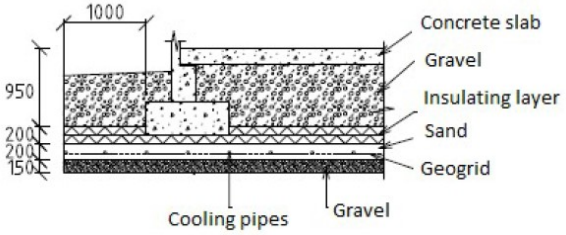

(b) Foundation design of Kulturhuset in Longyearbyen (Rongved and Instanes, 2012).

Figure 2.11: Exemplary foundation designs in previous projects on Svalbard.

Sysselmannsgården was reconstructed successfully, implementing heat pump cooled foundation. However power failure a few years after resulted in additional settlements as the system was not automatically restarted after the power failure. A residential building shown in Figure 2.12a and 2.12c, placed on a cooling plate, had to be evacuated, when the cooling system of the plate malfunctioned, and is now abandoned (Dickie, 2021). In order to minimize human error, it is recommended to have temperature sensors installed to automatically adjust the cooling temperature for the ground alongside proper maintenance of the system. Disadvantage for the system is the constant electrical power supply, the high initial cost and the maintenance to ensure the system is working correctly (Rongved and Instanes, 2012).

The Longyearbyen Kulturhuset (cultural house) was constructed in 2010 and placed on a heat pump cooling foundation. The building is an extension to an existing building which is also placed on a cooling slab. The existing building was finished in 1992. No clear records about the installation or specifications of the temperature sensors under the plate is available. The readings are given in resistivity but since no specification or calibration for the

thermistors is available, it is unclear how to interpret the readings (Shestov, A., personal communication, 26 February 2021). According to Dag Arne Husdal, Driftsingeniør Eiendom (Real Estate Operations Engineer) in Longyearbyen Lokalstyre, the aim is to optimize energy consumption in town and put the focus on renewable energy. Proper maintenance and measurements of energy consumption forms the bottom line for development. The cooling system for Næringsbygget was designed to be sufficient, in other words it is running continuously, cooling the ground but there is no information on how much the ground is cooled or possibly overcooled. As Dag Arne Husdal says, *The plant is producing cold for an imaginary need* (Mathisen, 2020). Excess heat is pushed out through cooling fans in the roof. This excess heat could be stored in batteries or used to heat the building. Furthermore, since the system needs most energy when energy from the sun is available, Longyearbyen Lokalstyre wants to develop a system where the cooling system is coupled with solar panels to harvest solar energy to run the heat pump system (Husdal, D. A., personal communication, 26 February 2021). This innovative technology is interesting for all permafrost areas, since it only relies on natural resources to maintain the energy supply for the system. The project is funded by the EU and Enova (Mathisen, 2020). Today, no system in Longyearbyen re-uses the extracted heat to heat the buildings above (Husdal, D. A., personal communication, 26 February 2021).

The latest project, with construction start in August 2020, for the application of a heat pump cooled foundation in Longyearbyen is the construction of a new environmental station (miljøstasjon). However, no thermal design has been conducted for the project and thus no thermal model of the ground exists. A more thorough analysis can provide detailed information of the ground's behaviour for future development of the system, to optimize the energy usage and to ensure stability for the service lifetime of the building. A detailed introduction to the project is given in chapter 4.

(a) Abandoned building in Longyearbyen, which had to be evacuated after a power failure in the cooling system. Cracks in the walls of the house are visible (Photo taken by the author).

(b) Reconstruction of the Sysselmannsgården foundation (Rongved and Instanes, 2012).

(c) Longyearbyen Kulturhuset (Photo taken by the author).

(d) Næringsbygget (Photo taken by the author).

(e) Svalbardbutikken (Photo taken by the author).

(f) Former ISS building (Photo taken by the author).

Figure 2.12: Photos of existing heat-pump cooling projects in Longyearbyen. They are all in operation except the house shown in (a) which is abandoned.

2.4.2 Advantages, Disadvantages and Possibilities

Studies state both advantages and disadvantages of the heat pump cooling system for permafrost engineering (Goodrich and Plunkett, 1990; Instanes and Instanes, 2008; Zarling and Yarmak, 2007; Instanes and Rongved, 2009; Instanes, 2010; Rongved and Instanes, 2012; Zhang and Horne, 2012; Instanes and Rongved, 2019). The advantages include that buildings can be placed directly on the permafrost, enabling vehicular access especially important for industrial facilities with heavy machinery. Also, pile foundation become very costly for large footing areas where the floor needs to be structural to transfer loads. Here, the load can be transferred via an embankment into the ground. Further on, for buildings with a long service lifetime, it is advantageous that permafrost temperatures can be maintained and cooling temperature can be adjusted for future climate warming, heat loss from the building can be regained and excess heat can be used to heat the building. Perlshtein et al. (2001) point out that *the expenses of installing a heat pump can be compensated for by using the produced heat for the building itself.* The disadvantages are connected to human-induced errors during the operation of the system or undetected power failure of the cooling system. Zarling and Yarmak (2007) suggest that an operational manual in which all relevant information to keep the system running at its highest efficiency should be available and one maintenance contractor should be selected.

The sole application of a heat pump to cool the permafrost is not a climate friendly technology. The heat pump runs on electricity which is mostly generated from fossil fuels. There are however options to turn the technology into a climate-friendly, zero emission solution. Firstly, the excess heat can be used to e.g. heat the building above or heat domestic water. This is one of the major reasons for ground source heat pumps in milder climates and the technology is therefore already available and can be easily implemented. Secondly, heat pumps can be powered by solar power. A recent study about solar assisted refrigeration systems for permafrost embankments in China concludes that *solar refrigeration has been demonstrated as an efficient method for protecting permafrost (Tian-fei and Zu-run, 2021).* Solar refrigeration in the study includes systems run with photovoltaic technology (PV) and solar thermal technology. PV directly produces electricity from solar radiation and solar thermal technology harnesses solar heat and stores it. The advantages listed include a good seasonal correlation of the application, the sunlight in summer warms the permafrost, the heat can be extracted and be used again to cool the ground. Also, it provides a decentralized power supply for maintaining permafrost which can especially be of interest in off-grid

locations (Tian-fei and Zu-run, 2021).

Heat pump cooled foundation systems in permafrost regions can be differently designed, giving room for various different optimization possibilities. A foundation design in Yukon, Canada accounts for seasonal operation of the heat pump. In summer, when the building is not heated, the heat pump cooling system is turned off to save energy for operation. The design takes into account that thaw in the elevated embankment below the foundation is unproblematic as the fill material is not frost-susceptible and no volume change takes place (Zhang and Horne, 2012).

In cases where the heat is dissipated into the ambient air and not used for further heating, an option can be to turn the cooling system off in winter months when the ambient temperature is cold and the adjacent ground is fully frozen. This needs to take into account that the heat will always flow from warmer to colder regions, therefore the temperature gradient in the ground of the area under the plate and the adjacent ground can greatly influence the heat flow towards the plate.

2.5 Summary and Research Gaps

Permafrost is very sensitive to alteration of climatic and ground surface conditions. Especially warm, saline and ice-rich permafrost as commonly found on Svalbard, is very sensitive to changes. The thermal and mechanical properties of the soil are highly temperature dependent. Engineering designs must account for the variability of thermal properties and also consider the change during the service lifetime of a building, especially in light of amplified climate change in the Arctic. In engineering design, empirical relationships aid to estimate site specific conditions, such as seasonal n-factors to link air temperature to ground surface temperature.

Heat pump cooled foundations have been successfully implemented in Svalbard since 1986 to found new buildings or reconstruct foundations of old buildings. The heat pump system shows many innovative opportunities to develop this technology further, make it more sustainable and climate-friendly and allow it to become a go-to solution also for remote permafrost areas, as it opens up the possibility to build directly on permafrost and maintain the permafrost beneath it. The development of the system by connecting it with renewable energy sources to create electricity for the heat pump can open up an off-grid solution to artificially freeze the ground.

However, little research is conducted on the thermal behaviour of the ground for the heat

pump cooled foundation, under different design scenarios such as seasonal cooling and its application in view of climate change. In Longyearbyen, extracted excess heat is pushed out into the air and systems are not designed for energy efficiency. However, in order to develop this technology, more knowledge, project specific temperature measurements and maintenance protocols need to be established. The most recent project in Longyearbyen lacks a detailed thermal design and thus an insight into the ground's thermal regime which is valuable information for this project itself and for the town's plans to develop heat pump technology further.

Chapter 3

Methodology

A new project in Longyearbyen, building a new environmental station (ny miljøstasjon) on the largest heat pump cooled foundation to date on Svalbard, is under construction. The foundation area spans over 3400 m² with about 30 000 metres length of cooling pipes. It is of utter interest for the project itself and for future projects, to model the ground's behaviour beneath the cooling.

This chapter presents the methodology to study the thermal regime of the ground. Firstly, the finite element method, which underlies the numerical simulation in this study, is introduced and further, the validation and verification of numerical models is presented. Subsequently the mathematical formulation underlying the chosen numerical software GeoStudio TEMP/W is shortly introduced, followed by a short outline of the modelling approach for this study to give a comprehensive overview of the necessary steps to build the verified project-specific 3D model.

3.1 Finite Element Analysis

Models can be divided by temporal, thermal and spatial criteria. The choice of model depends on the availability of data and the research question. For this study, a local site-specific model, simulating the transient development of the thermal regime from an initial condition to the current state and the future, under the influence of a chilled foundation, is of interest. Reasonable assumptions and/or simplifications of the reality are often inevitable.

The numerical simulation for this study is based on the finite element method. Various software are available to handle finite element analysis. The finite element method (FEM) is useful in case of complex geometry and material behaviour. The method is a numerical solution approach for solving partial differential equation (PDE) problems. The partial

differential equations are a mathematical description of the physical processes within the model domain and are derived by applying a statement of conservation to a representative elementary volume (REV). Characteristic properties can be defined for the REV, which represents the smallest finite control volume within the domain. The statement of conservation relates the change in storage within the REV to the flow process in or out of the REV.

A discretization of the domain into 'finite elements' results in a 'meshed' model domain, creating a finite number of well defined elements and points called nodes. The PDE can be described for each element for the value of the dependent variable at each node. Therefore the discretization of the model domain allows for the application of partial differential equations in a semi-continuous way over the entire domain, resulting in a series of equations which can be solved using linear algebra.

3.1.1 FEM with GeoStudio TEMP/W

The commercially available software GeoStudio TEMP/W + TEMP3D Version 2021.3 is used for this study. *GeoStudio is an integrated, multi-physics, multi-dimensional, platform of numerical analysis tools developed by GEOSLOPE International Ltd. for geo-engineers and earth scientists* (GEOSLOPE International, Ltd., 2020). The TEMP/W formulation is developed to allow the study of transfer in porous media. This section is based on the handbook by GEOSLOPE International, Ltd. (2020), focusing on the fundamentals for setting up a transient heat transfer model to study the permafrost dynamics under a cooling plate in TEMP/W.

The statement of conservation in the TEMP/W formulation is based on the first law of thermodynamics which states the law of energy conservation in a closed system: Energy can not be destroyed nor created, it can only be transformed. The heat inflow and outflow terms are associated with its respective control volume (dxdydz). Based on the law of energy conservation, the rate of change of the amount of thermal energy stored in the system must be equal to the difference in rate of inflow and outflow of the system. Soil is a porous media comprised of water/ice, air and soil particles. The governing heat transfer process in soil is conduction thus by neglecting convection and the latent heat of vaporization, the conservation statement can be written as (GEOSLOPE International, Ltd., 2020):

$$\left(C_p + \rho_w h_{sf} \frac{\partial \Theta_{uwc}}{\partial T}\right) \frac{\partial T}{\partial t} = \frac{\partial}{\partial x}\left(k \frac{\partial T}{\partial x}\right) + \frac{\partial}{\partial y}\left(k \frac{\partial T}{\partial y}\right) + \frac{\partial}{\partial z}\left(k \frac{\partial T}{\partial z}\right) \tag{3.1}$$

where the left part is the storage term composed of C_p the volumetric heat capacity, ρ_w the density of water, h_{sf} the latent heat of fusion, Θ_{uwc} the volumetric unfrozen water content.

The right side is the heat flow term caused by the respective temperature gradient in each direction and the thermal conductivity k.

Material models

Two material models are available to model the soil's ability to store and transfer heat: a full thermal model and a simplified thermal model. The simplified thermal model does not take into account temperature dependent soil parameters, but assumes that all latent heat is released or absorbed at a phase change temperature. The simple model can be used for materials such as insulation where phase change properties are not of significance.

The full thermal model enables to specify thermal conductivity k [(kJ/sec)/(m.°C)] and the normalized unfrozen water content Θ_{uwc} [-] as a function of temperature. Also, an unfrozen ($C_{p,th}$ [J/(m³.°C)]) and frozen ($C_{p,fr}$ [J/(m³.°C)]) volumetric heat capacity along with the in-situ volumetric water content Θ_w [-] can be defined.

Therefore, in the full thermal model, the change in sensible energy is controlled by the volumetric heat capacity in frozen and unfrozen state and the in-situ volumetric water content. The thermal conductivity changes with temperature and the normalized unfrozen water content controls the rate of change of latent heat of fusion with change of temperature. An overview of input parameters is given in Table 3.1. The thermal parameters for this study are calculated following the formulation presented in subsection 2.2.2.

Table 3.1: Input parameters for TEMP/W for the respective thermal models, where n is porosity and T is temperature.

Parameter	Simple Thermal Model	Full Thermal Model
Thermal Conductivity	k_{fr}= const., k_{th}=const.	k(T)
Volumetric Heat Capacity	$C_{p,fr}$= const., $C_{p,th}$=const.	$C_{p,fr}$=const.,$C_{p,th}$ = const.
Normalized Unfrozen Water Content	-	$\Theta_{uwc} = \frac{\Theta_{uwc}}{n}(T)$
In-situ Volumetric Water Content	Θ_w	$\Theta_w = n$

Geometry and Mesh

Meshing in TEMP/W is fully automatic, handles complex geometry and ensures mesh compatibility over regions. Before generating the mesh an approximate global element size can be specified. Regional alterations of the element size is possible by specifying the element edge length as either length or ratio of global element size or by specifying the number of divisions along an edge. It is recommended to limit the alterations, so to choose an appropriate global element size and only adjust limited locations. Furthermore, it is recommended that the mesh structure is chosen similar to the geometry, here unstructured quad

and triangle mesh is the most suitable. A surface layer option is available in TEMP/W 2D, which can be generated after the main soil region is generated. The surface layer is recommended for simulations including phase change. It allows to *numerically deal with rapid and dramatic boundary changes* (GEO-SLOPE International Ltd, 2014). The layer is finely meshed with quadrilateral elements to *ensure optimum numerical stability during the solution* (GEO-SLOPE International Ltd, 2014). Quadrilateral elements are preferred as ground surface processes, such as heat flow in this case, usually have a steep primary gradient perpendicular to the surface. Results can vary greatly when triangular elements are present at the ground surface relative to the orientation of the elements. The density can be controlled by defining mesh layers in the surface layer. IN TEMP/W 3D however, no automatic surface layer mesh option is available so regions must be created to ensure finer meshing in the top layers.

Also, to avoid numerical issues rounded surface slope changes are preferred over angular slope breaks. Some guidelines are followed when generating the mesh as proposed in GEO-SLOPE International Ltd (2014):

- All elements, except surface layer elements, should be visible to naked eye at 100 % zoom factor.
- First analyses are made with a maximum of 1000 elements, the mesh density is increased to refine the analysis in selected areas.

Boundary Conditions

Boundary conditions can be applied in form of functions or constants. Each boundary condition can be applied to a region, therefore a region must be split when a boundary condition changes. Here, only thermal boundary conditions are relevant. Boundary conditions can be specified in form of values over time for a certain period and then cycled through the entire analysis, or values can be defined for the entire analysis time. Dependent on the nature of the function, forcing data can be applied in form of step or spline functions. For example, if monthly changes are modelled, forcing data can be applied in form of mean monthly values resulting a step function. The detailed choice of boundary conditions will be elaborated for each study.

3.2 Verification and Validation of Models

Numerical simulations are increasingly used to simulate real life problems and are used as decision making tools (Sargent, 2013). The reliability of a simulation model is addressed by the verification and validation process. The Sargent Circle presented in Figure 3.1, developed by the Society of Computer Simulation in 1979 (SCS Technical Committee on Model Credibility, 1979) represents a simplified illustration of a validation and verification approach for modelling. The dotted lines show the steps involved to assess the models reliability. The problem entity is the problem that is studied or in other words the physical system, the conceptual model is the mathematical formulation of the studied processes, so a mathematical description of the studied problem. It includes partial differential equations, constitutive equations, geometry, initial conditions and boundary conditions. When the conceptual model is implemented in a computer it is referred to as computerized model. Three major tasks can be identified in the validation and verification process of a model: conceptual model validation, computerized model verification and operational validation. The conceptual model validation is defined as the assessment of correctness of chosen features and associated mathematical formulations for the conceptual model in order to represent the problem. The verification of the computerized model includes checking the implementation of the conceptual model and the computer programming for errors. This step can be subdivided into two tasks, the code verification and calculation verification (Thacker et al., 2004). The operational validation aims to quantify the accuracy of modelling results in view of the real situation, represented by e.g. experimental results, field data.

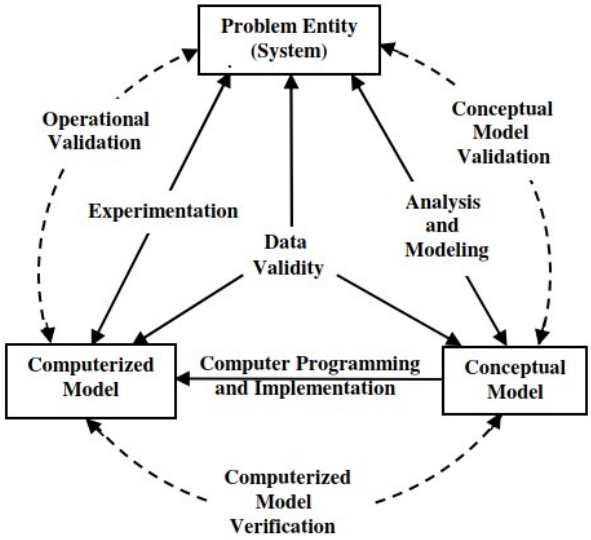

Figure 3.1: A simplified illustration of a validation and verification process for modelling (Sargent, 2013).

The conceptual validation includes the assessment whether geometry, boundary conditions and governing physical processes for this study are suitable. The suitability of geometry and boundary extents are tested during modelling in an iterative process to ensure no interference of boundary constraints. Also, limitations to the results of the numerical study caused by choices in the conceptual model will be stated.

In this study the code verification is not of interest since a verified software is used. The software is verified against common benchmarks and numerous simulation files showing the verification process of the software can be accessed online (GeoStudio, nd).

The calculation verification on the other hands is of interest. The software has integrated tools to check the convergence of each computed result. Convergence is reached when equal successive solutions within a specified tolerance or maximum number of iterations are computed. In TEMP/W two parameters can be defined for each analysis: significant figures or minimum difference. Minimum difference allows the user to specify a maximum temperature difference for which each successive nodal results are checked against. The significant figures value determines to which precision two successive iterations are compared. In other words, it states how many digits of a number carry meaning in terms of convergence, an example is presented in GEO-SLOPE International Ltd (2014). The default values in TEMP/W for maximum temperature difference is 0.1 °C and the significant figures is 2 which are adopted for this study and only alternated if convergence issues make it necessary. Convergence can be evaluated in a mesh view, showing unconverged nodes or by graphs. Options include plotting iteration versus unconverged nodes, which aids in determining the number of required iterations to reach convergence or time steps versus unconverged nodes. Furthermore an under-relaxation criteria in form of a thermal-under relaxation rate can be set. This criteria is required in highly-non linear analysis to mitigate divergence due to large variations of material properties. If the criteria is set to 1 no under-relaxation is included, or in other words no variance of material properties is allowed to achieve convergence. For analyses including phase change an under-relaxation rate of less than 1 is required. The default value is set to 0.1 and adopted for this study and only iterated if required due to convergence issues. The calculation verification of the analysis is satisfied when no unconverged nodes are present at any time step. This verification procedure is performed for each analysis of this study.

The operational validation in this study includes numerous tasks. First, the calibration of the model, where soil properties, geometry and boundary conditions are chosen and tested.

Further on, the performance of the model is quantified by comparing computed ground temperature profiles to recorded profiles in the location of the thermistor strings. This gives a quantitative value for the accuracy of the model and the reliability of simulation results. However, uncertainties in regards to boundary conditions for future modelling will always apply and can not be tested since it contains projected future data.

The 'best fit' is determined quantitatively by the Root Mean Square Error (RMSE) by calculating the daily or monthly $RMSE_d$ of observed and modelled temperature for each depth on each day or each month and summing $RMSE_d$ over the days or months in the year to obtain the total $RMSE$:

$$RMSE_d = \sqrt{\frac{1}{n}\sum_{i=1}^{n}\left(T_{obs,i} - T_{mod,i}\right)^2} \tag{3.2}$$

$$RMSE = \sum_{d=0}^{365} RMSE_d \tag{3.3}$$

where n is number of temperature measurement per day or month (for every depth), T_{obs} is the observed temperature in the field and T_{mod} is the modelled temperature. The daily or monthly RMSE is used to analyse the fit of the model at different time slices whereas the total RMSE gives an indication of the overall fit.

Chapter 4

Main Characteristics of the Study Site Miljøstasjon in Longyearbyen

For the development of a suitable model project specific information must be gathered, processed and analysed. This chapter introduces the key study *Miljøstasjon i Longyearbyen* or environmental centre in Longyearbyen, and presents available project related information. The compiled data is retrieved from meetings, emails, construction site visits and through access to the project online database, Interaxo, where construction relevant files such as drawings, pictures, etc. are stored. In the following section, for information retrieved by meetings or mails the respective person is cited. The project client is Longyearbyen Lokalstyre, the contractor is CONSTO AS and the consultant firm for the design of the cooling plate is Norconsult AS.

First an overview of the project is given with a special focus on the foundation system, subsequently the collected data is presented and analysed.

4.1 Project Overview

A new environmental station (Miljøstasjon), or recycling centre, is currently under construction in Longyearbyen on Hotellneset, a peninsula close to Svalbard Airport. Its relative location to town and to the Svalbard Airport is shown in Figure 4.1b. Construction started in August 2020 and trial operation is planned for October 2021 with final handover in April 2022. The service lifetime for the building is 50 years from handover. The building is divided in recycling areas for industrial and private waste as well as facilities for workers such as changing rooms, lunch room, bathrooms and meeting rooms. The inside temperature on

the ground floors is designed to be around +15 °C (Grande, L. O., personal correspondence, 11 March 2021). A conceptual illustration of the outside from Longva arkitekter (nd) is shown in Figure 4.1a.

The area of interest lies close to the coast line in an area of warm permafrost, presumably saline as well due to its vicinity to the sea. A special foundation solution is developed to transfer loads into the ground and assure its structural integrity during the service lifetime.

Primarily a pile foundation was considered for the project, consisting of end bearing piles founded on the bedrock in 30 metres depth. However, the area lies in a fault zone, thus lateral loading must be accounted for, which makes a pile foundation a very cost intensive solution (Braun, R.-H., project leader Lokalstyre, personal correspondence, 26 February 2021).

Finally, it was decided that due to the extents of the footing, the present geology and soil characteristics as well as the high import costs related to construction with concrete on the island a heat pump cooled slab foundation is the most cost-effective and technically suitable solution (Grande, L.O., consultant Norconsult AS, personal correspondence, 29 June 2021).

During the site investigation boreholes were drilled, located close to the centre points of the future outer walls of the structure. Some disturbed samples were taken during the drilling process and the laboratory analysis for soil properties was minimal. Some soil parameters for the location were suggested by Lars Olav Grande (personal correspondence, 12 February 2021) as following: soil type of silty sand, assuming a homogenous layer until bedrock in approximately 30 metres depth. Thermal parameters should be adopted from literature.

Further on, two thermistor strings were installed in the boreholes to measure the temperature in the ground over time. The geometry of the footing area and the relative location of the boreholes in respect to the foundation area are shown in Figure 4.2.

(a) Overview of the building site in regards to the town centre, the airport and the coastline (by the author).

(b) Illustration of the new environmental station (Longva arkitekter, nd).

Figure 4.1: Overview of project site and conceptual illustration of the new environmental station.

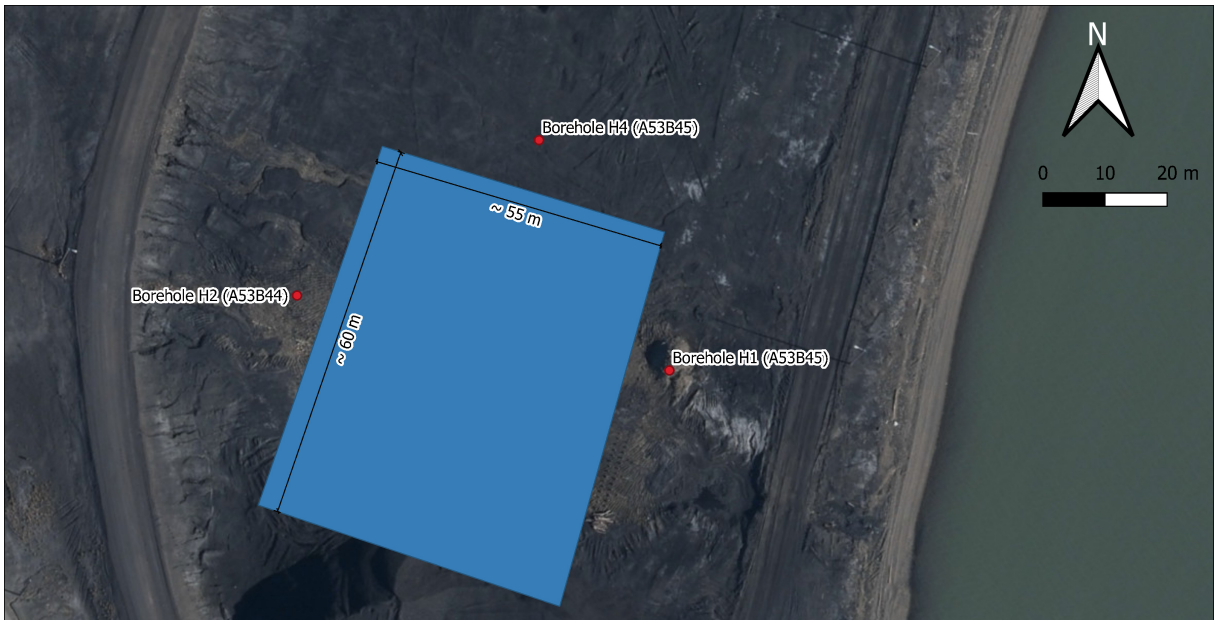

Figure 4.2: Location of boreholes and thermistor strings respectively in relation to the foundation area marked by the blue rectangle.

4.1.1 Foundation Design

The footing extends over an area of approximately 3400 m^2 with a width of about 55 m and a length of 60 m. The construction of the foundation system started by levelling of the terrain and removal of the top thawed layer, which mainly consisted of coal. During the removal of the active layer, solid ice layers were encountered on top of the permafrost and removed. The ground was reported to be frozen underneath the active layer. Drainage trenches were installed around the premises to lead surface water away and the excavated area was filled with clean gravel of varying thickness to create an even surface. The gravel layer is designed to be frozen and should transfer the loads evenly into the ground. On top of the gravel layer, 62 different loops of cooling pipes are mounted to the reinforcement bars and casted in 5 cm of concrete. On top of the concrete a 30 cm XPS insulation layer was placed. A membrane on top of the insulation layer is added to avoid moisture influx. The structure is founded on pre-cast beam elements which are directly placed on the membrane and insulation, transferring the loads to the cooled gravel (Grande, L. O., personal correspondence, 29 June 2021). Photos of the construction process, retrieved online from the Interaxo database, show the construction process of the foundation in Figure 4.3 to 4.4. The construction drawings of the foundation design can be found in Appendix B.

There are three different circulation systems to control the cooling of the foundation. About 30 000 metres of cooling pipes are placed. The layout is designed to homogeneously

cool the plate to the chosen cooling temperature. Twelve thermistors are planned to be installed in the area to constantly measure the temperature under the cooling plate in the ground (Grande, L. O., personal correspondence, 12 February 2021) but were not in place at the time of this study (Braun, R.-H., personal correspondence, 26 February 2021). The cooling was started on 29 December 2020, but temperature measurements conducted under the plate in mid December, showed ground temperatures of around -5 to -6 °C. Therefore the ground was frozen at the time of construction. The design cooling temperature is set to achieve a mean annual temperature of -5 °C. The operation of the cooling plate was handed over to a subcontractor (Grande, L. O., personal correspondence, 01 March 2021). Numerous attempts by the author to establish contact to the subcontractor to obtain more detailed information about the current cooling temperature and energy usage were unsuccessful. Thus no detailed information about the cooling system is available.

(a) 03.08.2020; building site before construction.

(b) 17.08.2020; levelling of terrain.

(c) 19.08.2020; clean base layer on top of compacted fill.

(d) 23.08.2020; placement of reinforcement on gravel layer.

Figure 4.3: Construction process of the foundation system, part 1; (photos retrieved online from the Interaxo database with the permission of Rainer-Helge Braun, Longyearbyen Lokalstyre).

(a) 14.09.2020; placement of reinforcement bars.

(b) 17.09.2020; placement of cooling pipes.

(c) 28.09.2020; fixing cooling pipes to reinforcement.

(d) 30.09.2020; casting of concrete slab.

(e) 05.10.2019; outlet for cooling pipes and casting of concrete.

(f) 12.10.2020; placement of XPS insulation.

Figure 4.4: Construction process of the foundation system, part 2 (photos retrieved online from the Interaxo Project Hotel with the permission of Rainer-Helge Braun, Longyearbyen Lokalstyre).

4.2 Temperature Data

GeoPrecision thermistor strings were placed in two of the four boreholes in August 2019, east and west of the building. One string in the eastern borehole H1 and one in the western borehole H2. The eastern string was removed at start of construction in August 2020 and stored indoors until November 2020, when it was reinstalled in the northern borehole (Grande, L. O., personal correspondence, 23 February 2021). During the construction process, an embankment was placed on top of the western borehole in January 2021. Some attempts by the author to secure the borehole were made, the pipe was extended to end just under the top level of the embankment, but unfortunately no readings could be obtained any more.

The northern and western borehole were last accessed on the 19th of February and an attempt to access the northern borehole more recently was unsuccessful since a big container was placed on top of it (Ingebrigtsen, T. R., CONSTO AS, personal correspondence, 01 July 2021). For further discussion, the thermistor strings will be referred to by the name of their respective borehole.

Photos of the thermistor strings relative to the construction site are shown in Figure 4.2 and Figure 4.5. Detailed information about the data logger and thermistor string type as well as calibration data for the thermistors are not available. However, a conceptual picture of a GeoPrecision thermistor string is shown in Figure 4.6 to provide a better understanding of the set up. Each data logger can be accessed via a Wireless-USB Dongle, which allows wireless communication between data logger and computer when in sufficient range. Permission to access the site was granted by the contractor, CONSTO AS, and client, Longyearbyen Lokalstyre, respectively. The data was downloaded and saved as comma delimited file for further processing. The 21 thermistors are spaced out along the string according to Table 4.1 and measure temperature in the respective depth. There are uncertainties about the set-up of the thermistors and their precise depth since there is not detailed documentation about the initial installation of the thermistor strings available. The logging interval is 21600 seconds (6 hours) for both data loggers. The timeline of available records for each location is summarized in Table 4.2.

(a) Borehole H1.

(b) Borehole H4.

Figure 4.5: Photos of the thermistor string location in February 2021. The embankment at H1 was partially built at the time of the picture.

Figure 4.6: GeoPrecision thermistor string; data logger is integrated in the metal casing and thermistors are placed in variable spacing along the string (GeoPrecision, nd).

Table 4.1: Placement of thermistors along the string: first sensor measures air temperature, second sensor measures ground surface temperature and ground temperature is measured down to 20 metres below top of the terrain.

Thermistor number [#]	Depth from top of terrain [m]	Comment [-]
1	+ 1.0	Air temperature
2	0.0	Surface temperature
3	-0.5	Ground temperature
4	-1.0	Ground temperature
5	-1.5	Ground temperature
6	-2.0	Ground temperature
7	-2.5	Ground temperature
8	-3.0	Ground temperature
9	-3.5	Ground temperature
10	-4.0	Ground temperature
11	-4.5	Ground temperature
12	-5.0	Ground temperature
13	-6.0	Ground temperature
14	-7.0	Ground temperature
15	-8.0	Ground temperature
16	-10.0	Ground temperature
17	-12.0	Ground temperature
18	-14.0	Ground temperature
19	-16.0	Ground temperature
20	-18.0	Ground temperature
21	-20.0	Ground temperature

Table 4.2: Timeline of ground temperature measurements from thermistor strings in respective boreholes.

Borehole	Installation date (approximately)	Data available from	to	Limitations
H1	26.07.2019	01.10.2019	10.02.2021	embankment constructed in January 2021
H2	26.07.2020	01.10.2019	01.08.2020	removed due to construction work
H4	10.10.2020	01.11.2020	10.02.2021	inaccessible later on as container placed on top

4.2.1 Ground Thermal Regime

The collected data files are processed using Python to create plots and datasets to analyse the thermal regime and further compare it to modelling results. For the analysis of the ground thermal regime only measurements from the ground surface and below are included. A summary of all available ground temperature measurements for this study is illustrated in a contour plot in Figure 4.7, which shows the respective dataset from the thermistors versus time. In the contour plot it is visible that deeper layers at H2 (west) are colder than at H1 (east). Also the effects of the embankment constructed in January 2021 on top of H2 are visible, as the temperatures measured at H2, shown on top in Figure 4.7, are much warmer compared to H4 shown on the bottom in Figure 4.7.

The ALT for each location is determined by interpolation of depth just above and below 0 °C. The DZAA is determined by taking the difference between maximum and minimum mean annual values for each depth and interpolating between the depth corresponding to a temperature difference of just above and below 0.1 °C. This is an approximation since the temperature curve is not linear but results in sufficient accuracy for this study.

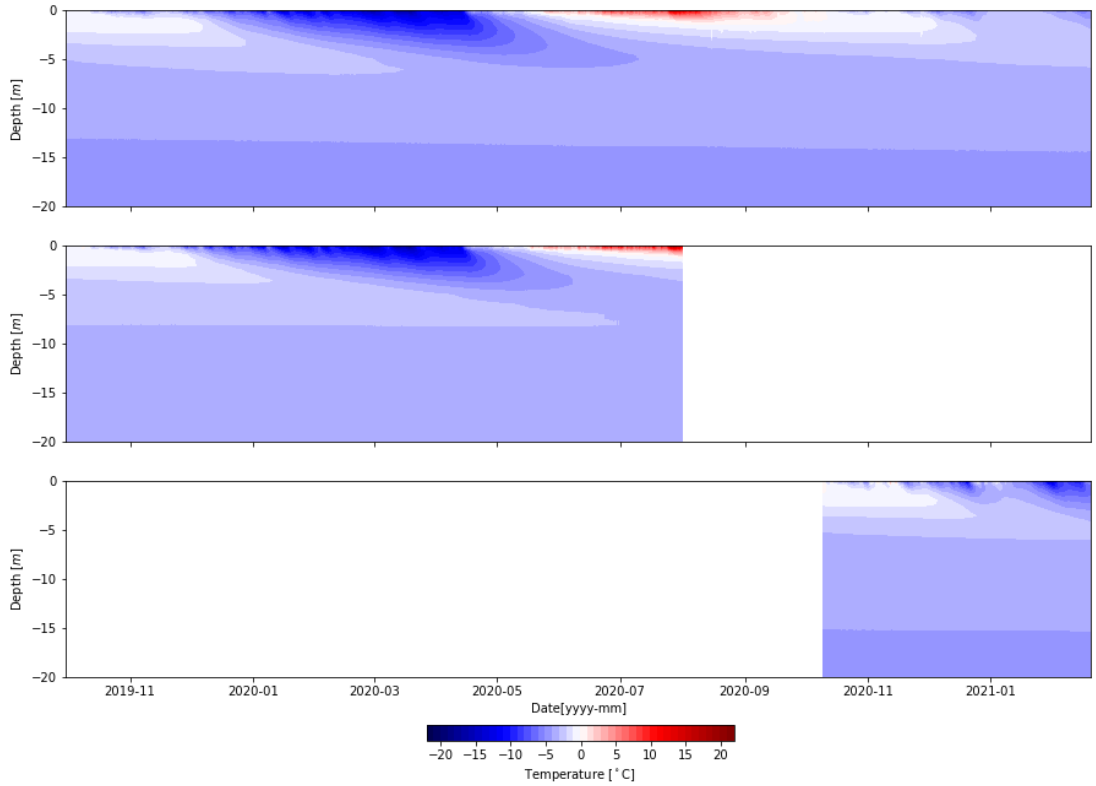

Figure 4.7: Contour plot of recorded temperature versus time with H2 (west) on top, H1 (east) in the middle and H4 (north) on the bottom. It is visible that the permafrost temperature at H2 and H1 are colder than at H4.

Thermal Profile H2 (West)

The western thermistor string in H2 provides the most consistent temperature records from October 2019 to February 2021. However, an embankment was constructed on top of the thermistor, therefore temperature readings from January 2021 onwards do not represent the natural ground thermal regime and were consequently dismissed for further analysis.

The maximum and minimum envelopes are shown in Figure 4.9a. These were used to determine the ALT and DZAA respectively. The active layer thickness is 1.47 metres and the depth of zero annual amplitude is at 9.66 metres. The entire dataset ranging from October 2019 to January 2021 is represented in a trumpet curve in Figure 4.9b where ALT and DZAA are also indicated. The permafrost temperature at 20 metre depth lies at -4.3 °C and the mean annual ground temperature ranges between -4.3 °C and -3 °C. It is visible that the ground is

adjusting to a warmer climate on the top as the trumpet is shifting towards warmer temperatures. This explains the temperature gradient below DZAA and for MAGT. The ground surface temperature ranges between -15 °C in March to approximately 8 °C in July.

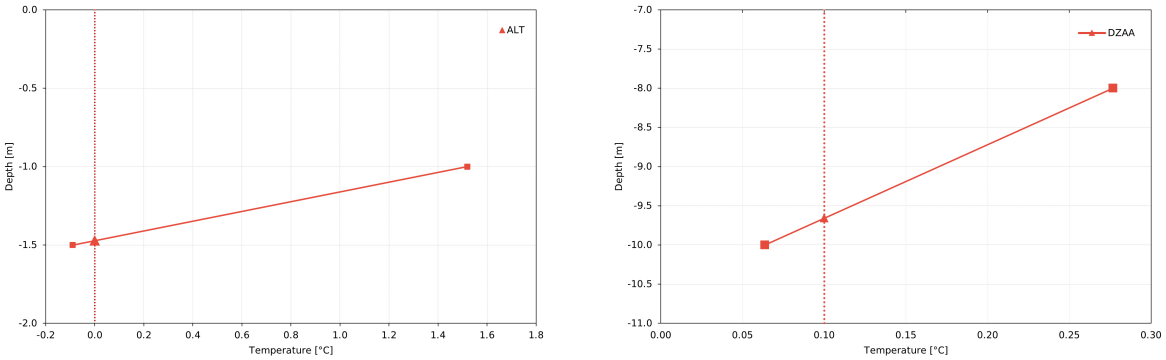

(a) H2: ALT equals 1.47 metres.

(b) H2: DZAA lies at 9.66 metres.

Figure 4.8: Estimation of active layer thickness and depth of zero annual amplitude in H2.

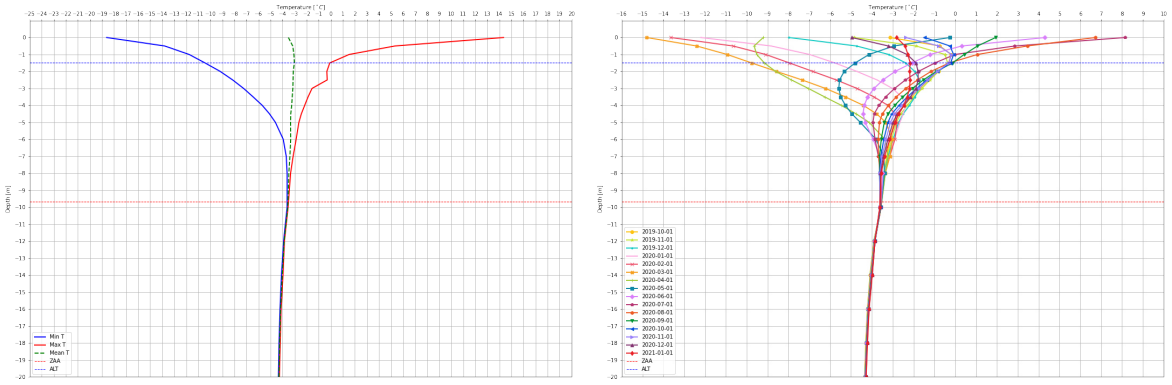

(a) Maximum and minimum envelopes for the H2 dataset resulting in an ALT of 1.47 metres, a DZAA of 9.66 metres and a MAGT of 4.3 °C.

(b) Annual temperature trumpet consisting of mean monthly temperature profiles in H2.

Figure 4.9: Temperature profiles in H2.

Thermal Profile H1 (East)

H1 provides temperature records from October 2019 to July 2020. Hence the dataset does not represent a full year and misses warming months from August and September 2020. The maximum and minimum envelopes are presented in Figure 4.11a. Again, the maximum and minimum ground temperatures are used to determine ALT and DZAA. The active layer thickness is 1.32 m and the depth of zero annual amplitude is at 9.81 metres. The entire dataset ranging from October 2019 to January 2021 is presented in a trumpet curve in Figure 4.11b, where ALT and DZAA are indicated.

The permafrost temperature at 20 metres is -3.8 °C and the mean annual ground temperature lies between -3.8 °C to -3 °C. The ground surface temperatures range between -15 and +8 °C.

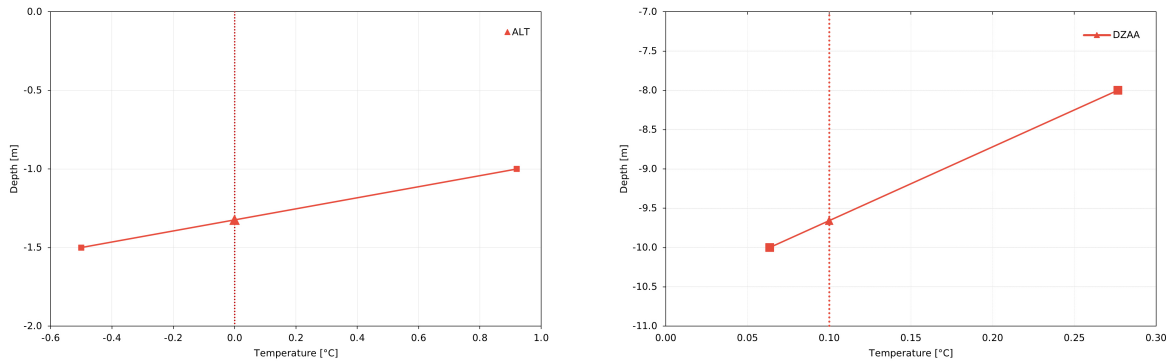

(a) H1: ALT equals 1.32 metres.

(b) H1: DZAA lies at 9.81 metres.

Figure 4.10: Estimation of active layer thickness and depth of zero annual amplitude in H1.

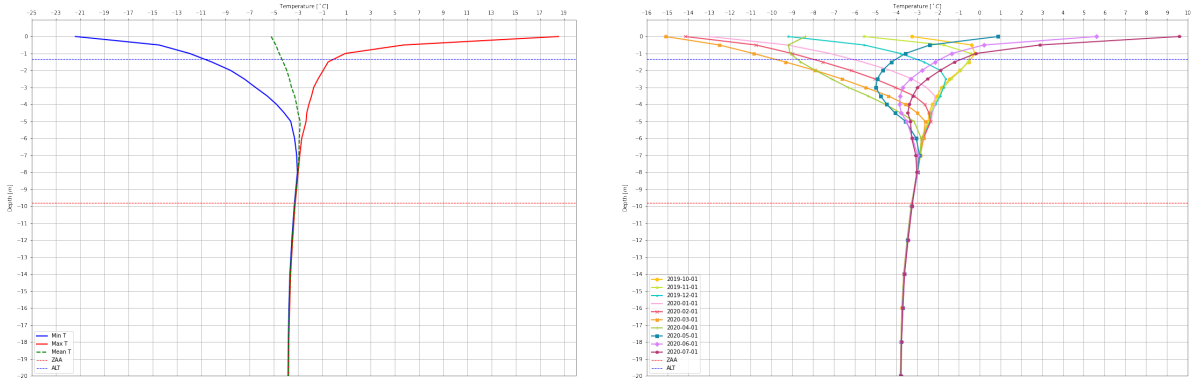

(a) Maximum and minimum envelopes for the H1 dataset; ALT is 1.32 metres, DZAA is 9.81 metres and MAGT is -3.8 °C.

(b) Annual temperature trumpet consisting of mean monthly temperature profiles in H1.

Figure 4.11: Thermal profile in H1.

Thermal Profile H4 (North)

For H4, temperature measurements from three consecutive months are available, November 2020 to January 2021. The active layer is not determined since the data set does not cover sufficient time. However the DZAA can still be estimated. The DZAA for this location lies at 9.8 metres depth and the permafrost temperature at 20 metres depth is -4.3 °C. The maximum and minimum envelopes are shown in Figure 4.12a and the mean monthly temperature profiles are presented in 4.12b.

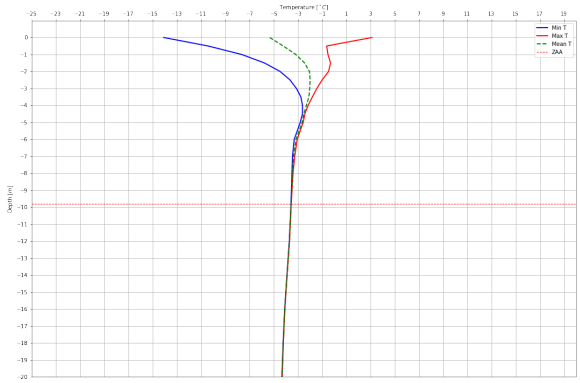

(a) Maximum and minimum envelopes for the H4 dataset; DZAA lies at 9.81 metres and MAGT is -4.3 °C.

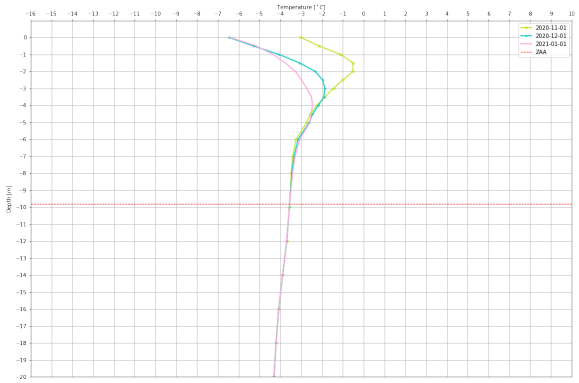

(b) Annual temperature trumpet consisting of mean monthly profiles in H2.

Figure 4.12: Thermal profile in H4.

Discussion of Thermal Profiles

The ground thermal regime supplies a lot of information about the past and current climate in a location. All three profiles show that the ground is adjusting to warmer climate as the temperature, also below DZAA, is getting colder in deeper layers. This is explained by the lag time that the ground experiences over depth. Deeper layers take more time to respond to climatic conditions than shallower layers.

A comparison of the three obtained temperature profiles shows differences in MAGT even though the boreholes are located within 60 metres of each other. The western and northern temperature regimes, represented by H2 and H4, show approximately the same temperature at 20 metre depth of -4.3 °C, whereas in the east, represented by H1, it is 0.5 °C warmer at -3.8 °C. The colder MAGT of H2 and H4 compared to H1 could be explained by its vicinity to the sea, which is expected to warm the ground as water bodies act as major heat sources.

The DZAA is comparable in all three locations, the thermal profiles in H1 and H4 show a 20 cm deeper zero annual amplitude than in H2.

The ALT differs by 15 cm between eastern and western side, H2 shows 1.47 metres of seasonally thawed ground compared to 1.32 metres at H1. The ALT is dependent on the surface temperature during thaw season, therefore the ALT at H4 is not obtained from the measurements as the effect of warming summer months is not represented in the data set. A comparison of maximum and minimum envelopes for H1 and H2 respectively is shown in Figure 4.13, where it is visible that the trumpet in H1 is shifted to the left therefore to colder temperatures. However, H1 has a higher surface temperature amplitude which could also result from the fact that the data set is not fully representing a full year as opposed to H2.

Table 4.3: Comparison of the ALT, DZAA and ground temperature for the three temperature profiles at the project site.

Location [-]	Duration [-]	ALT [m]	DZAA [m]	GT at 20 m [°C]
H1	Oct 19 - Jul 20	1.32	9.81	-3.77
H2	Oct 19 - Oct 20	1.47	9.66	-4.30
H4	Nov 20 - Dec 20	-	9.81	-4.30

Figure 4.13: Comparison of maximum and minimum annual envelopes for H1 and H2 show that the ground thermal regime at H2 is colder than at H1 and DZAA and ALT are similar.

4.3 Climate Data

The closest weather station Svalbard Airport (ID: SN99840) is located approximately 1 km away from the project site as shown in Figure 4.1b. The station was established in 1975 and freely available climate data is provided online by The Norwegian Meteorological Institute (MET Norway) (nd) and can be accessed via the Frost API using Python.

Figure 4.14 shows a plot of the measured temperature from sensor 1 in the respective boreholes compared to the measured air temperature at Svalbard Airport. The comparison is made, on the one hand to ensure that the first sensor is placed above the ground and to measure air temperature, and on the other hand to see discrepancies between measured

values at site to measured values from the weather station.

It is visible that the measurements from the first sensor shows good correlation with the weather station data in winter months. In summer the measured values on site are higher. The higher measured temperatures in summer could result from heating of the plastic tube in which the thermistor is placed. The tube is directly exposed to sunlight and this can alter the temperature readings at sensor 1. However, the comparison of air temperature from the weather station and temperatures measured from thermistor 1 show good compliance. The trends are the same and the air temperature at Svalbard Airport is used for further modelling.

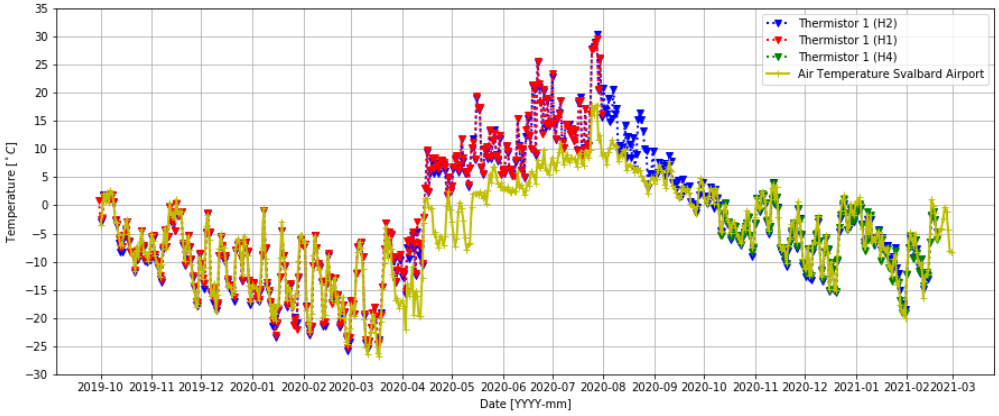

Figure 4.14: The comparison of measured air temperature from thermistor 1 in each borehole in blue, red and green respectively and air temperature recorded at the Svalbard Airport weather station in yellow.

Solar radiation data is not available for this study. Also, the surface albedo is unknown and snow depth is not measured on site. Since there are too many uncertainties in the climate data, the surface n-factors are estimated to link the measured air temperature to the ground surface temperature on site. The measured ground surface temperature from thermistor H2 and recorded air temperature data from Svalbard Airport for Autumn 2019 to Autumn 2020 are used to estimate seasonal n-factors.

First, the measurements at H2 from the second sensor are compared to the first sensor to check if the sensor is located approximately at the ground surface. From Figure 4.15 it is visible that on one hand the measurements from the second sensor oscillate much less than from the first sensor, on the other hand they are not smoothed like sensor three which indicates temperature deeper in the ground. Also, the construction of the embankment can be observed by the response in temperature variation amplitude from January 2021. The measurements from the second sensor are much smoother from beginning of January 2021. The measurements from sensor three are warmer in winter and colder in summer, which is also

reasonable as ground surface temperatures have a higher amplitude and not all heat is transferred into the ground. These observations lead to the assumption that the measurements from the second sensor can be used as ground surface temperature. Of course, uncertainties still apply whether the sensor is positioned flush with the ground surface.

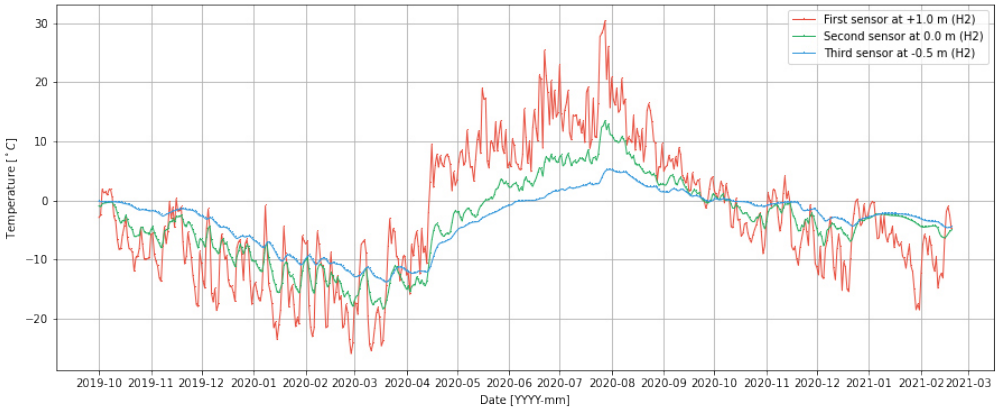

Figure 4.15: Temperature measurements for the first, second and third sensor respectively at H2; it is concluded that it is reasonable that the second sensor is placed on the ground surface as the temperature variation is less pronounced than for the first sensor but also not fully smoothed, like sensor 3, indicating ground temperature.

The estimation of the seasonal n-factors starts with the analysis of cumulative degree-days for air and ground temperature respectively as presented in Figure 4.16. The freezing index is the difference between maximum, in October 2019, and minimum, in May 2020, cumulative degree-days. The thawing index is the difference between minimum in May 2020 and maximum in October 2020, cumulative degree-days.

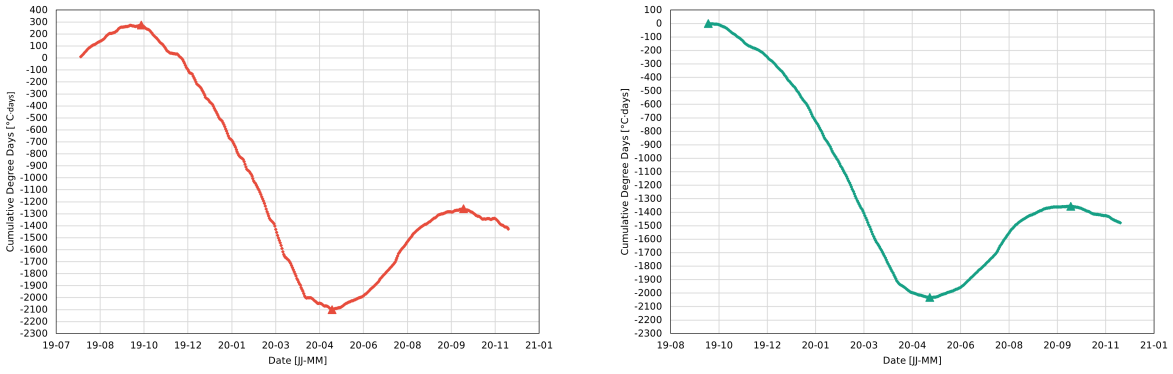

(a) Air Temperature.

(b) Ground Surface Temperature.

Figure 4.16: Cumulative degree days for air and ground surface temperature with an indication for minimum and maxima in autumn 2019, spring 2020 and autumn 2020 respectively.

The seasonal surface n-factor is then estimated according to Equation 2.2 and 2.3:

$$n_f = \frac{-2364.5}{-2030.8} = 0.859 \tag{4.1}$$

$$n_t = \frac{841.1}{675.5} = 0.803 \tag{4.2}$$

The measured and estimated ground surface temperature for the calibration period show a coefficient of determination of 0.89 (see Figure 4.17). A $n_f < 1$ indicates that the ground surface temperature is lower than the air temperature which can be explained by the insulation effect of the snow cover in winter. A $n_t < 1$ indicates that the ground is vegetated and the ground surface stays cooler than the air temperature in summer. The ground surface in thawing season at the project location is composed of sand, gravel and coal dust residue from the coal loading deck nearby which lead to the expectation of a $n_f > 1$, or in other words to warmer summer conditions at the ground surface than in the air. However, the measured and estimated GST for summer season correlate well and the recorded and estimated mean annual GST differ by 0.03 °C, therefore the estimation of $n_f < 1$ is adopted for further modelling.

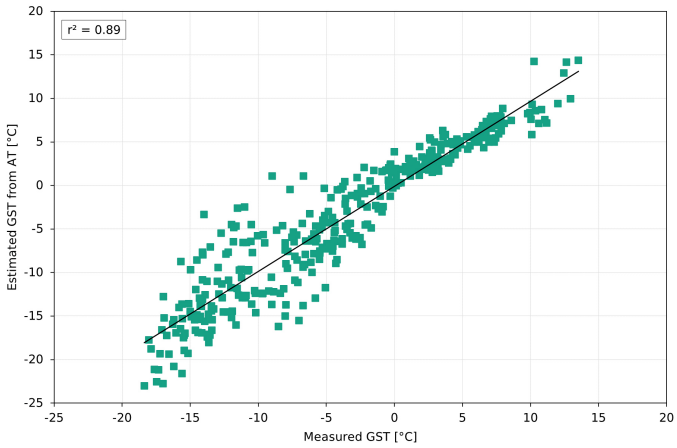

Figure 4.17: Measured ground surface temperature (GST) for the calibration period plotted against estimated GST using a n-factor modifier function. The r2 is 0.89 for the site, the modelled and estimated values agree well in thawing period. In freezing season a larger scatter is observed.

The calibration period for the n-factor reaches from autumn 2019 to autumn 2020. This results in high uncertainties for future modelling since the n-factor can vary between different annual periods due to different climatic conditions. More confidence would be achieved by estimating an average n-factor based on a long-term time series. However, the available data for this study allowed only for estimation of the n-factor for the chosen calibration period.

For future modelling it is important to consider this uncertainty.

4.4 Summary

The key features identified by analysing project related information and from the thermal analysis in view of modelling of the thermal regime are presented here:

- No detailed information about the design of the cooling system in regards to heat pump capacity, cooling fluid, pipe type, geometry or layout, cooling temperatures etc. is available. The structural design of the foundation system is known from construction drawings. The foundation system must be simplified for further modelling to account for the lack of information regarding the cooling system.
- The soil properties are mostly unknown. A soil type of silty sand will be used for further analyses.
- Bedrock is encountered in approximately 30 metres depth.
- Geothermal heat flux for the project site is unknown.
- Three locations are available with temperature measurements covering different time frames. H2 is the most consistent and can be used to compare full annual trumpets, ALT and DZAA. The H1 dataset can also be used for verification purposes of the model for the respective months as well as the DZAA but the ALT is assumed to be underestimated. The H4 dataset can only be used for verification purposes in November and December 2020.
- The ground is adjusting to warmer climate which is visible in all three temperature trumpets.
- The adjacent sea is assumed to have an impact on the study site as the MAGT in H1 (50 metres to the coastline) is 0.53 °C warmer than in H2 (110 metres to the coastline). However, sea temperature at the project site is unknown.
- A comparison of measured air temperature at the weather station and temperature measured at the sensor 1 metres above ground surface show a good correlation and lead to the conclusion that measurements from Svalbard Airport are a very accurate replication of air temperature on the the project site.
- Solar radiation, snow depth and surface albedo are not available for the study site.

- Seasonal n-factors achieve a good estimation of ground surface temperatures and can be adopted for modelling, but introduce uncertainties when constant n-factors are applied for long-term future predictions.

Chapter 5

Calibration and Operational Validation of the Model

This chapter contains the description of the calibration and validation process to create a reliable 3D model. Firstly, a 1D model is built to calibrate soil properties, secondly, a 2D model of a cross section is built to test boundary constraints and conditions. These analyses are performed on a 2D model to lower the computational cost. Thirdly, a 3D model is built, based on the 2D domain. The 3D model is first implemented to simulate the thermal regime in the ground without the effects of the cooling plate, to test the model's performance by comparing modelled mean monthly temperature profiles to measured field data.

The H2 dataset is the most consistent set and will therefore be put to use to calibrate the thermal properties of the ground. In order to reproduce the temperature profiles for the initial condition of the model, the H1 and H2 temperature profiles are used for comparison. All three data sets, thus H1, H2 and H4, are utilized to test the 3D model performance.

5.1 1D Model: Soil Properties

First, thermal parameters from literature are compiled to have a database for reference for the respective soil type and other materials used in this study. This is summarized in Table B.1. However, it is also very obvious that soil parameter can vary greatly also within the same soil type, as various factors, such as temperature, moisture and mineral content, etc. influence thermal properties of soil.

For this study, the soil properties are determined in an iterative simulation process, to reproduce the measured mean monthly temperature profiles in the ground. The accuracy is

quantified by the root mean square error between the modelled and measured daily temperature set, as explained in section 3.2.

A 1D model is built and the forcing data consists of recorded ground temperatures from location H2. The upper boundary condition is applied as a spline function of mean daily ground surface temperature measurements, thus readings from sensor 2 on string H2, as presented in Figure 5.1. The lower boundary condition is set to a constant temperature of -4.3 °C, equal to the mean annual ground temperature at 20 meter depth. The initial condition for the analysis equals the measured temperature profile on 01 October 2019 in H2. The model geometry replicates a 20 metre deep homogenous soil column and the same material is applied for the entire domain. A mesh is generated automatically with a chosen approximate global element size of 0.5 meters. The duration equals the number of days from 01 October 2019 to 30 September 2020 (366 days) and the time stepping is set to one day. The duration is chosen according to the recorded ground temperature data to cover an entire year of undisturbed in-situ measurements.

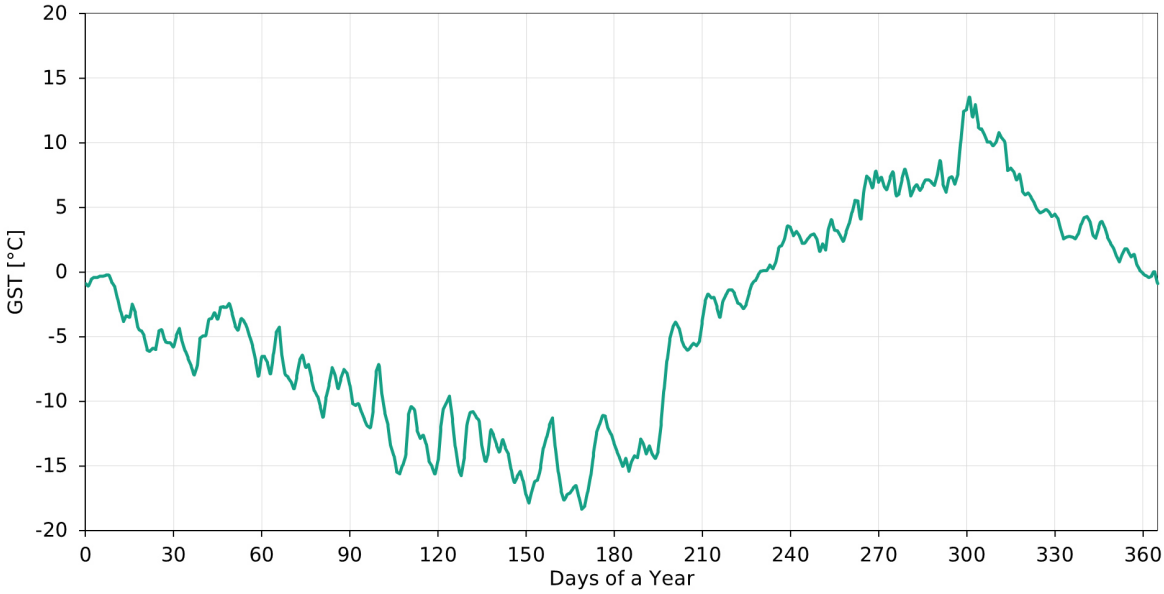

Figure 5.1: Spline function of measured ground surface temperature in H2, applied as upper boundary condition to calibrate soil properties.

The limited information about soil properties suggests a soil type of silty sand at the project location. The effective thermal conductivity is estimated following Equation 2.5 as proposed in subsection 2.2.2. The conductivity of air, water and ice respectively is constant, values are adopted from literature (Andersland and Ladanyi, 2004; French, 2007) and are summarized in Table 5.1. A fully saturated ground is assumed due to the proximity to the sea and a porosity of 23 % for dense silty sand (Andersland and Ladanyi, 2004) is chosen, assuming dense

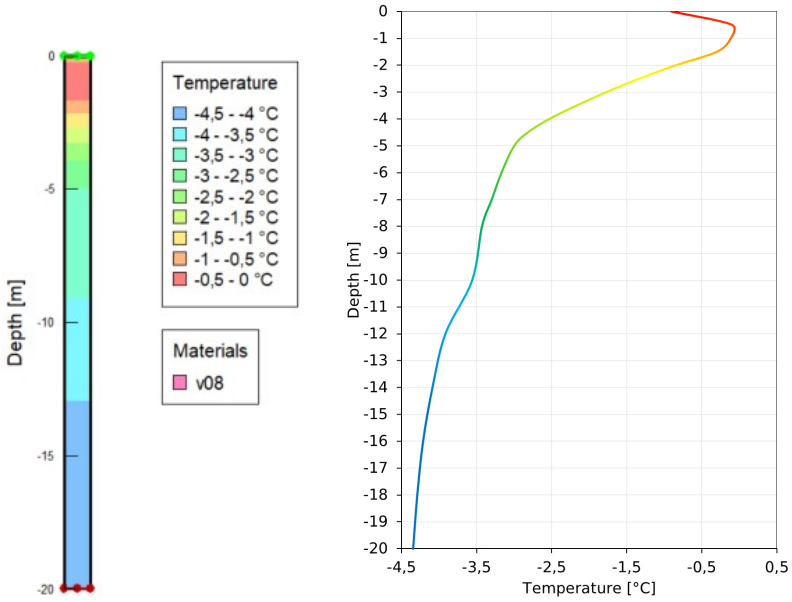

(a) 1D model in TEMP/W. (b) Initial condition for 01 October 2019 at H2.

Figure 5.2: 1D model domain with initial condition set to temperature profile from 1st of October 2019 as measured on site.

soil in this area.

The thermal conductivity of the soil particles is varied. Due to the lack of information about the mineralogy composition of the ground, a first estimate of the particle conductivity is computed by following Johansen's formulation presented in Equation 2.6 and assuming a Quartz content of 20 %. This results in a particle conductivity of 2.8 W/(m.°C) and in very unreasonable results in view of the temperature distribution in the ground. The ground profile is much warmer in the simulation than in measured condition, which indicates that the thermal conductivity is too high. The unfrozen water content for these analysis is kept constant, with α and β parameters adopted from Andersland and Ladanyi (2004) for silty soils, to be able to quantify the effect of the particle conductivity.

The most reasonable range for particle conductivity is found to be between 1.7 and 1.9 W/(m.°C), which is adopted for the further fine-tuning of the soil properties. For the fine-tuning, two values for particle conductivity as well as for α and β respectively are defined, which results in 8 combinations as presented in Table 5.2. The range of α and β parameters are adopted from Andersland and Ladanyi (2004) for various tested silty soils. It is important to note that the α and β parameters are soil specific and depend heavily on the moisture content of the specific soil. Therefore, the parameters are very uncertain in view of the real parameters, however the adopted values for α and β in this study show reasonable results.

The modelled ground temperature profile of each month is compared to the recorded

profile to observe the behaviour of the model for each set of parameters. The total RMSE for the modelled and measured daily temperatures for each set of parameters is summarized in Table 5.2. The smallest RMSE is achieved for parameter set v08, with an error of 0.38 °C. The results in form of mean monthly temperature profiles are presented in Figure 5.3 to 5.4. In October the modelled and observed temperature is very similar, since the modelling starts on 01 October. The simulation results in a colder regime in November and December, from January onwards until April the modelled temperature is slightly warmer, May until September show colder profiles in the simulation.

Also, it can be observed that the model does not produce more inaccuracy the longer the simulation is run, which indicates a good response of the model to the forcing data. The largest variation can be observed in June and July, where the RMSE of mean monthly temperature profiles is 0.61 and 0.58 °C respectively. Also, in all 12 reproduced mean monthly temperature profiles, the trend of the observed temperature profile is followed, which indicates a good fit of chosen soil properties.

Table 5.1: Summary of constant thermal properties for the silty sand adopted from (Andersland and Ladanyi, 2004) and assumed saturation of the soil.

k_i	k_w	k_a	n	S_w
[W/(m.°C)]	[W/(m.°C)]	[W/(m.°C)]	[-]	[-]
2.21	0.56	0.026	0.23	1

Table 5.2: Calibration of soil properties with different combinations of soil properties; v08 shows the best fit;the simulation for v08 was rerun including a surface layer which improved the RMSE.

Version	Particle conductivity	α	β	RMSE
[-]	[W/(m.°C)]	[-]	[-]	[°C]
v01	1.7	2	-0.5	0.51
v02	1.9	2	-0.5	0.58
v03	1.7	6	-0.5	0.65
v04	1.9	6	-0.5	0.57
v05	1.7	2	-0.3	0.66
v06	1.7	6	-0.3	0.49
v07	1.9	2	-0.3	0.73
v08	1.9	6	-0.3	0.38

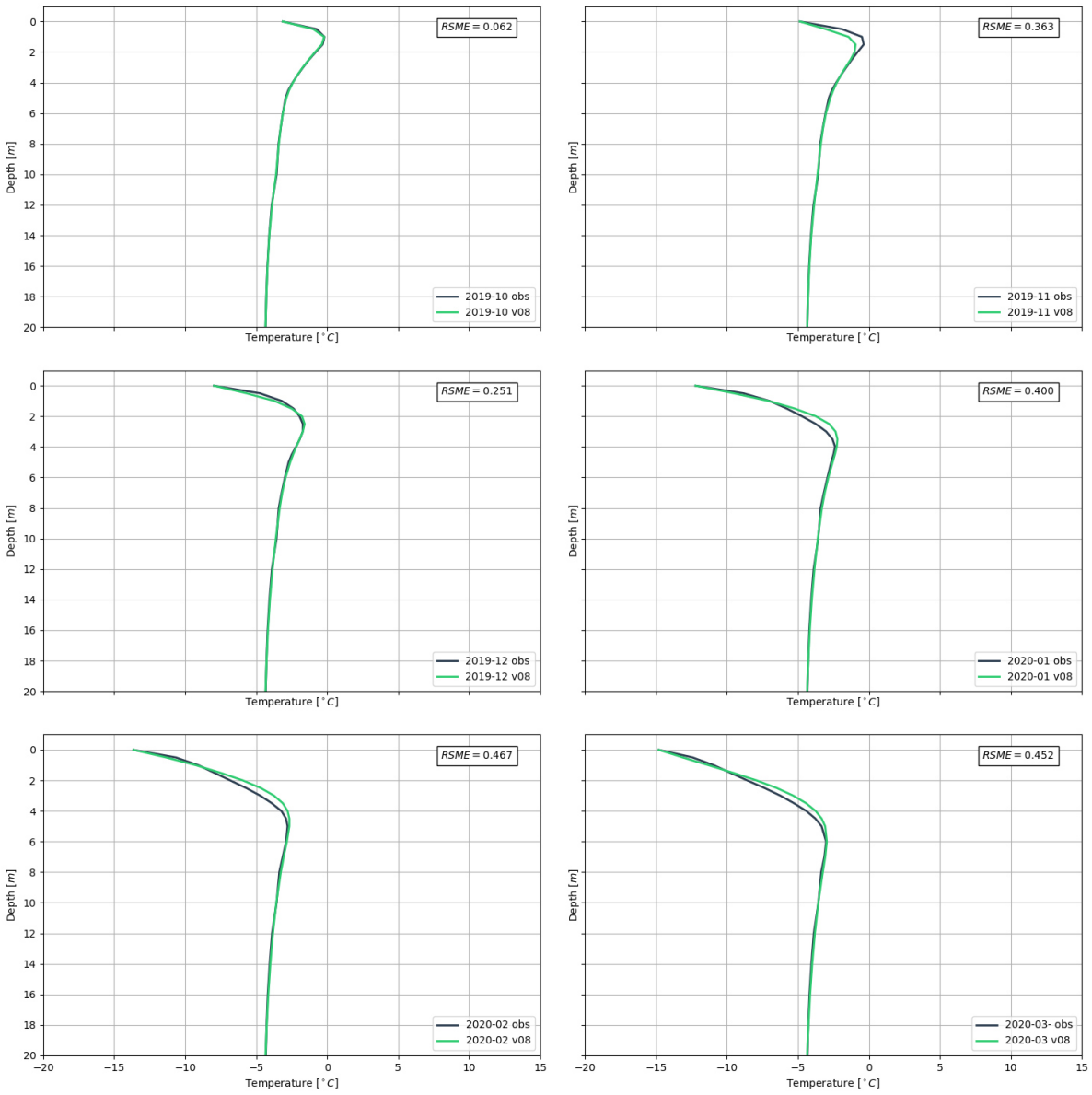

Figure 5.3: Comparison of modelled temperature profile (green) and measured temperature profile (grey) for the first of each month for calibration analysis v08 (Oct 2019 - Feb 2020).

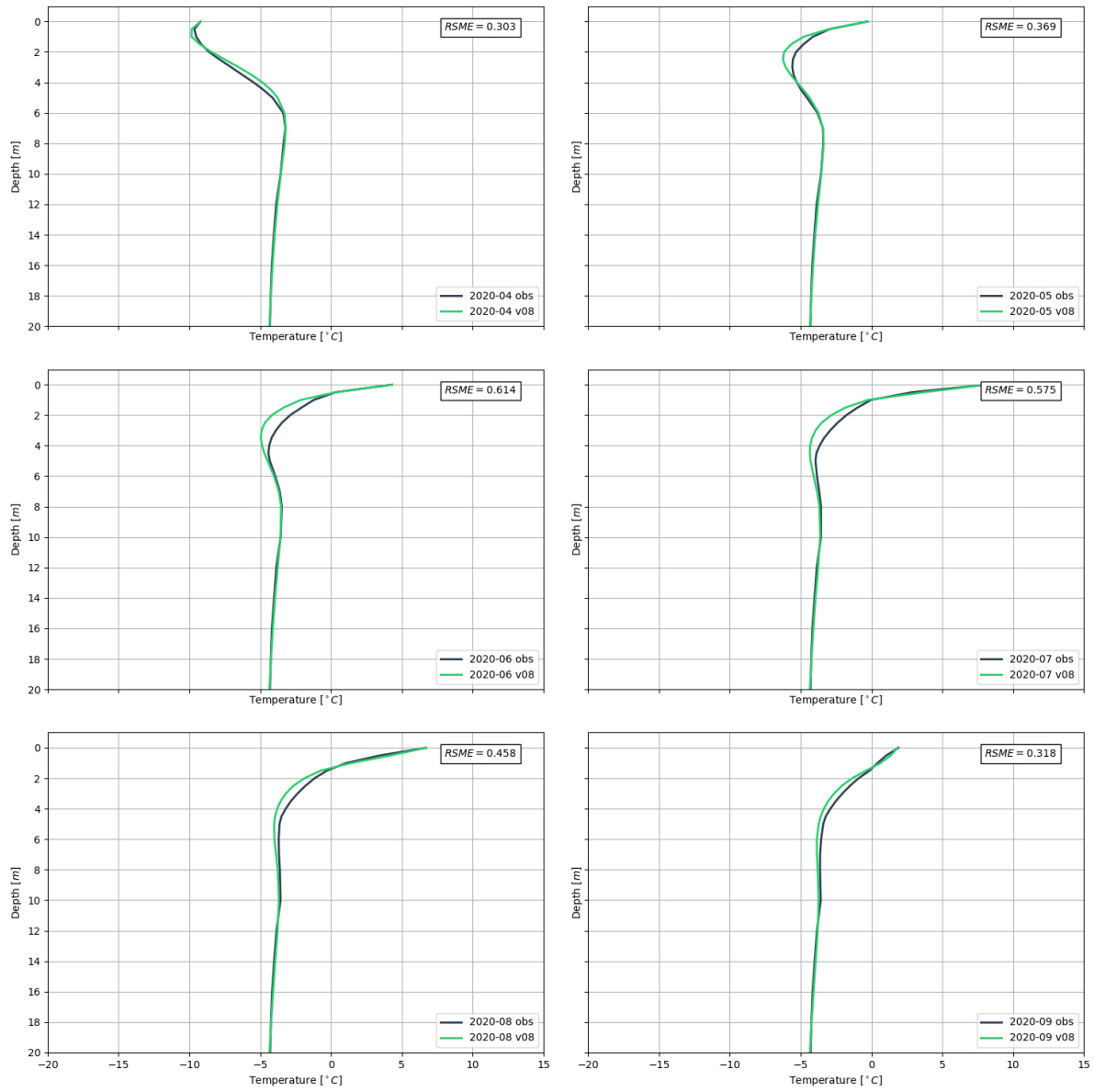

Figure 5.4: Comparison of modelled temperature profile (green) to measured temperature profile (grey) for the first of each month for calibration analysis v08 (Mar 2020 - Oct 2020).

The soil parameter set for analysis v08 is adopted for further modelling, the thermal properties are summarized in Table 5.3 and the input functions for the soil thermal conductivity and normalized unfrozen water content are presented in Figure 5.5a and Figure 5.5b. The unfrozen and frozen heat capacity is estimated using Equation 2.7 and 2.8, where the unfrozen water content is set to the estimated value at a temperature equal to -4.3 °C. The soil is assumed to be fully saturated, thus the in-situ volumetric water content is set equal to porosity.

Table 5.3: Set of soil properties for parameter set v08 resulting in the most accurate model results.

Unfrozen heat capacity [kJ/(m³.°C)]	Frozen heat capacity [kJ/(m³.°C)]	In-situ volumetric water content [-]	Thermal conductivity [(kJ/sec)/(m.°C)]	Unfrozen volumetric water content [-]
2 415	1 620	0.23	see Figure 5.5b	see Figure 5.5a

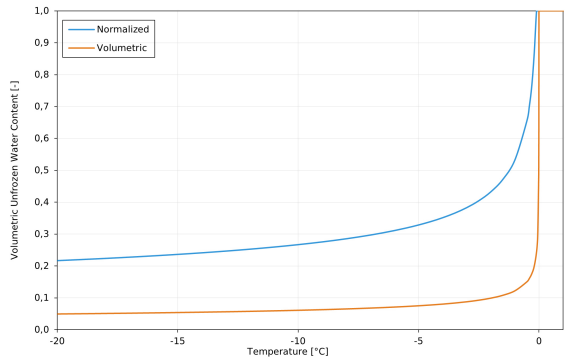

(a) Normalized and volumetric unfrozen water content versus temperature for soil parameter set v08.

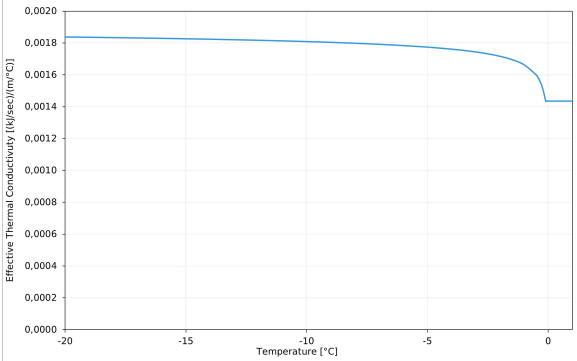

(b) Effective thermal conductivity versus temperature for soil parameter set v08.

Figure 5.5: Thermal input functions for effective conductivity and unfrozen water content for parameter set v08.

5.2 2D Model: Geometry, Forcing Data and Initial Condition

The 2-dimensional model is created to define the boundary extends for the cross-section, define suitable conditions to establish an initial condition and to test the sensitivity of the upper boundary condition. This is done in a 2-dimensional domain to save computational cost in greatly time-consuming iterative processes where an added dimension is not necessary.

A suitable model geometry is crucial to obtain reasonable results. Four main considerations were taken into account for the choice of geometry and boundary conditions in this study:

- the topography should be simplified,
- the influence of the ocean should be included in the model,
- the foundation system should be reasonably simplified, and
- the location of the thermistor strings need to be included.

The cross-section is chosen from west to south crossing through the cooling plate, thermistor location H2 and H1 as well as the coastline. The topography is derived from a cross-

sectional profile in QGIS using a digital elevation model (DEM) published by the Norwegian Polar Institute (Faste and Moholdt, 2021). The area of interest shows negligible elevation changes and gentle slopes. Therefore, the model domain is simplified by a horizontal ground surface until the coastline. Influence from slope shading or similar is thus not simulated. The bathymetry is extracted from the Norwegian Mapping Authority Kartverket (nd) and simplified for the model domain. The topography, the simplified model terrain and the extends of the model domain is shown in Figure 5.6. The final choice of geometry is strongly linked to the respective boundary conditions which is ultimately the result of a long iterative process. This is elaborated in more detail in the following sections before presenting the final geometry of the model domain. The 2D domain has 5 boundaries in total, a ground surface and a sea water, a left, a right and a lower boundary.

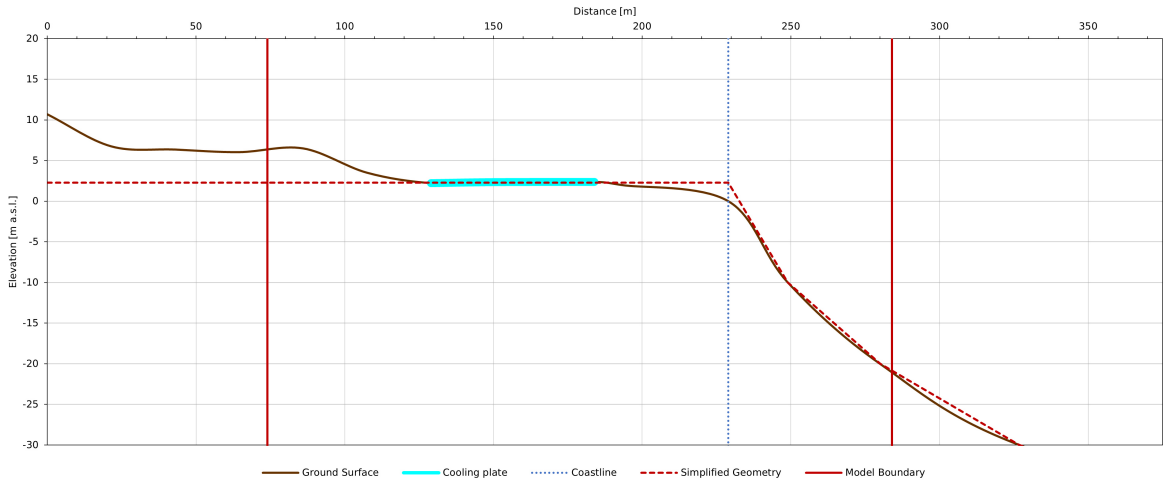

Figure 5.6: Illustration of the terrain and the simplified geometry for the model domain.

5.2.1 Ground Surface Boundary

Two options are considered for the upper boundary condition. A surface energy balance (SEB), where annual functions of wind speed, evaporation, air temperature, solar radiation, albedo and snow depth must be defined. This option requires a lot of site specific data. Since there is no information about snow depth, albedo and solar radiation for the location, numerous uncertainties are introduced by a SEB.

The second option is the application of a ground surface temperature function. Recorded air temperature from Svalbard Airport is available and can be modified with seasonal n-factors, discussed in more detail in subsection 2.2.1, to model ground surface temperature at the project location. This option introduces uncertainties in regards to the variable n-factors, which can change inter annual.

Both options considered, the ground surface temperature function is adopted as upper boundary condition since the available data for this option is more consistent and thus less uncertainties are introduced. The model should reproduce a good fit in view of mean monthly ground temperature measurements. Therefore the forcing data should also consist of mean monthly ground surface temperature data for the respective period of the analysis. This can be applied in form of a step function in TEMP/W.

5.2.2 Sea Water Boundary

The upper right sloping boundary represents the sea bed, sloping down from top of ground surface towards the sea as shown in Figure 5.6. To simulate the changes of sea temperature throughout the year, mean temperature values from a time series from 1987-2017 for winter and summer respectively are used. The values are extracted from Figure 5.7 adapted from Skogseth et al. (2020). The measurements were taken along a transect in Isfjorden close to Longyearbyen, and measurements from the upper 30 metres are used for this study. Station 34, indicated by the numbers on the x-axis in Figure 5.7, is located closest to the project location therefore temperature values from this area are chosen. The seasonal values are shown for winter, defined as January until May, and summer defined as July to September. In order to create a consistent time series throughout the year, winter and summer means are interpolated and applied for the missing months. The step function of mean monthly values, as presented in Figure 5.8, is cycled throughout the entire analysis period. The mean annual sea temperature of the chosen condition is approximately +1.0+,°C.

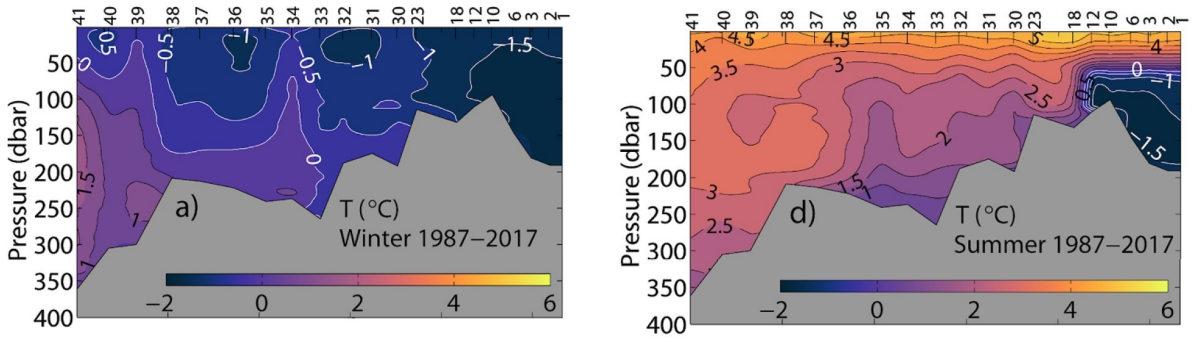

(a) Winter.

(b) Summer.

Figure 5.7: Mean annual temperature variation for summer (Jul-Sep) and winter (Jan-May) in Isfjorden for the time period 1987-2017 (Skogseth et al., 2020). The upper numbering represent different sampling locations along a transect in Isfjorden and number 34 is situated close to Longyearbyen.

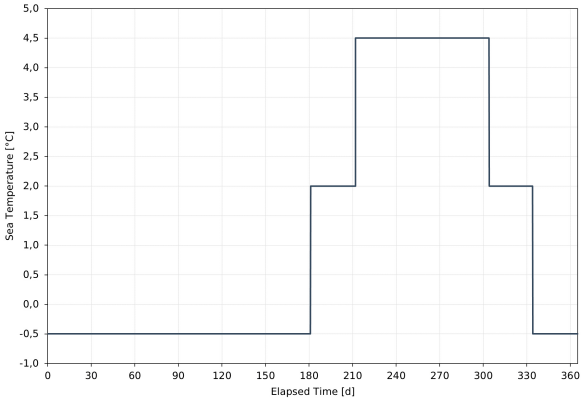

Figure 5.8: Adopted yearly sea temperature step function for the ocean bed boundary. Here depicted from Jan-Dec. The step function is adapted to the respective starting dates of an analysis.

5.2.3 Left and Right Boundary

The left or western and right or eastern vertical boundaries are closed, which means no heat can be added or removed through this boundary. Consequently no influence from the left side is considered. This is a simplification as terrain, roads, etc. can have an influence, but is neglected here in order to simplify the model and keep uncertainties to a minimum. The influence from the land side is not considered crucial here. The right vertical boundary results from constraining the extents of the model towards the sea side and is also set to closed.

5.2.4 Lower Boundary

The choice of the lower boundary condition was especially complicated by the existence of the ocean boundary. The lower boundary condition and extent must allow for a realistic temperature field creation. There are three options considered for the lower boundary condition:

- fixed temperature,
- closed (no heat is added or removed), and
- heat flux.

There is no solution that fully replicates the real situation. In combination with the lower boundary condition the depth of the model domain is important to define. Dependent on the extent of the model domain, different conditions can be applied.

The first option considered is to keep the model domain shallow, down to a depth of 20 metres for which measured temperature data is available, and apply a fixed temperature condition on the bottom. The drawback of a fixed temperature is that no temperature changes at

this boundary can be simulated, which can lead to inaccuracy in respect to transient modelling. Also, the MAGT at the lower boundary changes in respect to the x-coordinate or in other words in vicinity to the ocean. Consequently a fixed temperature is not suitable for this model.

The second option is a deeper model domain combined with a closed boundary condition. The depth of the model domain should approximately represent a depth in which the permafrost does not experience excessive warming from the bottom due to the geothermal gradient, but also allows enough space for a realistic temperature distribution in the upper layers, especially in view of the heat flux from the sea side. A closed boundary condition means that no heat can be added or removed at this boundary. This can be applied, if the model domain depth is chosen deep enough, so that upper layers, about down to 20 metres, are not affected by this boundary condition. Two temperature profiles from two boreholes in the area are analysed to support the decision-making and make a rough estimate of the deep thermal profile in the adjacent area. The location of the respective boreholes (TRT Measurements, Dh4-C02-07) relative to the environmental station is shown in Figure 5.9. First, temperature measurements conducted with a thermistor in a borehole located around 1 km away on Hotellneset are analysed and presented in Figure 5.10a. The data is provided by two NTNU master students, Marko Piitu Eemeli Kurttila and Kjersti Buraas Snoen, who conducted temperature measurements down to 200 metres. A borehole was drilled to perform thermal response tests (TRT) and, before the TRT test and after drilling, a thermistor was lowered into the borehole to record temperature every 5 metres. Thus, the data is not very accurate, but the trend in the borehole shows that the permafrost is not affected by the geothermal gradient to about 80 metres depth. Further results by Midttoemme et al. (2015) from a borehole located in Adventdalen, about 4 km east of Longyearbyen, are analysed. The temperature log from borehole Dh4 presented in Figure 5.10b shows that there is a negative heat flux present down to 110 metres, where it changes to a positive flux. Based on these observations, the domain depth should be extended to 80 metres to apply a closed boundary condition. However, after 30 meter depth bedrock is encountered at the project location, which needs to be considered in view of thermal response of the model in deeper layers.

The third option is to extend the model domain even further and apply a geothermal heat flux. This includes the warming effect on deeper layers and also indicates the bottom boundary of the permafrost.

Since the geothermal heat flow differs dependent on location and no information about the bedrock properties at the project location is available, it is decided that no heat flux is applied at the bottom boundary. This also keeps the domain shallower as a closed boundary can be applied at a depth of 80 meters. Furthermore, it is concluded that the entire model domain is modelled as a homogenous soil column of silty sand. This decision constraints the accuracy of the model to a depth of 30 meters and therefore does not account for the existence of bedrock. However, the focus of this study lies on the thermal regime around and under the plate and therefore only results down to 20 meters are relevant and will be analysed and processed. The extent of the model domain is only chosen to be able to create an appropriate initial temperature distribution, also factoring in the influence of the sea.

Figure 5.9: Location of the two respective boreholes, TRT Measurements and Dh4-CO2-07, in relation to the project site.

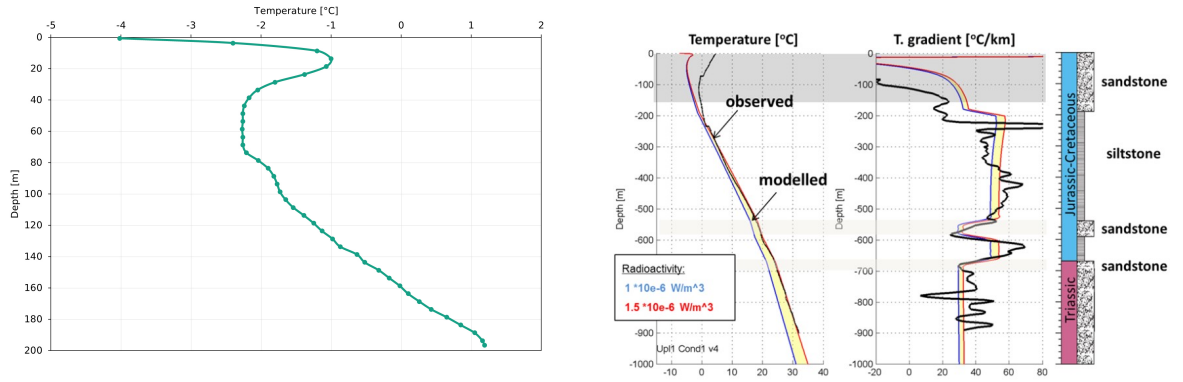

(a) TRT Project.

(b) Dh4-CO2-07.

Figure 5.10: (a) measurements for the TRT project show a warming effect in about 80 metres depth; (b) a negative heat flux is present until approximately 110 meter depth, a warming effect is observed below 120 metres (Midttoemme et al., 2015).

5.2.5 Model Geometry

The extents of the model domain are shown in Figure 5.6. The depth of the domain is set to 80 meters according to the reasons discussed beforehand in subsection 5.2.4. The right boundary was chosen to extend further from the plate than the left boundary to incorporate the effects of the adjacent ocean to the right. The distance between the left edge of the plate and the left boundary of the model is 55 meters. The right boundary extent was chosen to be two times the length of the plate. The total length of the domain in x-direction is 220 meters. The geometry should not constrain the area of interest and thus the outcome of the simulation.

The domain is divided into 3 regions to allow regional adjustment the discretization. The focus lies on the thermal regime down to 20 metres, hence a coarser mesh can be assigned to deeper layers to reduce the computational cost of the model. The first upper region extends to 1.5 meter below ground surface and is created with the surface layer option in TEMP/W. The depth is chosen according to the active layer thickness. The second region extends to a depth of 22.5 meters and the element length is 1 meter. The resolution of temperature distribution in the lower region does not need to be high, thus an element length of 20 meters is chosen. The mesh pattern is quads and triangles. The surface layer is meshed automatically with quadrilateral elements. The geometry and mesh for the 2D domain is shown in Figure 5.11.

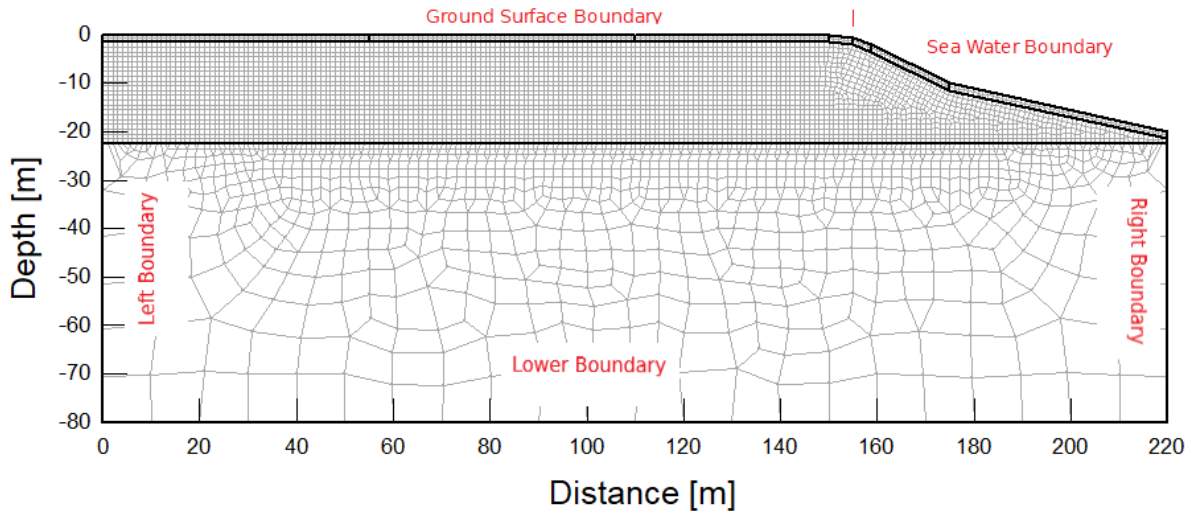

Figure 5.11: 2-dimensional geometry of the modelled cross-section; a finer mesh in the upper layer avoids numerical issues related to complex simulation of phase change.

5.2.6 Establishment of an Initial Condition

The initial condition, at which a simulation is started, influences the results greatly. Especially if simulations are not run over a long time until equilibrium or a steady-state condition is obtained, the results can very greatly, if the initial condition is not defined suitably. Here, an initial condition for the undisturbed terrain for October 2019 is established, to run an analysis from the start of October 2019 for an entire year, to test the model's performance on the basis of measured temperature data.

The model was tuned in order to reproduce a temperature profile as measured in the field. The conditions which ultimately result in the best fit for the initial condition in the 2D domain are subsequently applied for the 3D domain.

First, a steady-state analysis is run with a constant ground surface and sea water temperature to produce a temperature field for the entire model domain. Based on the steady-state analysis a transient analysis is run forcing monthly ground surface and sea water temperature fluctuations to achieve seasonal variation and warm the upper soil layers. The temperature for the upper boundary condition for the steady-state analysis is varied in combination with the subsequent warming period to find a combination that results in the best fit. The results are only presented for the best fit combination.

Steady-State

The sea water boundary is set to the mean annual sea temperature of +1 °C and a closed condition is prescribed to all remaining boundaries. The upper boundary temperature for the best fit is -4.55 °C. The resulting temperature field in the domain is displayed in Figure 5.12.

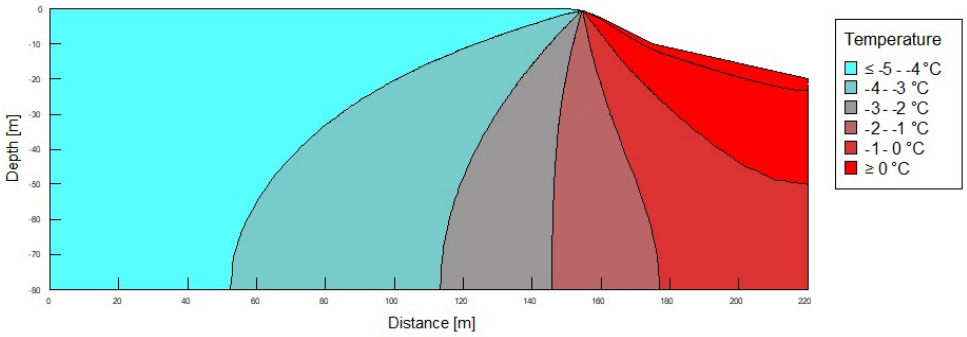

Figure 5.12: Temperature field in the 2D domain after running a steady-state simulation.

Transient Analysis

A transient analysis is run to warm the ground and introduce seasonal fluctuations. The analysis is started on 01 January and run for 6 years, saving the temperature profile for 01 October in each year. The boundary conditions are cycled throughout the entire analysis and results are compared to measured temperature to choose the best fit. The aforementioned soil properties from parameter set v08 are adopted.

Daily recorded air temperature from Svalbard Airport from 2014 to 2019 are used to create an average dataset for one year. The past 5 years are chosen, since the thermal regime in the ground, especially in deeper layers, is a result from several years of climatic fluctuation. The air temperature is modified with the respective seasonal n-factors presented in subsection 2.2.1 and assigned in form of a step function. The sea boundary condition in the transient analysis is set to the step function discussed in subsection 5.2.2. Time stepping is set to 27 days since the forcing data consists of monthly values.

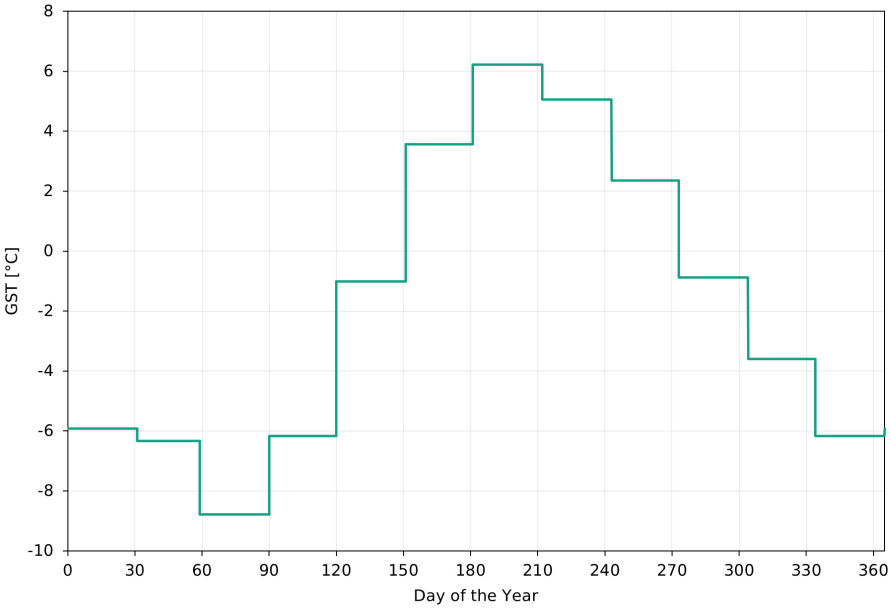

Figure 5.13: Step function applied as upper ground surface boundary condition consisting of an average ground surface temperature dataset from 2014-2019.

The temperature profiles from the transient analysis for 01 October for each year for borehole H1 and H2 are compared. The RMSE is calculated for each case and the conditions giving the smallest average RMSE are adopted for the initial condition. After a warming period of 6 years, equals 2099 days, the initial temperature profile in the ground generates an average RMSE of 0.19 °C and is adopted for further modelling. The RMSE in H2 is smallest after 5 years and starts to increase subsequently, in H1 the smallest RMSE is achieved after 6 years of warming. The temperature distribution on 01 October 2019 for H1 and H2 respectively is shown in Figure 5.14.

In both cases the modelled temperature on the bottom is slightly warmer than measured. Both profiles follow the same trend as the measured profile. H2 shows a good fit at top in the upper 1.5 metres. H1 is slightly too warm from ground surface until about 1.5 metres where it becomes slightly colder than measured. Overall, it shows a good fit with measured data and consequently the results are accepted for the initial condition and presented for the entire model domain in Figure 5.15.

Also, warming from the sea side can be observed and temperature profiles are well reproduced in both cases, therefore the geometry extent is chosen to be a good fit. A sensitivity analysis of the influence of the boundary extents can be conducted in these cases, here it would aid to minimize the extents of the model domain. However, since measured temperatures around the foundation area are reproduced well by the model, the sensitivity analysis

is not carried out in depth in this study.

Table 5.4: Initial condition chosen for further modelling shows 0.19 C error between modelled and recorded temperature.

Elapsed Time [days]	RMSE H2 [°C]	RMSE H1 [°C]	RMSE AVG [°C]
638	0,47	0,53	0,50
1004	0,34	0,39	0,36
1369	0,23	0,27	0,25
1734	0,20	0,20	0,20
2099	0,22	0,17	0,19

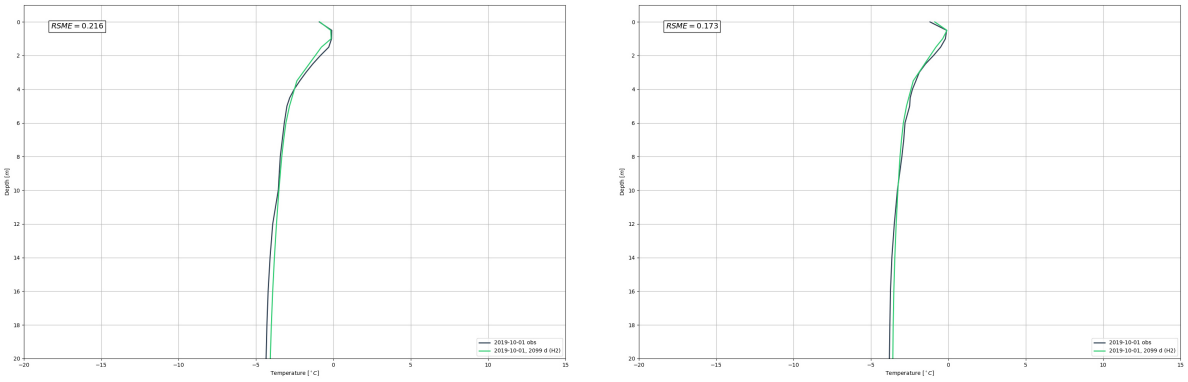

(a) Comparison of the modelled and measured thermal profile for 01 October 2019 in H2.

(b) Comparison of the modelled and measured thermal profile for 01 October 2019 in H1.

Figure 5.14: Initial condition for the simulation compared to recorded temperature profiles in H2 and H1 respectively; the average root means squared error is 0.19 °C.

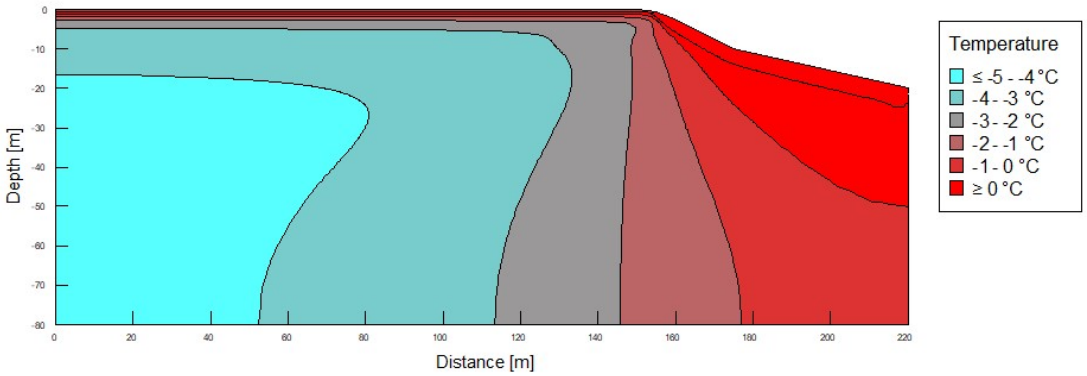

Figure 5.15: Temperature distribution in the initial condition for 01 October 2019.

5.2.7 Sensitivity of the Upper Boundary Condition

Since n-factors are estimated and not measured in the field, they introduce an uncertainty to the model. Also, Instanes (2016) suggests that a n-factor of 1.0 is a reasonable approximation in Longyearbyen. Furthermore, as mentioned previously, a thawing n-factor < 1.0 was

unexpected for this location. In order to quantify the effect of n-factors, a 2D analysis is run and the upper boundary condition is varied. Results are compared to estimate the impact or/and accuracy of the seasonal n-factors for this study. To reduce the computational cost, the analysis was done on the W-E cross section rather than the entire 3D model. Geometry, soil properties and all other boundary conditions are adopted as aforementioned. The analysis is run from October 2019 to October 2020 in order to compare a full year modelled and recorded temperature. The time stepping is set 27 days and the forcing data consists of monthly mean air temperature from Svalbard Airport, modified for two scenarios.

Three different conditions are adopted for the upper boundary and applied as a step function:

- mean monthly air temperature (AT),
- mean monthly air temperature modified with n_f=0.859 and n_t=0.803 (GST), and
- mean monthly air temperature modified with n_f=0.859 and n_t=1.0 (GST).

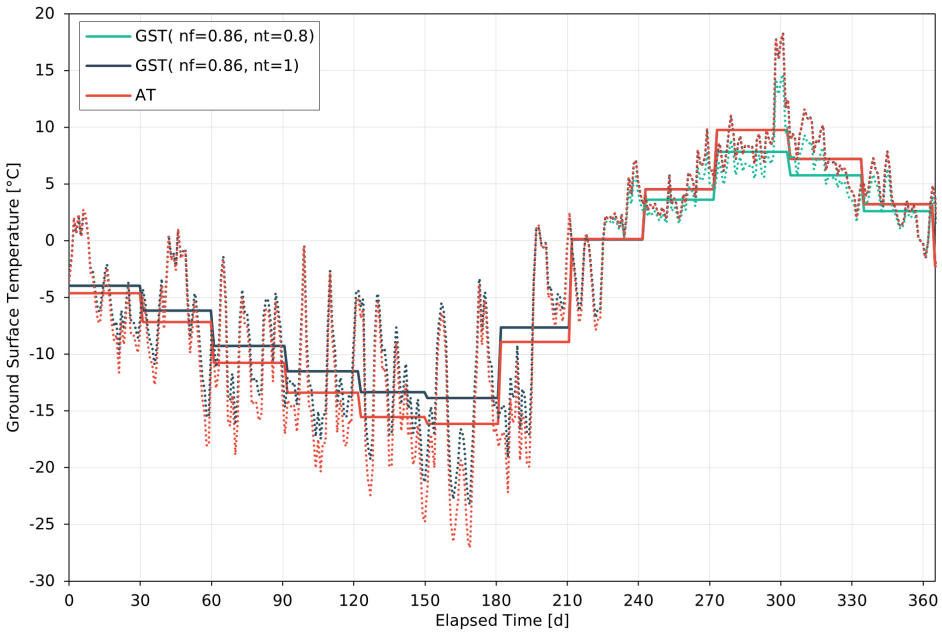

Figure 5.16: Step functions for the upper boundary condition forcing air and ground surface temperature for the three different scenarios.

Results are analysed by compiling mean monthly ground temperature profiles. The temperature profiles are shown in Figure 5.17 in form of yearly temperature trumpets. The results are compared in view of active layer thickness, DZAA, MAGT and the overall fit of the temperature profile by estimating the total RMSE. The results are summarized in Table 5.5.

Forcing air temperature leads to a good approximation of the active layer thickness, an overestimation of the DZAA and a generally colder MAGT. The total RMSE equals 1.11 °C. When observing the temperature trumpet, it is visible that modelled ground surface temperatures are warmer in summer and colder in winter. The temperature at 20 metres depth is slightly warmer. The profiles of each month follow the same trend, but show differences of up to +/- 1 °C. The second analysis, forcing modified air temperature with estimated n-factors, underestimates the active layer thickness by 15 cm and overestimates the DZAA. The MAGT is approximated reasonably well with a difference of 0.35 °C. The total RMSE for the entire dataset is 0.79 °C. The surface temperatures show a good correlation, where modelled temperature is slightly warmer in winter and colder in summer. The third analysis results in a good approximation of the active layer and an overestimation of the DZAA. The MAGT is approximated well and the total RMSE is 0.81 °C. The surface temperatures are slightly warmer in winter and summer.

Table 5.5: Comparison of measured and modelled ALT, DZAA, MAGT and MMGT at location H2.

Analysis [-]	ALT [m]	RMSE [m]	DZAA [m]	RMSE [m]	MAGT [°C]	RMSE [°C]	MMGT RMSE [°C]
Measurements H2	1.47	-	9.66	-	-3.48	-	-
Air Temperature	1.50	0.03	11.94	2.28	-4.08	0.60	0.85
GST (n_f=0.859 and n_t=0.803)	1.32	0.15	11.47	1.81	-3.83	0.35	0.51
GST (n_f=0.859 and n_t=1.0)	1.55	0.08	11.47	1.81	-3.76	0.28	0.54

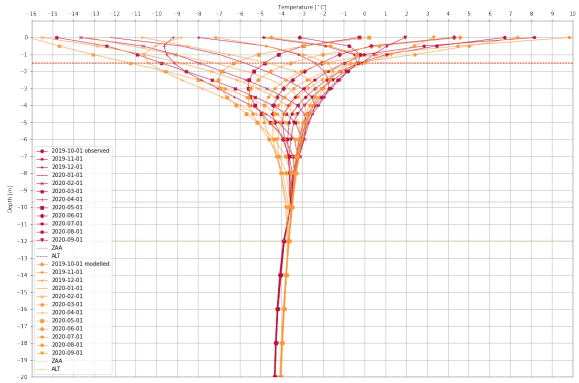

(a) Forcing data: Mean monthly air temperature (AT).

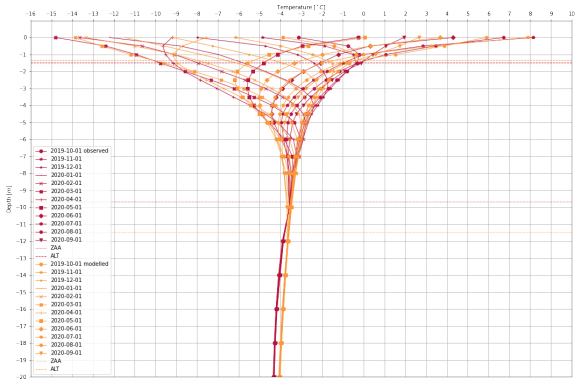

(b) Forcing data: Mean monthly air temperature modified with n_f=0.859 and n_t=0.803 (GST).

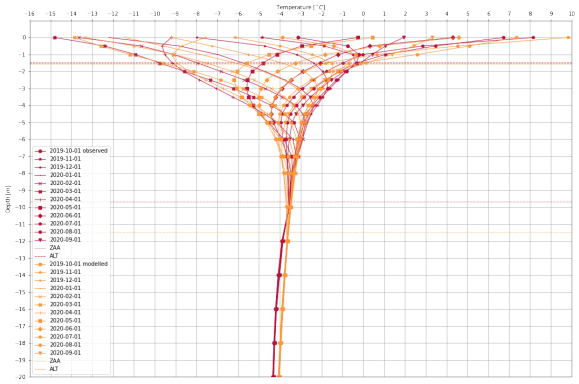

(c) Forcing data: Mean monthly air temperature modified with n_f=0.859 and n_t=1.0 (GST).

Figure 5.17: Comparison of modelled (orange) and measured (red) annual temperature trumpets for location H2.

Summary

For modelling the immediate future, air temperature with a modified thawing n-factor of 1.0 and a freezing n-factor of 0.86 is adopted, since it reproduces the best fit in terms of the active layer and the MAGT. However, mean monthly surface temperatures differ as much as 1.3 °C in January 2020. However, for simulations of future scenarios for the next decades, no n-factor is applied as n-factors are highly dependent on surface conditions which are expected to changed in the light of climate change.

5.3 3D Model

The 3D model is generated from the 2-dimensional cross-section. The geometry is extruded in z-direction, the added dimension for the 3D domain, by 90 metres. The geometry boundary is chosen to avoid the influence of boundary constraints in the region of the foundation and to show the influence of the cooling plate in regards to its surroundings. The dimensions

could possibly be optimized by running iterative simulations and comparing the temperature profile close to the plate, but this was not done for this study. The boundary is placed far enough from the plate, so that a steady temperature regime can be observed over a a sufficient length in z-direction from the plate to the edge of the model domain. The domain includes half of the footing's footprint to minimize the computational cost and the symmetry axis runs across the middle of the plate from west to east.

The major change in view of the 2D domain is the incorporation of the foundation system. The real foundation system is complex with various input parameters and additional physical processes such as convective heat transfer. The foundation system is designed with four different layers as follows: a 15 cm thick gravel fill layer, a 5 cm thick concrete layer with freezing pipes and 30 cm thick XPS insulation. The flank areas are also insulated with 30 cm of XPS insulation. During the construction process the design was altered to meet the encountered conditions. The final depth of excavation is 1 meter and a gravel fill layer was placed to level the terrain and thus varies in thickness dependent on the location. The gravel layer is supposed to be frozen at all times and is placed after excavation and dewatering of the site. The dimensions of the layers are adapted from the construction drawings and from meetings with the project manager, where changes to the original construction drawings were discussed. Here, the focus of the simulation lies on the thermal response in the ground to the foundation's cooling temperature. The foundation and pipe layout is designed to homogeneously cool the ground and keep the gravel layer under the cooling pipes constantly frozen (Grande, L. O., personal correspondence, 26 February 2021). Assuming that the design of the foundation achieves this, the entire freezing pipe system can be described as a surface with a temperature equal to the cooling temperature.

This simplification allows to model the foundation system by inscribing a one meter deep, 55 meter wide and 60 meter long cut into the topography equal to the outer dimensions of the foundation in reality. The concrete layer and cooling pipes are not incorporated. Rather a 70 cm thick gravel layer is placed on the bottom of the cut, followed by 30 cm of XPS insulation. Also, 30 cm thick XPS insulation is placed along the four vertical faces of the cut. The cooling temperature can be applied to the upper face of the gravel fill body simulating the cooling effect between the gravel layer and the insulation. The gravel layer is assumed to be fully drained and simulated with the simplified thermal model to lower the computational cost and temperatures in the gravel layer should always lie below the freezing point. The thermal conductivity is adopted from VDI (2019) recommending a thermal conductivity for

dry gravel between 0.4 to 0.9 W/(m·K) in the guidelines for *Thermal use of the underground - Ground source heat pump systems*. If the thermal conductivity is underestimated, the simulated layer acts as a better insulator; if it is overestimated, heat is conducted better than in reality. The choice of a low thermal conductivity therefore leads to an conservative approach in terms of freeze in time of the soil, however it is favourable in terms of power failure where the layer can act as an from the heat flowing from the heated building above.

The thermal properties are summarized in Table 5.6. The XPS insulation is simulated with the simplified thermal model in TEMP/W with a heat capacity and water content of zero and a constant thermal conductivity of 0.036 W/(m.°C) or 0.000036 kJ/sec. The thermal conductivity is adopted from the BEWI XPS Insulation data sheet available online (BEWI, nd). The activation temperature is set to 0 °C. Both materials are activated with a temperature of 0 °C, since it was constructed in December when ambient temperature is below freezing.

Table 5.6: Input parameters for foundation layers in the simulation.

Material [m]	Height [m]	Therm. conductivity (frozen & unfrozen) [W/(m.°C)]	Vol. Heat Capacity [MJ/(m³.°C)]	Act. Temp. [°C]
Gravel, drained	0.7	0.5	1.5	0
XPS insulation	0.3	0.036	0	0

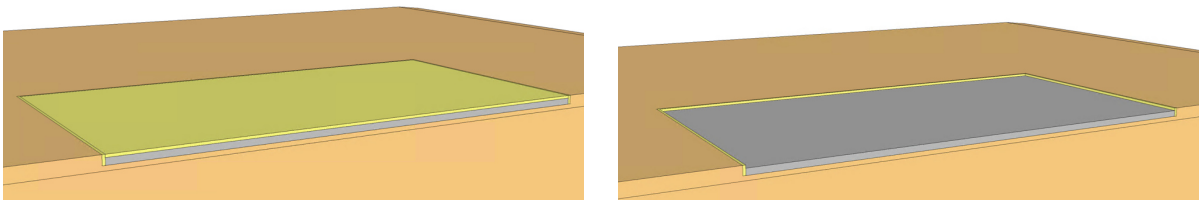

(a) Insulation in yellow, gravel in grey and the and soil in brown.

(b) The cooling temperature is applied on the upper gravel face visible here, which lies under the insulation.

Figure 5.18: Illustration of the simplified foundation system for the simulation.

The 3D geometry consists of 5 solid bodies (or regions). The regions are meshed with hexahedral elements. The surface layer is split at the coast line to enable a finer discretization in vicinity to the plate. The upper land layer, the plate and the insulation are meshed with an element size of 0.5 metres and the upper layer at the sea side with 1.5 metres. The region under the surface layers is meshed with elements of one meter length and the lowest regions with an element length of 40 metres. The size of the mesh effects the results and an iterative process was necessary to define a mesh size, which is large enough to achieve a reasonable computational time, but small enough to ensure a good approximation of real conditions. Especially in the upper layers, in light of phase change, a finer mesh is needed to accommo-

date these effects in the results. The geometry and mesh for the 3D model is depicted in a sketch in Figure 5.19 and a screenshot from TEMP/W 3D in Figure 5.20.

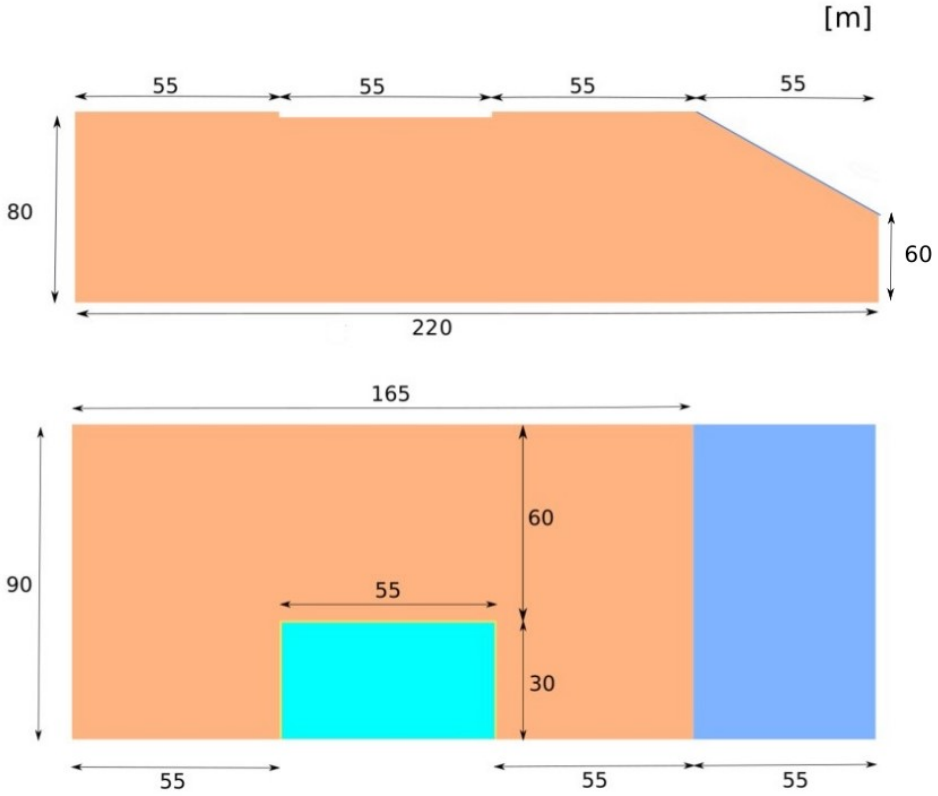

Figure 5.19: Conceptual sketch of 3D geometry and its dimensions, the upper sketch depicts a cross-section from west to east, the lower depiction is a bird view of the model domain with the sea in blue and the cooling plate in turquoise.

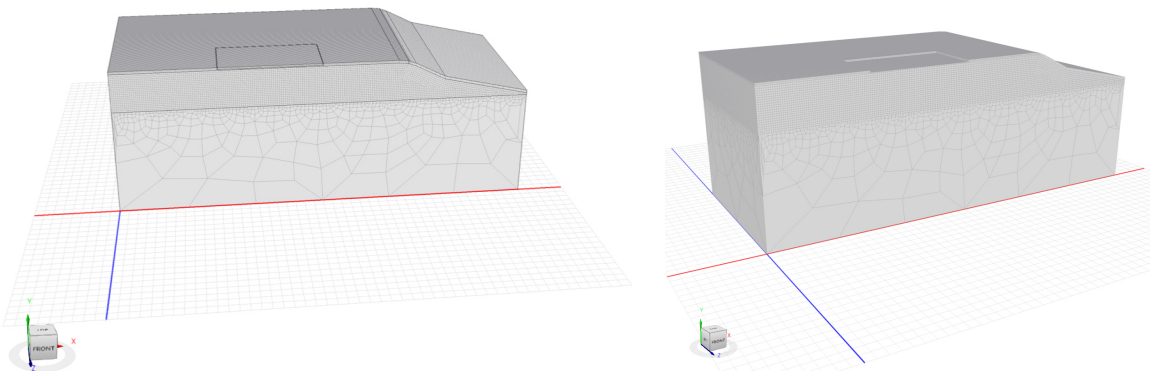

(a) 3D geometry before construction of the plate.

(b) 3D geometry after construction of the plate.

Figure 5.20: 3D geometry in TEMP/W with respective mesh in each region.

5.3.1 Model Performance

The model's ability to reproduce in-situ conditions is tested in the 3D domain before conducting numerical simulations of different scenarios. Reliable temperature measurements are only available for the time prior of the start of the cooling system, thus the testing is done by modelling the undisturbed terrain prior to 29 December 2020 when the cooling system was started.

The 3D simulation is run with soil properties, geometry and discretization as explained prior. The start date is 01 October 2019, and the simulation is run until December 2020. The thermal boundary condition for the sea boundary is applied in form of a step function as explained in subsection 5.2.2. A mean monthly ground surface temperature in form of a step function is applied as discussed in subsection 5.2.7. All other boundary condition are set to closed. The time stepping is set to 27 days. The initial condition is obtained for 01 October 2019, following the same procedure as discussed for the 2D domain in subsection 5.2.6. The result of the steady-state analysis and the final profile for 01 October 2019 are shown in Figure 5.21.

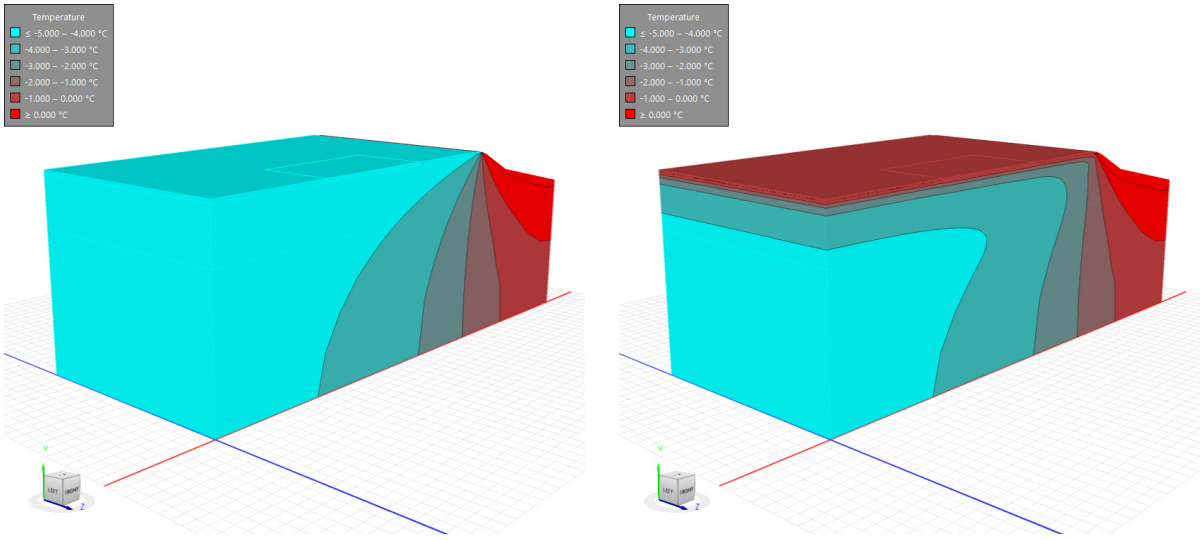

(a) Steady-state analysis.

(b) Transient analysis: Final profile for 01 October 2019.

Figure 5.21: Temperature field in the ground for the steady-state analysis and the subsequent warming in the transient analysis to establish the initial condition for 01 October 2019.

The results of the analysis in terms of ALT, DZAA and ground temperatures are summarized in Table 5.7 and illustrated in Figure 5.22. At H1 the permafrost temperature at 20 meter depth is overestimated by 0.2 °C whereas at H2 is underestimated by 0.3 °C.

The recorded and modelled mean monthly profiles for each location are compared and shown in Figure 5.23 to 5.28. Additionally, a comparison of results for the upper five metres

is made to quantify the accuracy in the shallow subsoil around the foundation system. The results are summarized in Table 5.8 and a detailed illustration of only the upper 5 metres is appended in section B.5. The plots give more insight whether the model over- or underestimates ground temperatures, which is valuable insight for interpretation of the model results.

The accuracy of the model in respect to monthly results differs between 0.2 °C in the best fit and 1.2 °C in the worst fit. The accuracy of the model differs for the same month of different years, for example in December 2019 the total RMSE is 0.9 °C in H2 whereas in December 2020 it is 0.5 °C. In the majority of cases, the model produces a colder regime than recorded in the field. However, no seasonal trend can be observed and based on the errors produced by the model, it is necessary to interpret the results with a ± 1 °C accuracy. For a conservative interpretation of the ground temperatures in regards to a minimum cooling temperature, the model results should be considered with an accuracy +1 °C.

Table 5.7: Quantification of the model accuracy in respect to ALT, DZAA and MAGT at -20 metres for the indicated duration at the respective location.

Location [-]	Duration [-]	ALT [m]	RMSE [m]	DZAA [m]	RMSE [m]	MMGT at -20 m [°C]	RMSE [°C]
H1	Oct 19 - Jul 20	-	-	11.57	1.76	-4.0	0.23
H2	Oct 19 - Dec 20	1.51	0.04	11.57	1.91	-4.0	0.30

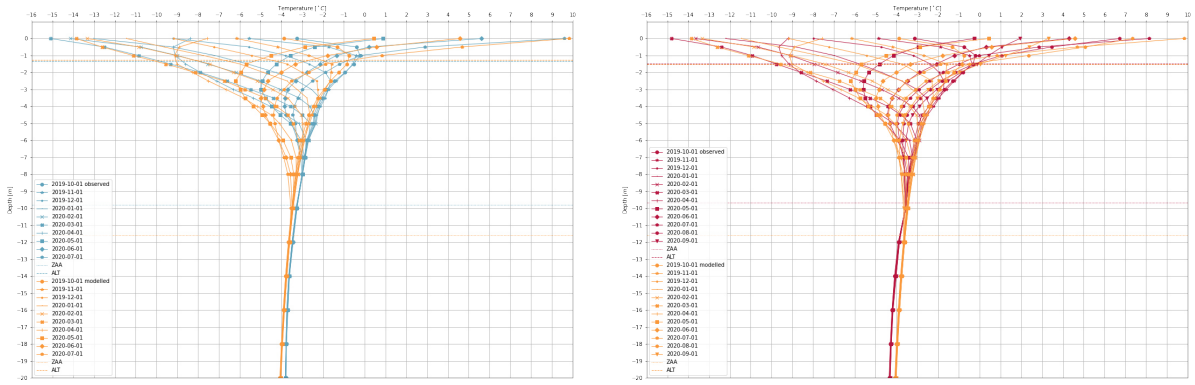

(a) Location H1.

(b) Location H2.

Figure 5.22: Mean monthly measured and modelled temperature profile for October 2019 until September 2020.

Table 5.8: Summary of produced RMSE for the total depth and for the upper 5 metres in respect to recorded mean monthly ground temperature for each location.

	H2		H1		H4	
Date [m-yy]	$RMSE_{total}$ [°C]	$RMSE_{5m}$ [°C]	$RMSE_{total}$ [°C]	$RMSE_{5m}$ [°C]	$RMSE_{total}$ [°C]	$RMSE_{5m}$ [°C]
Oct-19	0.4	0.4	0.4	0.4	-	-
Nov-19	0.9	1.2	0.8	1.1	-	-
Dec-19	0.9	1.2	0.7	0.9	-	-
Jan-20	0.4	0.4	0.5	0.7	-	-
Feb-20	0.3	0.3	0.4	0.5	-	-
Mar-20	0.4	0.4	0.5	0.6	-	-
Apr-20	0.5	0.6	0.5	0.5	-	-
May-20	0.4	0.5	0.8	1.0	-	-
Jun-20	0.6	0.8	0.8	1.1	-	-
Jul-20	0.8	1.1	0.8	1.0	-	-
Aug-20	0.6	0.8	-	-	-	-
Sep-20	0.5	0.7	-	-	-	-
Oct-20	0.3	0.3	-	-	-	-
Nov-20	0.2	0.2	-	-	0.5	0.6
Dec-20	0.5	0.7	-	-	0.8	1.1
Average	0.5	0.6	0.6	0.8	0.7	0.9

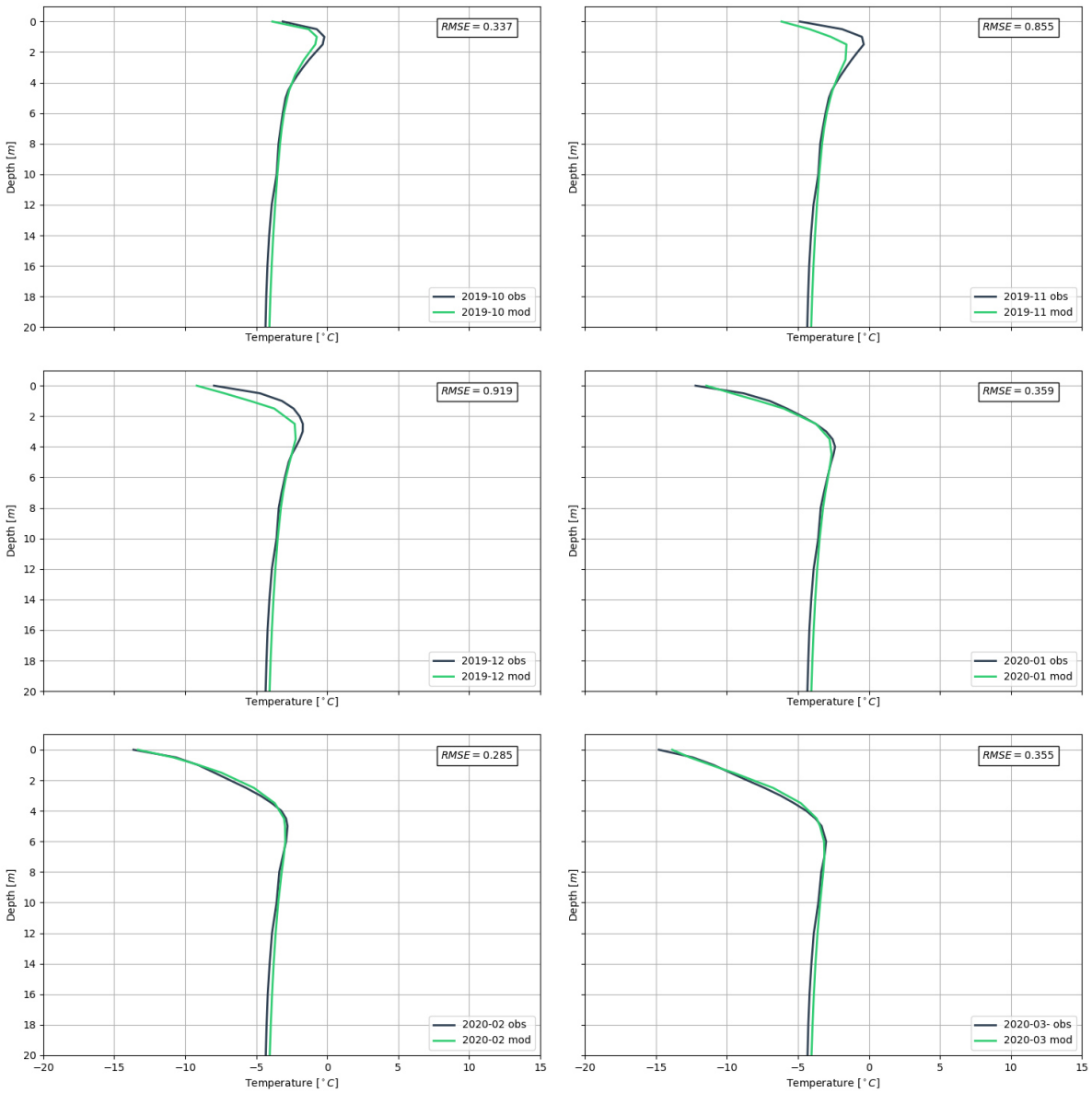

Figure 5.23: Comparison of modelled (green) and measured (black) mean monthly ground temperature profiles

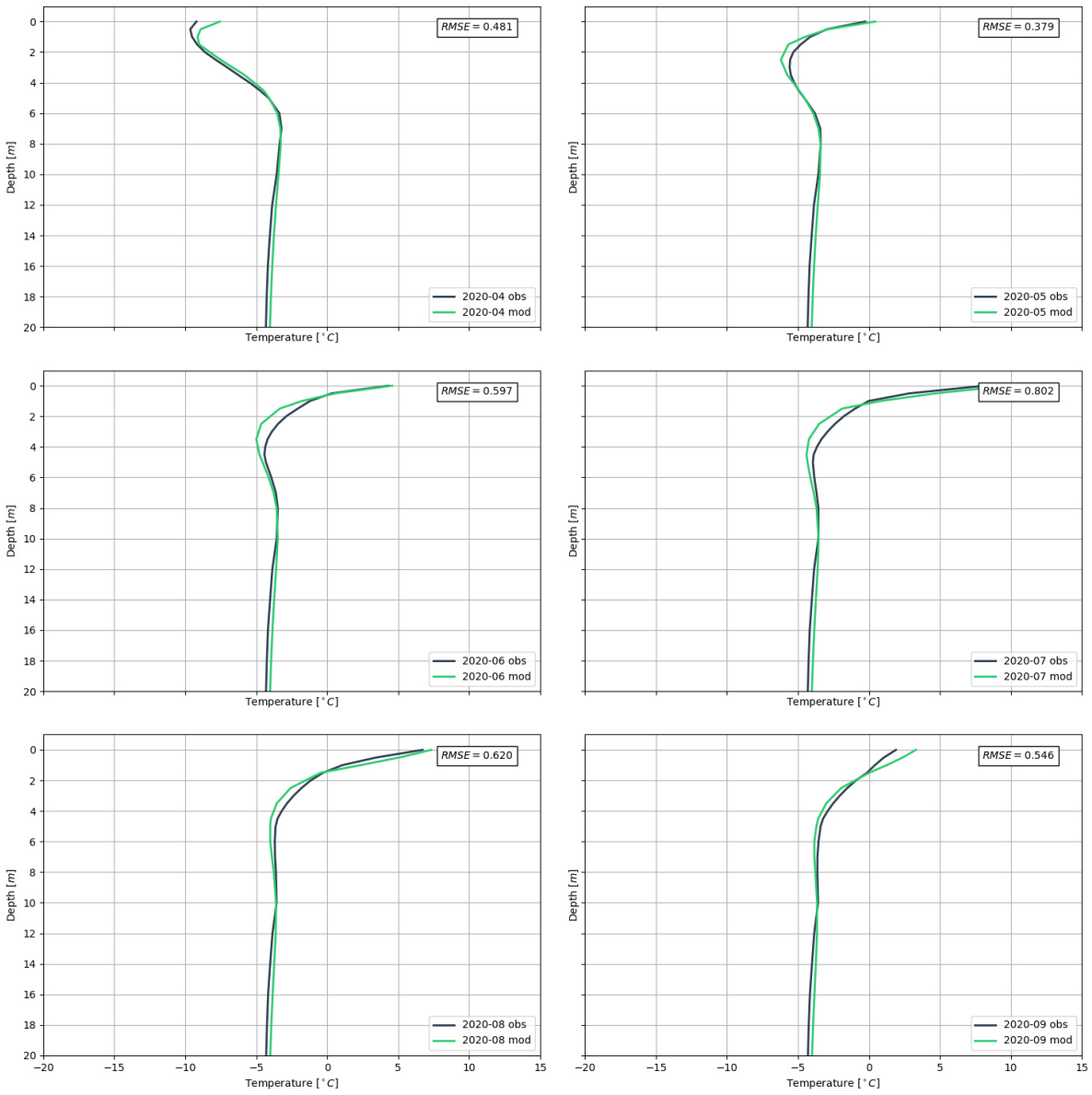

Figure 5.24: Comparison of modelled (green) and measured (black) mean monthly ground temperature profiles at H2 (Apr 20 - Sept 20).

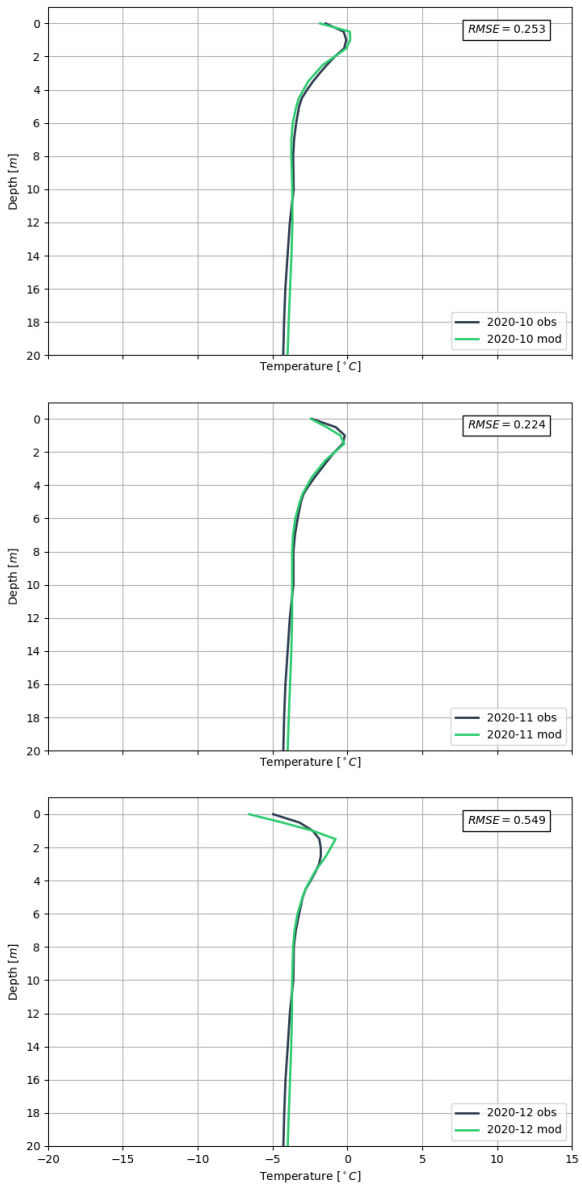

Figure 5.25: Comparison of modelled (green) and measured (black) mean monthly ground temperature profiles at H2 (Oct 20 - Dec 20).

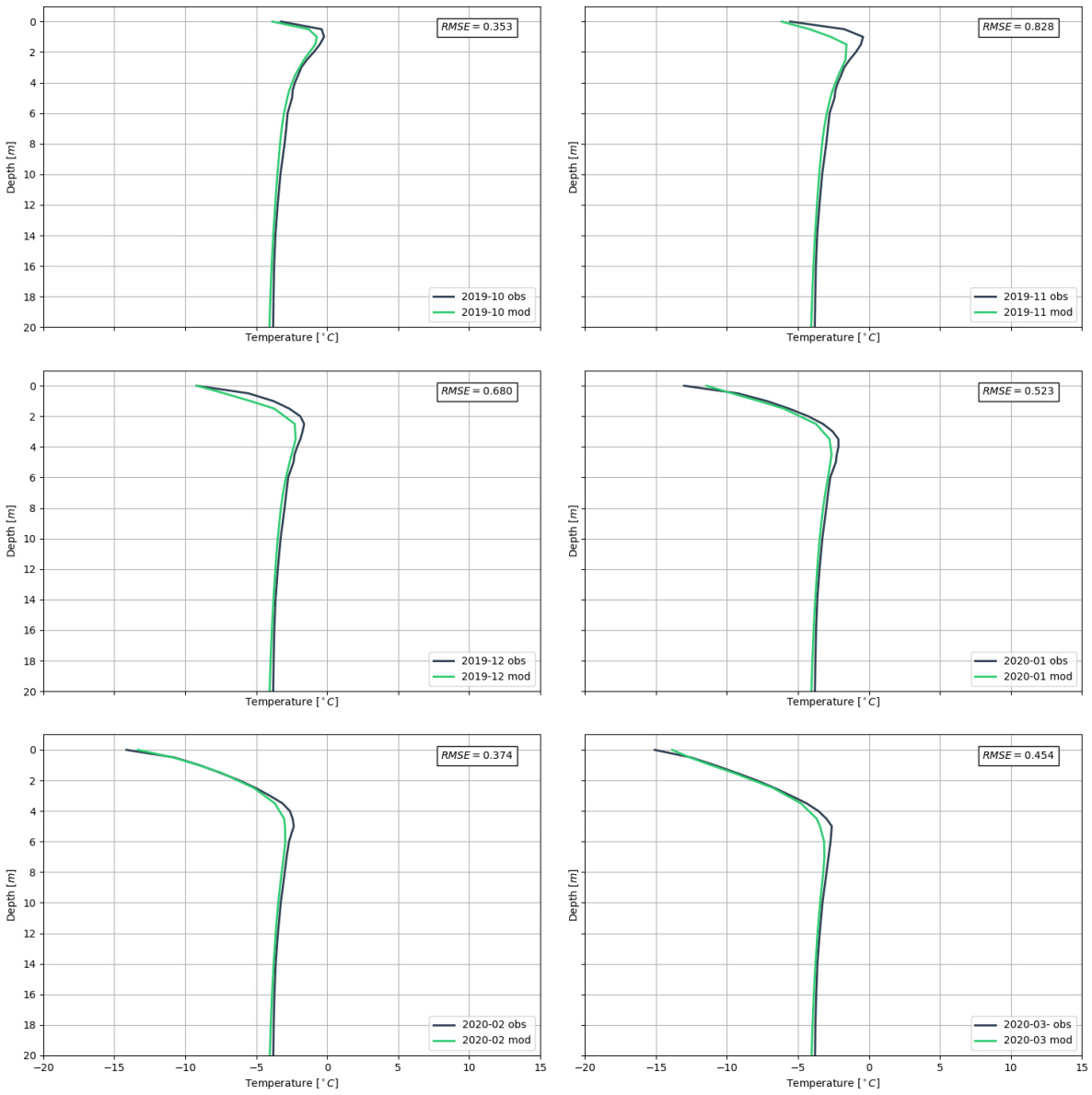

Figure 5.26: Comparison of modelled (green) and measured (black) mean monthly ground temperature profiles at H1 (Oct 19 - March 20).

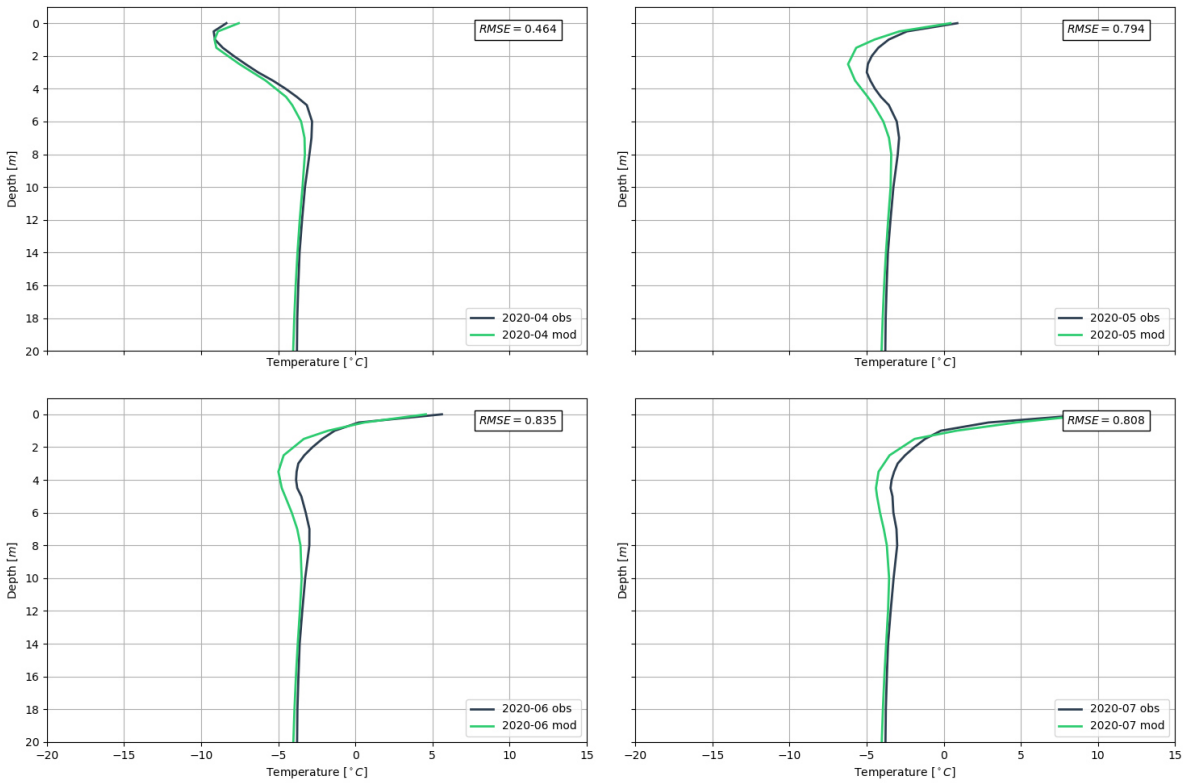

Figure 5.27: Comparison of modelled (green) and measured (black) mean monthly ground temperature profiles at H1 (Apr 20 - Sept 20).

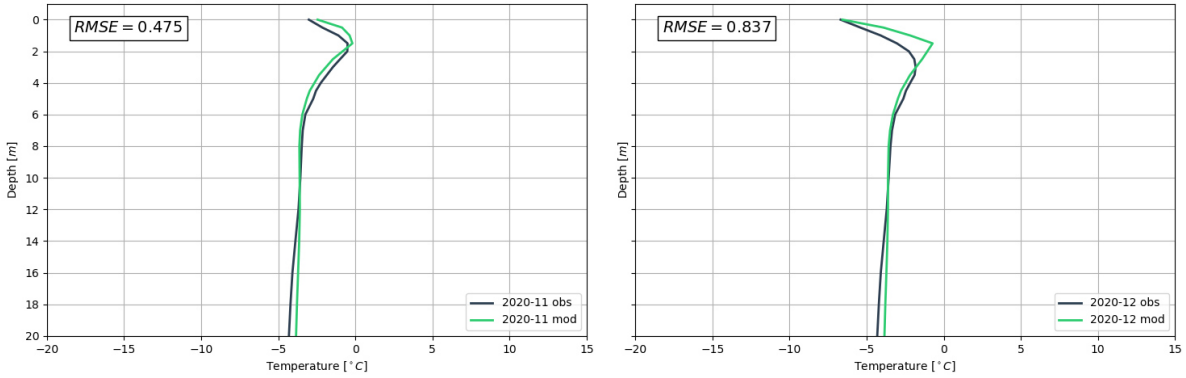

Figure 5.28: Comparison of modelled (green) and measured (black) mean monthly ground temperature profiles at H4 (Apr 20 - Sept 20).

5.4 Summary

The results of the calibration and validation process are summarized here:

- The soil is simulated as one homogenous soil column of silty sand to 80 meter depth. The soil properties of the silty sand are calibrated to measured data and the thermal profile shows good correlation with the measured data down to 20 meter depth. How-

ever, the thermal regime below 20 meter depth is unknown. This limits the model's reliability to a depth of 20 meters.

- The unfrozen thermal conductivity of the soil is 0.0014 (kJ/sec)/(m°C) or 1.4 W/(m°C). The frozen thermal conductivity is temperature dependent with up to 1.8 W/(m°C) at -20 °C.
- The unfrozen volumetric heat capacity of the soil is 2415 kJ/(m³/°C) and the frozen volumetric heat capacity is 1620 kJ/(m³/°C).
- The unfrozen volumetric water content for the soil shows that a part of the pore water remains unfrozen even at temperatures below -20 °C. The freezing point is assumed at 0 °C, thus no effects of salinity are included in this analysis.
- The average root mean squared error for the initial condition (01 October 2019) is 0.19 °C.
- The sea water temperature at the project location is not measured over a full cycle of seasons and the sea temperature for the model is adopted from a study in vicinity to the project site. However, the modelled thermal profile H1, close to the sea, shows good correlation to the measured profile and its warming effect on the cooling plate can therefore be assumed to be included in the model.
- Air temperature modified with seasonal n-factors result in a better fit than solely air temperature. The total RMSE decreases about 0.3 °C when applying n-factors.
- The model simulates mean monthly temperatures down to 20 metres with an annual root square mean error of 0.6 °C in H1 and 0.5 °C in H2.
- The active layer thickness is only compared for H2 where a full data set is available and shows a very good approximation with a negligibly small error of 0.04 m.
- The depth of zero annual amplitude is overestimated in the model by approximately 1.8 metres.
- Mean annual ground temperatures at 20 metres depth are modelled with a RMSE of 0.2 and 0.3 °C for H1 and H2 respectively.
- Model results should be interpreted with an accuracy of at least ±1 °C, which is especially of importance in areas of critical ground temperatures approaching the freezing point.

Chapter 6

Numerical Simulations of Relevant Scenarios

This chapter describes the simulations of four different scenarios based on the verified 3D model. The scenarios are relevant for this project in specific, but shall also give more understanding for the ground's thermal behaviour for future projects.

The design cooling temperature is set to - 5°C for this project. However, this temperature is based only on temperature measurements from string H2 and H4. This study should give more insight into the temperature distribution under the plate and give guidance in view of a suitable cooling temperature. For this purpose, the first scenarios deal with the thermal response of the ground for a cooling temperature of -5 and -10 °C respectively. Also, the heat rate and cumulative energy transfer is studied to give an estimate of operational cost and minimum heat pump capacity in both cases.

Further, for the design cooling temperature, a scenario with seasonal cooling is simulated to study the possibilities to optimize energy usage during operation. This scenario is of increasing interest in view of future projects and development of the system. Especially in view of the ongoing EU funded pilot project in Longyearbyen, which aims to couple heat pump cooling foundation with solar energy to run the system on green energy. As the dark season is not suitable to run the system on solar energy, the possibility to turn off the system in cold winter months, when the ground gets cooled naturally from the ambient air, is investigated here.

Also, since power failure has shown to be the most frequent cause for damages to structures built on heat-pump cooling systems, the thermal response of the ground is investigated when the cooling is turned off. This scenario should foremost show the necessity of cooling

and can give insight into the duration at which the ground remains frozen without cooling in an event of power failure.

The final scenario is a simulation for a projected climate warming for the 50 years service lifetime of the building. This is done to investigate the system's applicability in regards to whether the adjacent soil remains permanently frozen or not. The future operational cost for this scenario is compared to the cost nowadays to study its feasibility for its lifetime.

The general conditions, which are applied to all scenarios, are summarized first in this chapter, followed by sections for each scenarios, where scenario specific conditions are outlined in more detail. In general, the initial condition and the time stepping are not varied between the scenarios. The presentation of results can be found in each scenario. This chapter ends with a summary of limitations, which underlie the numerical simulations.

6.1 General

The time stepping for all analyses is 27 days to obtain monthly results and the datasets are created without leap years, thus each year is assumed to have 365 days for simplification. Table B.3 to B.8 give an overview of the date and respective elapsed time in the simulation. This states 01 October 2019 as day 2099, which is caused by the fact that time elapsed for the prior establishment of the initial condition for 01 October 2019.

For the purpose of studying the thermal regime under the plate, six reference points are defined on the bottom of the foundation area. A conceptual sketch of their respective positions is shown in Figure 6.1. Every reference point on the plate is placed along the inner edge of the insulation. The symmetry line runs across the lower horizontal edge in the sketch below, as only half of the footing is included in the model as explained prior.

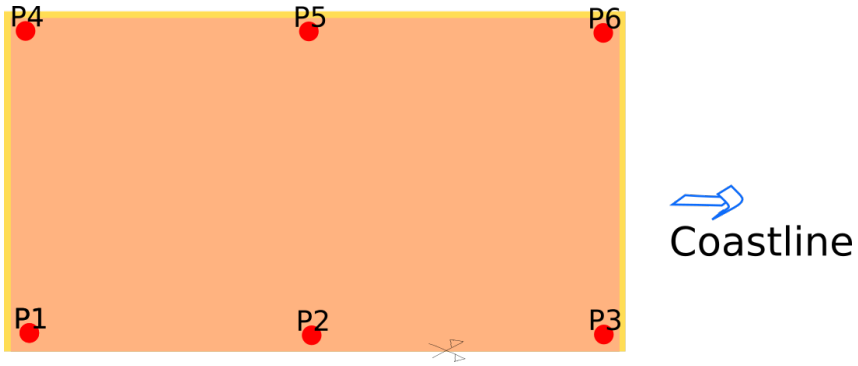

Figure 6.1: Conceptual sketch of the reference points relative to the foundation area.

For each scenario the convergence criteria was set to the values discussed in section 3.2.

The convergence criteria was met in all simulations presented in this chapter, resulting in zero unconverged temperature nodes and a maximum of 35 iteration steps.

6.1.1 Initial Condition

An initial condition must be established for end of December 2020 when the cooling system was started. In order to obtain an initial condition, a simulation is run from October 2019 until December 2020 for the natural terrain. For this purpose, the upper boundary condition is set to mean monthly ground surface temperature for the simulation period and mean monthly sea surface temperature as explained in subsection 5.2.2. Measured monthly air temperature is modified with n_t= 1.0 and n_f=0.86 as shown in Figure 6.2a. All other boundaries are closed. The resulting initial condition December 2020 for subsequent studies is shown in Figure 6.2b. The obtained initial for condition for December 2020 shows a RMSE of 0.7 °C in H2 and 0.4 °C in H4 compared to the measured mean monthly profile. The model produces a colder regime in the upper layer and a warmer regime in the deeper layers, below 10 metres, compared to measured data as shown in Figure 6.3.

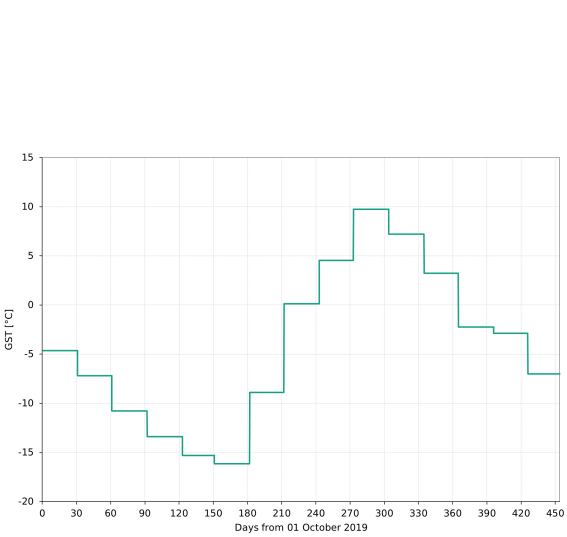

(a) Step function applied for monthly ground surface temperature from Oct 19 - Dec 20.

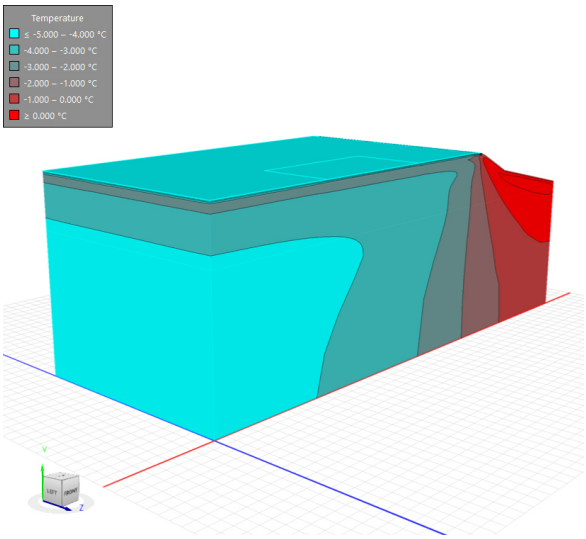

(b) Obtained initial Condition for December 2020, just before the cooling system is turned on.

Figure 6.2: Applied forcing data for the land surface (left) and generated initial thermal regime for the natural terrain in December 2020 (right).

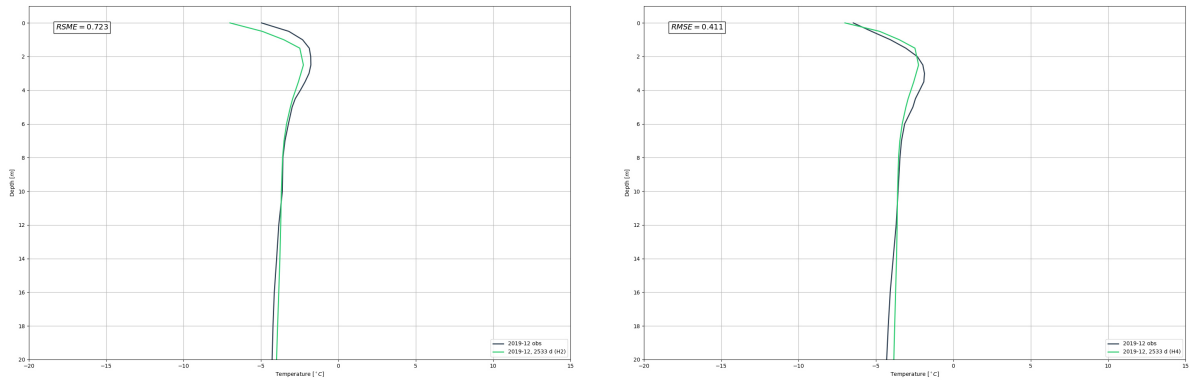

(a) H2. (b) H4.

Figure 6.3: Comparison of the temperature profile used as initial condition for the model in December 2020.

6.2 Behaviour of the Ground under a Cooling Plate

A transient analysis, to investigate the ground's thermal behaviour under the cooling plate for a duration of 10 years under unchanged climatic conditions, is conducted. The simulation is run for a cooling temperature (T_p) of -5 °C and -10 °C respectively, to compare the ground's thermal response. The heat rate and cumulative energy transfer at the cooling pipe surface are obtained to make a rough estimate for the heat pump's capacity and annual operational cost.

6.2.1 Definitions

The analysis starts in January 2021 with the aforementioned initial condition. The foundation system is incorporated in the model geometry as explained in section 5.3. The cooling temperature is applied on the upper gravel face. The ambient temperature in the building on top of the foundation is +15 °C, which is applied as an upper boundary condition to the foundation system on the upper insulation face for the entire simulation. An average mean monthly air temperature dataset is compiled from measured air temperature data for 2019 and 2020 respectively to smooth annual extremes. To relate the air temperature to the ground surface temperature, a freezing n-factor of 0.86 and a thawing n-factor of 1.0 is applied. The mean annual ground surface temperature is -2.7 °C. The mean monthly ground surface temperature is applied in form of a step function and cycled for 10 years as shown in Figure 6.4b. Again, the mean monthly sea surface temperature is applied as discussed in subsection 5.2.2 and also cycled throughout the entire simulation.

The simulation is run for 10 years and the forcing data during this time is cycled annually

to remove the influence of climatic changes in order to observe the ground's equilibrium state. This however does not represent real conditions as climate always changes but eases the interpretation of results and definition of governing factors in view of the design of the cooling system.

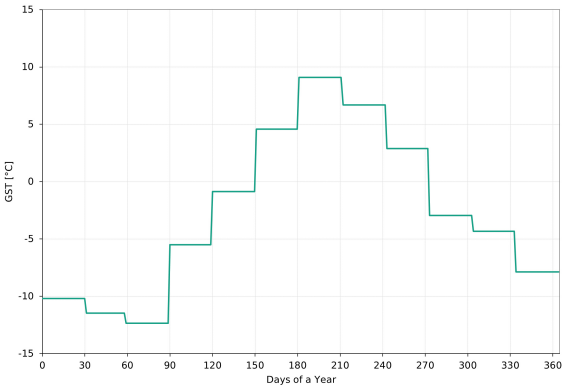

(a) Mean monthly ground surface temperature exemplary shown for one year.

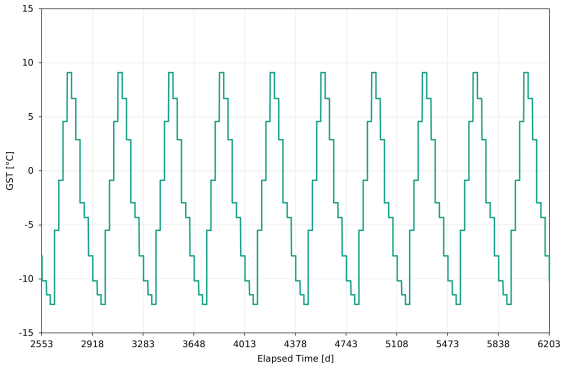

(b) Mean monthly ground surface temperature dataset for the entire analysis.

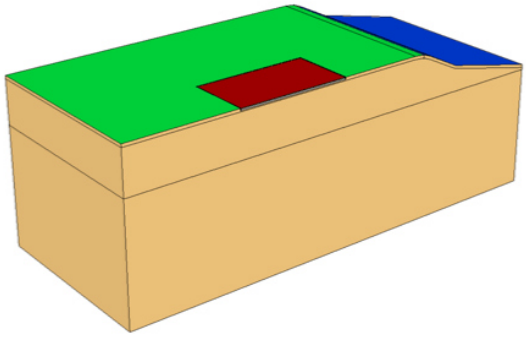

(c) Applied boundary conditions for the simulation distinguished by color: GST (green), sea temperature (blue), building inside temperature (dark red).

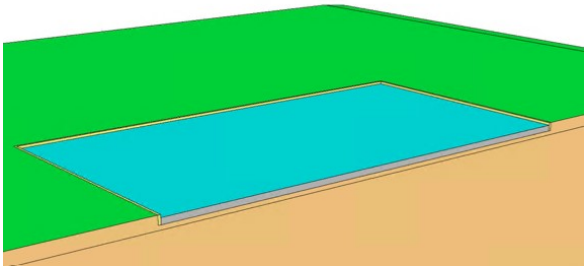

(d) Cooling temperature (turquoise) beneath the insulation on top of the gravel pad.

Figure 6.4: Definitions for the numerical simulation of the ground's behaviour under a cooling plate.

6.2.2 Results

Temperature Regime from a Cooling Temperature of -5 °C

Ground temperature versus time plots for selected depths for each reference point are presented in Figure 6.6. This is also evident in the temperature profile in P2, shown in Figure 6.7, where it is visible that the ground has already adjusted to the cooling temperature in year 3. The profile becomes more linear in year 10 but changes are small. Therefore, it can be approximated that the ground thermal regime approaches an equilibrium state after approximately three years, when the inter-annual changes become negligibly small. The ground temperature at 10 meter depth at P2 (centre of the plate) is about -4.5 °C after 10 years. However, this does not take into account, that the cooling system, at the start of operation, takes

some time to cool the ground down to the desired cooling temperature in reality. The temperature distribution under the plate shows warmer temperatures in the edge areas (P1, P2, P3, P4, P5, P6) of the plate, which can be explained by external seasonal influence of the climatic conditions. It becomes evident (Figure 6.6d and Figure 6.6f) that temperature fluctuation is greatest in these areas. The warmest temperatures however, are experienced at the corner facing the ocean (P6), which is therefore the most critical in regards to choosing a suitable cooling temperature. The temperature development half a meter under the plate at P6, shows that the temperature fluctuates between approximately -6.5 and -2.3 °C.

A detailed analysis of the maximum temperature envelopes for each reference point, presented in Figure 6.8a, highlights the temperature differences per location under the plate. P6 shows the greatest variation of temperature versus depth. In P2, on the other hand, the maximum envelope becomes almost linear and no fluctuations are observed, as the temperature increases steadily with depth until reaching MAGT. The annual temperature trumpet for year 10 in P6, presented in Figure 6.10, shows that the maximum temperatures in the ground at P6 occur in September, so at the end of the warming season. The maximum ground temperature in September in the upper layers reach -2.3 °C. Also visible in Figure 6.8b is that the temperature in February, in surface near areas, is colder than the cooling temperature. This leads to the conclusion that the ambient air cools the edge areas additionally in winter. A visualisation of the ground temperature regime, after ten years for every month, is included in Appendix B.6 in Figure B.10 to B.11. In Figure 6.5 the ground thermal regime and the development of the freezing front after 1 year and after 10 years respectively is shown.

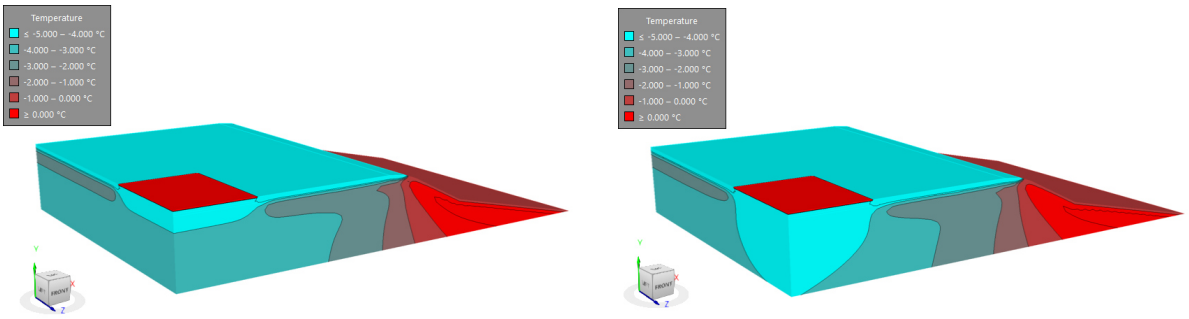

(a) Year 1.

(b) Year 10.

Figure 6.5: Ground thermal regime after one year of cooling and ten years of cooling shows the development of the freezing front under the foundation area.

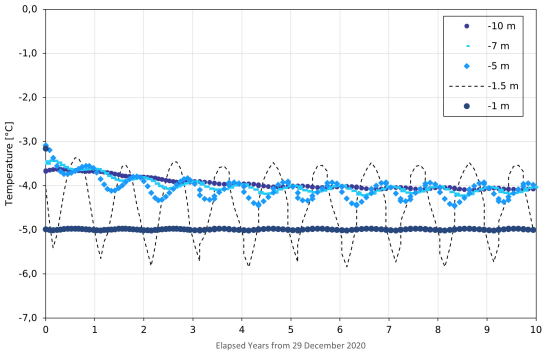

(a) P1.

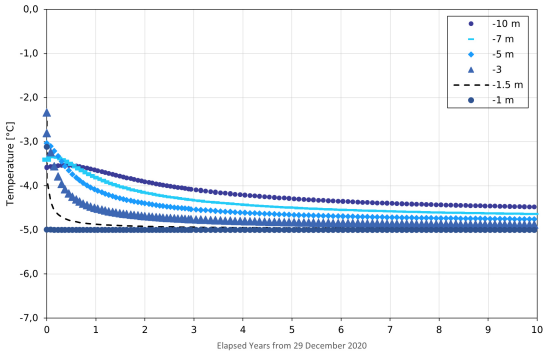

(b) P2.

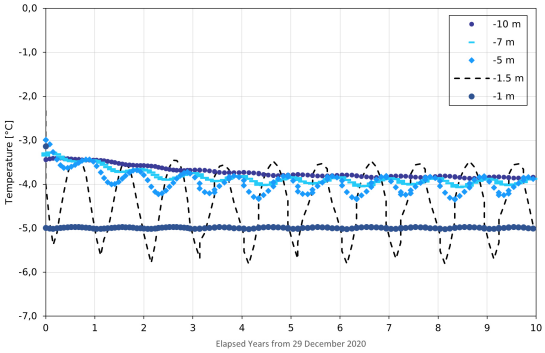

(c) P3.

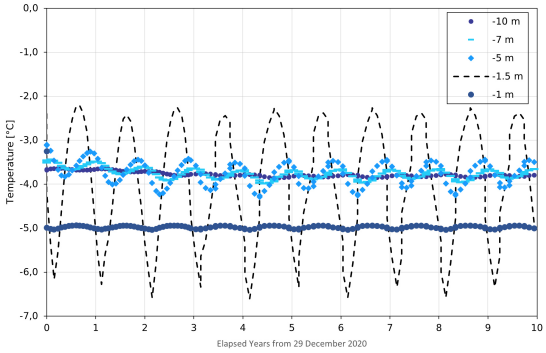

(d) P4.

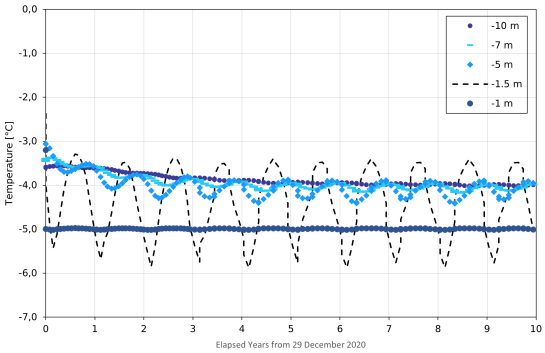

(e) P5.

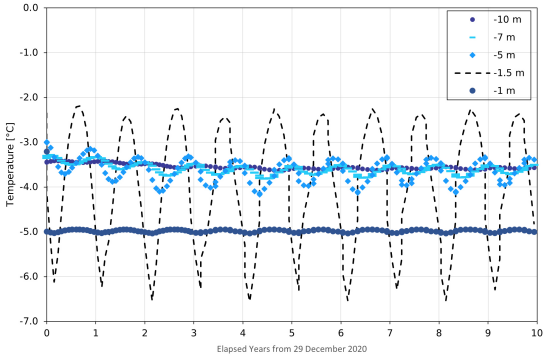

(f) P6.

Figure 6.6: Temperature development in the ground under the plate in chosen depths for a cooling temperature of -5 °C. The highest fluctuation can be observed in P6 and P4, at the corner of the foundation area. P6 indicates that the corner facing the ocean, is the warmest area under the plate. P2 is cooled continuously, without influence from the ambient air, which results in a almost constant ground temperature close to -5 °C.

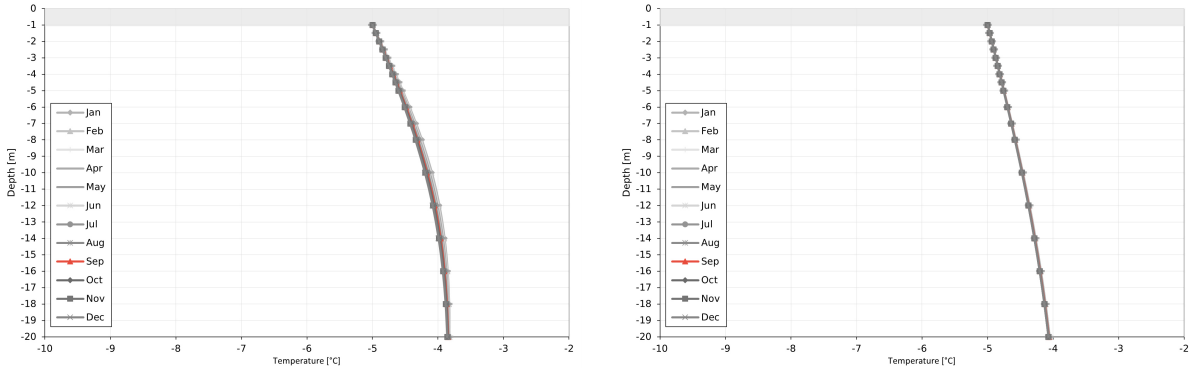

(a) Year 03.

(b) Year 10.

Figure 6.7: Annual temperature profile in P2 at T_p= -5 °C shows that the ground has already adapted to the cooling temperature in year 3. The longer the cooling is run, the more linear the temperature profile becomes, which is evident when comparing year 3 and year 10. The plate is indicated in grey until 1 metre depth.

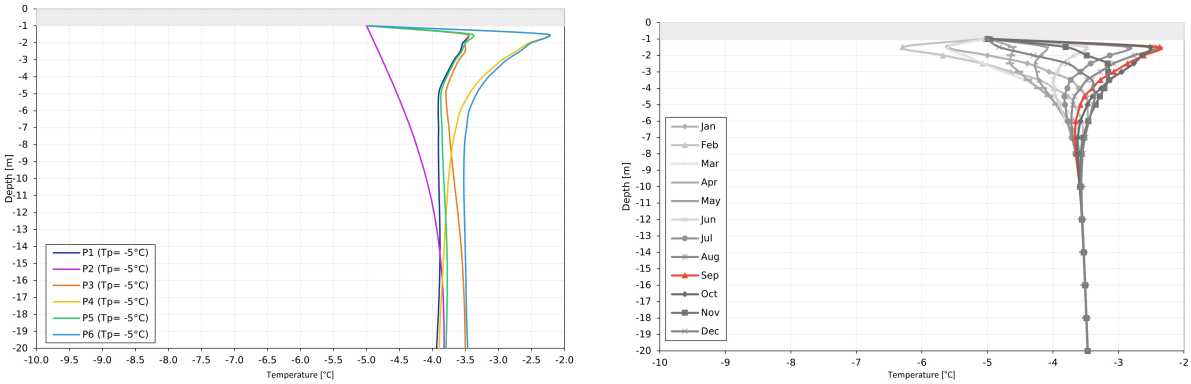

(a) Maximum temperature envelope for year 3 to year 10 for each reference point under the plate until 20 meter depth; the temperature profiles show that P6 is the warmest area under the plate; at P2 the temperature profile becomes almost linear between MAGT and cooling temperature.

(b) Mean monthly temperature profiles for year 10 at P6; in February the ambient air cools the ground traditionally, whereas in September the ground experiences the warmest ground temperatures (red).

Figure 6.8: Temperature profiles for at T_p= -5 °C; the plate is indicated in grey until 1 metre depth.

Temperature Regime from a Cooling Temperature of -10 °C

An overview of temperature development in the ground over time for each reference point is given in Figure 6.9. A steady cooling effect can be observed which decreases over time. The changes between year 9 and 10 at P2, shown in Figure 6.9b, become very small compared to year 3 and 4. A more detailed depiction is shown in Figure 6.11, where the temperature profile for year 3, 4, 5 and 10 are shown respectively. It is evident that the ground is still adjusting to the cooling temperature in year 3. From year 4 onwards, the temperatures have become more constant and the changes become small in a monthly perspective. This indicates that the ground takes long to adjust to a cold cooling temperature and inter-annual thermal equilibrium is approached after 4 to 5 years of simulation. This can be explained

by the large temperature difference of about 6 °C between the cooling temperature and the mean annual ground temperature. The ground temperature at 10 meter depth at P2 (centre of the plate) is about -7.5 °C after 10 years. The temperature development, half a meter under the plate, at P6 show that the temperature fluctuates between approximately -4.5 °C and -9.0 °C.

Seasonal fluctuations are most prominent in P4 and P6 (Figure 6.9d and 6.9f) at the foundation's corners. The maximum envelope for each reference point, shown in Figure 6.10a, indicates that the maximum temperatures lies at -4.3 °C at P6 within 3 metres under the plate. The analysis of the seasonal temperature profile, shown in Figure 6.10b, in year 10 gives insight into the warmest month of the year. The maximum ground temperature of -4.5 °C is reached in September. Figure 6.10b indicates a warming effect from the summer period, but shows an overall cold annual temperature regime, where surface temperatures are adapting to the cooling temperature.

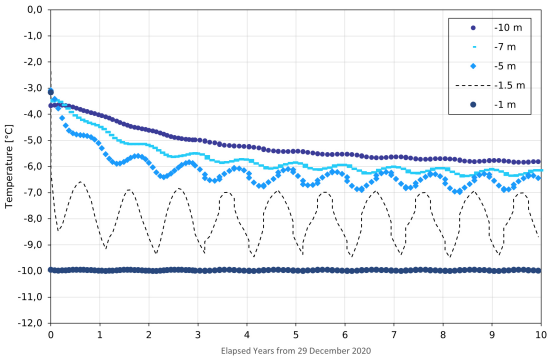

(a) P1.

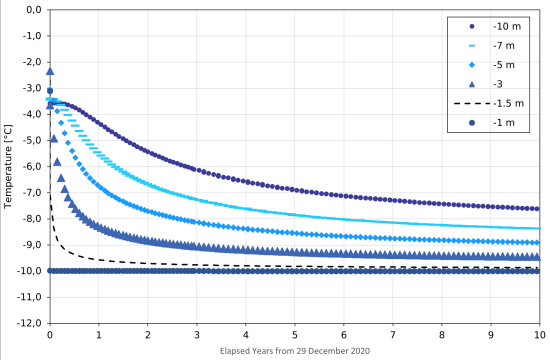

(b) P2.

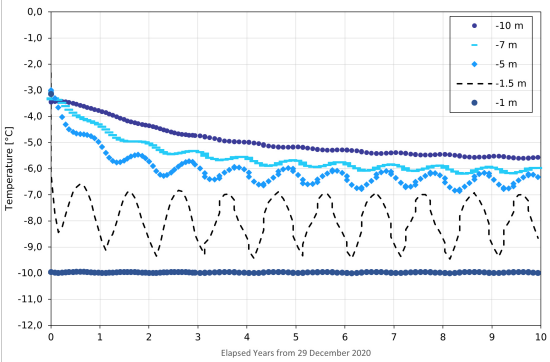

(c) P3.

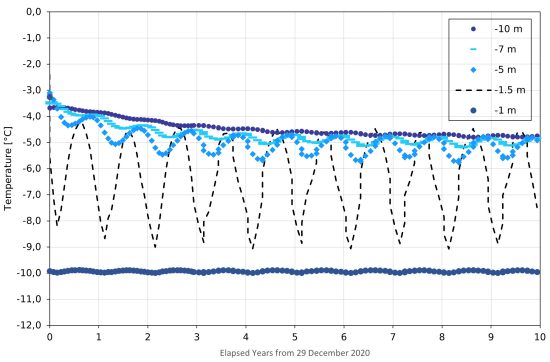

(d) P4.

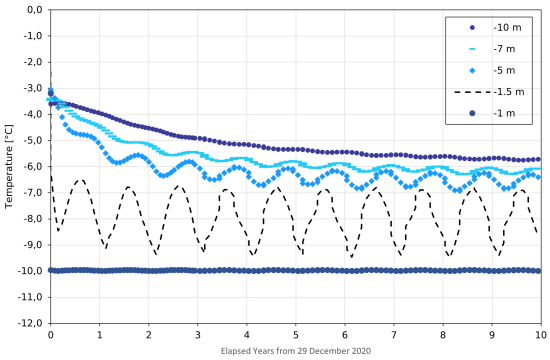

(e) P5.

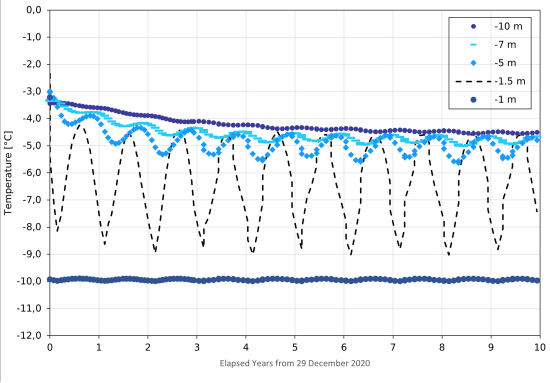

(f) P6.

Figure 6.9: Ground temperature development under the foundation over time in chosen depths for a cooling temperature of -10 °C. The temperature at P2 cools constantly, a higher cooling effect can be observed at the start of the cooling until the ground.

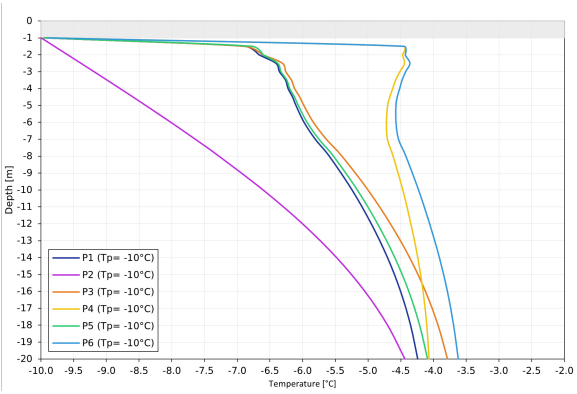

(a) Maximum temperature envelope for year 4 to year 10 for each reference point under the plate until 20 meter depth; the temperature profiles show that P6 is the warmest area under the plate; at P2 the temperature profile becomes almost linear between MAGT and cooling temperature.

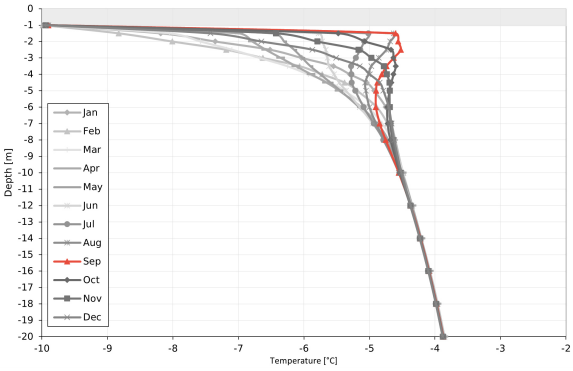

(b) Mean monthly temperature profiles for year 10 at P6; in February the ambient air cools the ground traditionally, whereas in September the ground experiences the warmest ground temperatures (red).

Figure 6.10: Temperature profiles for T_p= -10 °C. The plate is indicated in grey.

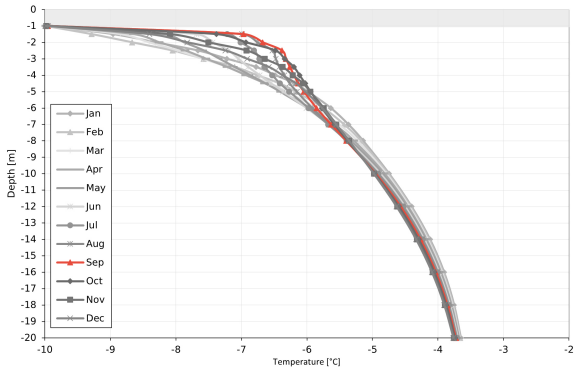

(a) Year 03.

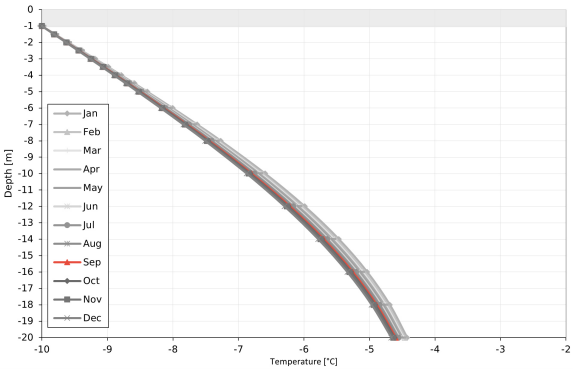

(b) Year 04.

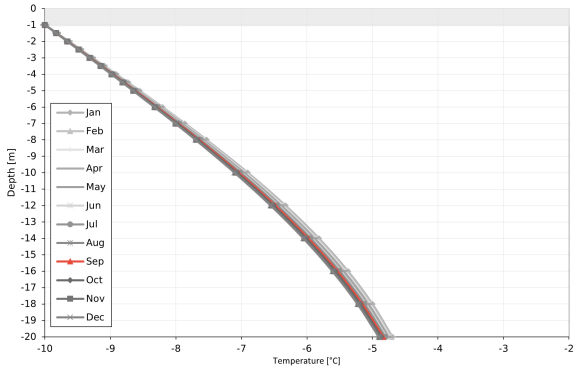

(c) Year 05.

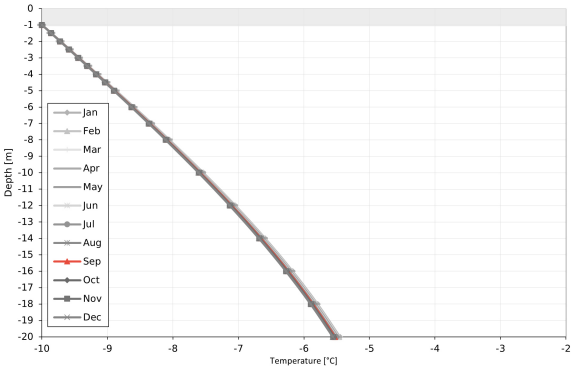

(d) Year 10.

Figure 6.11: Monthly temperature profiles at P2 for T_p=-10 °C for chosen years. (a) shows that the ground is still adjusting to the cooling temperature in year 03; after year 03 it becomes more stable with a steady cooling effect from the cooling temperature; the plate is indicated in grey.

Comparison of Power Requirement and Operating Cost at Different Cooling Temperatures

The amount of energy that needs to be removed from the domain, in order to sustain the cooling temperature at the desired value, equals the summed cumulative energy transfer for the face of the cooling surface boundary in the model. The cumulative energy transfer is a combination of heat flow from the warm temperature regime in the house and an energy gain or loss from the subsoil, depending on the temperature regime, so the season. A conceptual sketch presented in Figure 6.12 shows a simplified system of heat flow in the ground, where Q_1 is the heat flow from the building towards the cooling pipes, Q_2 is the heat flow from the adjacent ground and Q_tot is the heat flow that needs to be extracted by the cooling system. The quantification of energy transfer is interesting in view of the heat pump capacity and its operational cost.

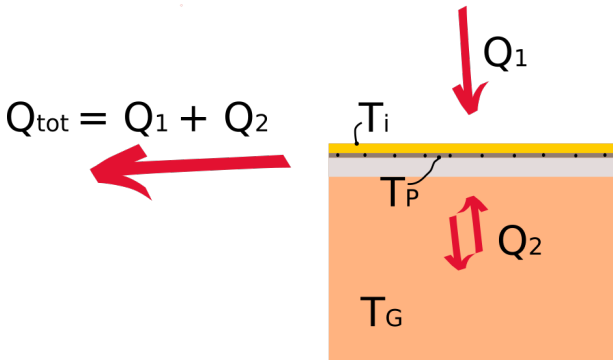

Figure 6.12: Conceptual sketch of the foundation system on the underlying soil; Q_{tot} symbolizes the total heat extracted by the cooling system; Q_1 is the heat flowing from the building (T_i) towards the cooling plate (T_G), Q_2 is the heat flowing towards or away from the cooling pipes dependent on the season and thermal regime in the ground T_G.

The evolution of the heat rate, summed for the cooling pipe surface for the duration of the simulation is shown in Figure 6.13a. A negative heat rate stands for heat loss, so the rate at which heat leaves the ground. The heat rate spikes, when the plate is turned on and then finds a more steady-state condition over the annual cycles. A more detailed representation is shown in 6.13b, where a maximum heat rate can be observed in March and a minimum in August. In a simplified manner it can be assumed that the heat flow from the building above remains constant, if the temperature gradient remains constant, then the variation of heat rate is caused by the seasonal fluctuations of ground temperature. In March heat is flowing towards the adjacent ground to colder areas, whereas in August heat is flowing towards the plate from warmer regions in the subsoil.

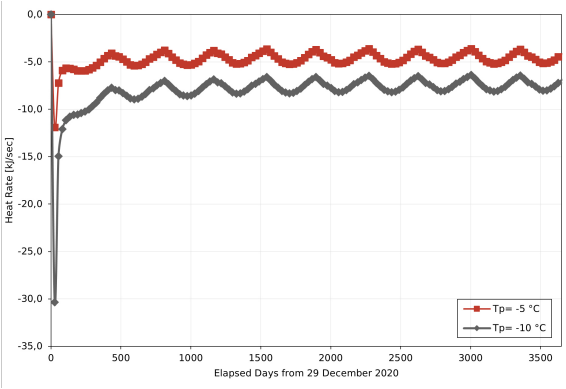

(a) Heat rate from year 0 to 10. It shows a higher heat rate for a colder cooling temperature, as more heat must be extracted to cool the ground.

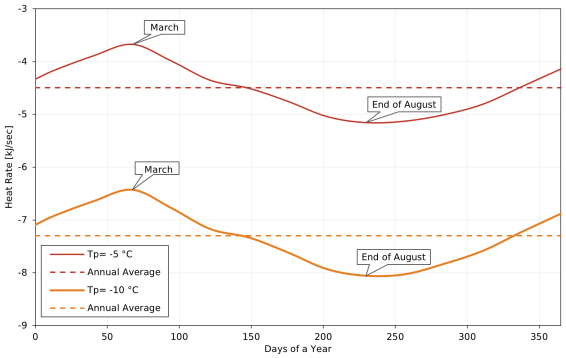

(b) Heat rate development for year 10. The lowest rate of energy transfer is visible in March when the ground is the coldest, the most heat must be extracted from the ground in the end of August after the warming period.

Figure 6.13: Heat rate at the cooling pipe surface for T_p=-5 °C and -10 °C respectively. The negative sign shows that heat must be extracted.

In order to quantify the amount of energy for an annual cycle the cumulative energy transfer is extracted from the model which equals the heat rate integrated over time. The cumulative energy transfer is the total amount of heat that flows through the cooling pipe face, so the heat that needs to be removed from the domain to sustain the desired cooling temperature. The average annual and daily energy that needs to be extracted is shown in Table 6.1. All results from the simulation are multiplied by two to estimate values for the entire footing area. The heat rate can be used to estimate the heat pump's minimum capacity and increases with decreasing cooling temperature.

Table 6.1: Comparison of energy transfer and heat rate for a cooling temperature of T_p=-5 °C and -10 °C respectively.

T_p [°C]	Avg. annual energy transfer [MJ/year]	Avg. daily energy transfer [MJ/day]	Heat rate $\dot{Q}_{tot}$ [kJ/sec], [kW]
-5	-300 374	-823	-9,5
-10	-508 777	-1394	-16,1

The heat rate at which heat flows towards the cooling pipes from the building $\dot{Q}_1$ and from the subsoil $\dot{Q}_2$ respectively is summarized in Table 6.2. It is evident that the heat flow from the soil increases substantially, when the cooling temperature is lowered and thus the temperature difference between MAGT and T_p is increased.

Table 6.2: Heat rate at different cooling temperatures; the negative sign indicates that heat is extracted from the ground; $\dot{Q}_{tot}$ is the total heat rate, $\dot{Q}_1$ is the fraction of heat rate caused by the building above and $\dot{Q}_2$ is the fraction caused by the adjacent ground.

T_p [°C]	$\dot{Q}_{tot}$ [kW]	$\dot{Q}_1$ [kW]	$\dot{Q}_2$ [kW]
-5	-9,5	-8,2	-1,4
-10	-16,1	-10,2	-5,9

A rough cost estimate is made following a methodology used by Goodrich and Plunkett (1990), where the heat extracted and an assumed COP is used to back-calculate the power needed. A COP between 2.0-3.0 is assumed for the system based on estimates for cold climates. Then the electrical energy needed to run the system is back calculated from Equation 2.17. The calculation results are presented in Table 6.3 for different COPs. The annual cost to operate the heat pump cooling system at a 24-hour operation is shown in Figure 6.14. The price of electricity for Longyearbyen was not available, therefore the price for electricity in Tromsø 2019 (mainland Norway) at 378 NOK/MWh, was adopted (Nord Pool, nd). The operational cost lies between 16 000 to 32 000 NOK (or 1 300 to 2 800 EUR) for T_p=-5 °C and 27 000 to 54 000 NOK for T_p=-10 °C. It is evident that the price increases with decreasing cooling temperature.

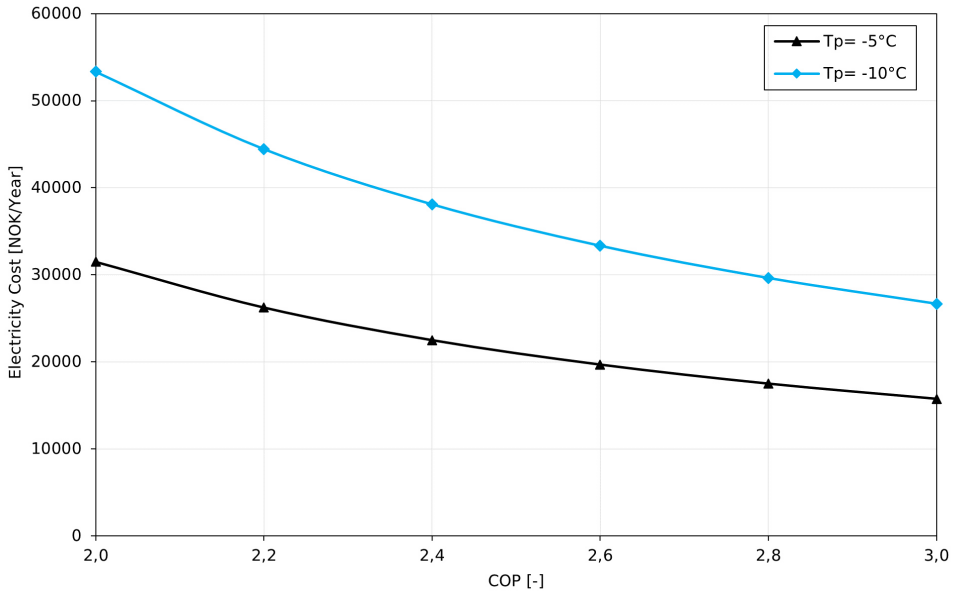

Figure 6.14: Yearly operational cost dependent on the COP of the heat pump system for T_p=-5 °C and -10 °C. The price increases with decreasing cooling temperature.

Table 6.3: Cost comparison for a 24-hour per day operation of the heat pump for T_p=-5 °C and -10 °C at different COPs.

T_p	COP	Electricity (24-h operation)		Electricity Price	Annual Cost	
[°C]	[-]	[kW]	[kWh per day]	[NOK/kWh]	[NOK]	[EUR]
-5	2.0	9.5	228.6	0.4	31 480	3 148
-5	2.2	7.9	190.5	0.4	26 233	2 623
-5	2.4	6.8	163.3	0.4	22 486	2 249
-5	2.6	6.0	142.9	0.4	19 675	1 968
-5	2.8	5.3	127.0	0.4	17 489	1 749
-5	3.0	4.8	114.3	0.4	15 740	1 574
-10	2.0	16.1	387.2	0.4	53 321	5 332
-10	2.2	13.4	322.7	0.4	44 434	4 443
-10	2.4	11.5	276.6	0.4	38 087	3 809
-10	2.6	10.1	242.0	0.4	33 326	3 333
-10	2.8	9.0	215.1	0.4	29 623	2 962
-10	3.0	8.1	193.6	0.4	26 661	2 666

6.2.3 Discussion

The most critical areas for both simulated cooling temperatures are located in the area of P6, at the corner of the foundation, located in vicinity to the ocean. This is an important finding, as it shows that a suitable cooling temperature must be chosen in accordance to the corner areas, where temperatures can be almost 3 °C warmer than the cooling temperature. A cooling temperature of -5 °C can be critical, if climate warms and if the soil has a high salinity content resulting in a freezing point depression. Nowadays, the soil remains frozen, but the safety margin is very small. Also, the temperatures produced by the model can vary in accuracy of ±1 °C as shown in subsection 5.3.1.

The power requirement and cost does not increase significantly with a 5°C decrease of cooling temperature. In the worst case, the cost increases by approximately 11 000 NOK per year for a cooling temperature of -10 °C. The minimum heat pump capacity for T_p=-10 °C increases by about 7 kW compared to T_p=-5 °C. The initial costs of the heat pump are not included here, but the larger the necessary heat pump capacity, the higher the initial cost.

6.3 Seasonal Cooling of the Plate

The purpose of this study is to investigate the thermal response of the soil when the cooling system is turned off seasonally. The study of seasonal cooling is conducted for a cooling temperature of -5 °C. Thus, the analysis is run with the same conditions as stated in section 6.2.2, but after 4 years the cooling is turned off seasonally. The scenario aims to investigate the possibility to turn off the cooling system during the coldest months of the year to

lower the energy needs of the system and optimize the usage of renewable energy, especially solar energy. Also, there is an abundance of solar radiation in summer season, but in the Arctic the winter season is characterised by polar darkness, which means no solar radiation from approximately the end of October to mid February. This indicates that a shut off during this period can aid to save electricity, which in the dark season, can not be generated by harvesting solar energy.

The analysis is started after year 4 when the ground thermal regime down to DZAA has established an inter-annual steady-state condition, which indicates that the freezing front is fully developed. Here, the cooling is turned on from April to December and turned off for the three coldest months in the year: January, February and March. This is simulated by removing the cooling temperature boundary condition from the top of the gravel layer for these 3 months as shown in Figure 6.15.

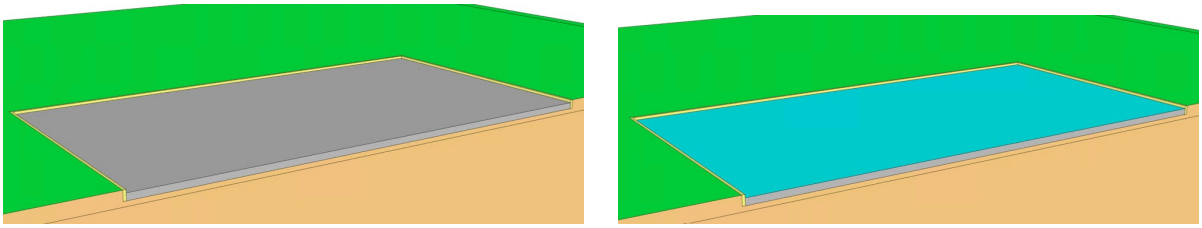

(a) Applied boundary conditions for the 'no cooling' period: the cooling temperature is removed from the upper gravel face.

(b) Applied boundary conditions for the 'cooling' period: the cooling temperature is applied to the upper gravel face.

Figure 6.15: Difference in boundary condition for the seasonal cooling scenario.

6.3.1 Results

Figure 6.16 shows the temperature field at P2 and P6 respectively over time as these areas show the most extremes in view of ground temperature evolution. The temperature at P2 directly under the plate, so at one meter depth, shows that an increase of 2.2 °C in 3 months is generated. At P6 where additional cooling is obtained from the adjacent ground, the temperature just under the plate increases by 1.8 °C. The ground temperatures at P6 from half a meter below the plate onwards are colder than -5 °C in winter, due to the additional cooling effect of the cold ambient air. The most critical area in this scenarios is in the centre of the plate, where the ground constantly warms from the heated building above. The corner and edge areas experience additional cooling from the cold ambient air which naturally lowers the temperature in these areas. An overview of the temperature regime for the entire model domain before the cooling is turned off and at the end of the 'no cooling' period is shown in Figure 6.17. This visualizes the warming effect in areas adjacent to the foundation caused by

the constant heat flux from the building above.

When comparing 5 years of seasonal cooling to a constant cooling operation, an average heat rate of 8.5 kW compared to 9.2 kW is present. That equals an average energy saving over the duration of 5 years equal to 57 300 kJ per day or 0.7 kJ per sec (kW). At an electricity price of 0.4 NOK/kWh and a saving of 16 kWh per day (0.7 kW for 24 hours operation per day) this equals a cost saving of approximately 2 300 NOK (or 2 300 EUR) per year. It is visible in Figure 6.18, that the energy saving increases with time compared to a constant cooling operation.

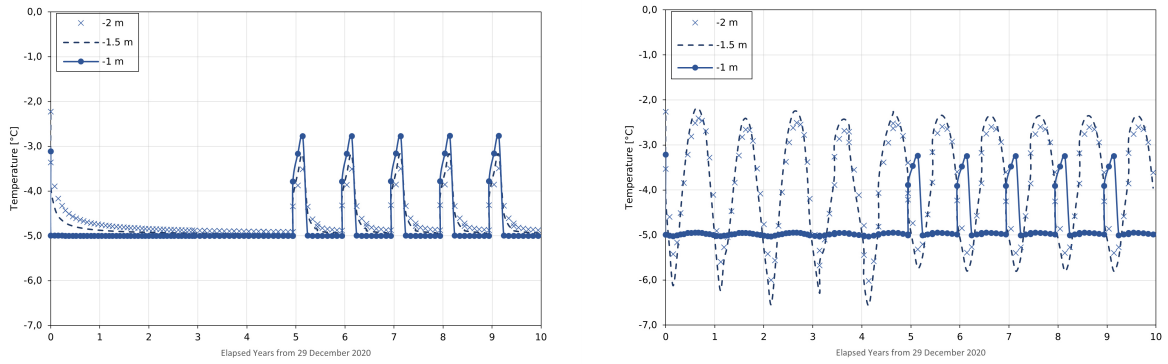

(a) P2: Foundation centre.

(b) P6: Eastern foundation corner close to the ocean.

Figure 6.16: Temperature evolution under the plate for different depths; 1 metre depth is at the bottom of foundation. The seasonal cooling is started at year 5 when a fluctuation in temperature can also be observed at P2 in the centre of the plate.

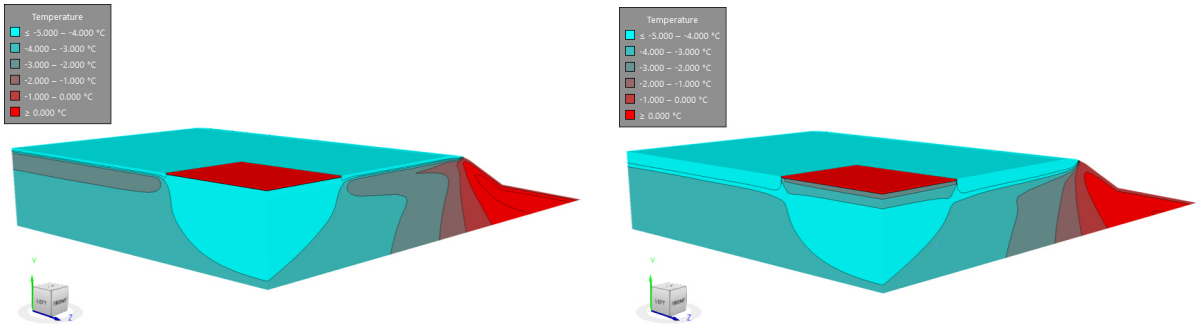

(a) Temperature field in December before the cooling is turned off shows a temperature field below -4 °C under the entire foundation area.

(b) Temperature field in March before the cooling is turned on again shows a warming of the upper soil under the entire foundation area down to a range of -1 °to -2 °C.

Figure 6.17: Temperature distribution in the model domain just before the cooling is turned off and turned back on again.

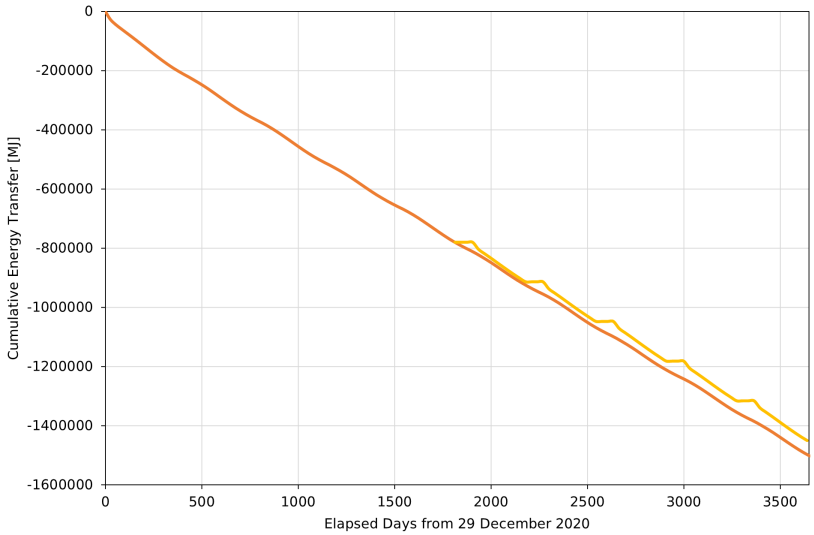

Figure 6.18: Cumulative energy transfer for a constant operation (orange) and a seasonal operation (yellow) shows that energy is saved during seasonal operation.

6.3.2 Discussion

Seasonal cooling does not lead to an increase of temperature above 0 °C, however a substantial temperature increase in the centre of the plate can be observed. In situation of seasonal cooling, when the cooling is turned off in winter months, the most critical area is in the centre of the plate as a constant heat flow from the building above warms the ground and no additional cooling effect from the colder adjacent ground is present.

The energy saving increases over time compared to constant operation, after 5 years the average heat rate has decreased by 0.7 kW which equals 2 300 NOK in annual saving. This amount is not significant, however a big advantage of the seasonal cooling also lies in the ability to save electricity in winter months. If the system is coupled with solar collectors for the production of energy, the ability to turn the cooling off in winter months, when no solar radiation is available to produce electricity, helps to create an innovative off-grid technology.

6.4 Power Failure

This analysis investigates the ground's thermal response in an event of power failure of the cooling system. The scenario simulated in this incorporates a power failure in June, when the ground is already warming. The simulation is run for one year, where the initial condition is adopted from June after 10 years of cooling. All boundary conditions are unchanged to the prior analysis apart from the condition at the cooling pipe surface, where the cooling temperature is removed.

6.4.1 Results

Again, a more detailed analysis is presented for P2 and P6 as they show the largest variation of temperature development. Figure 6.19a and 6.19b display the respective ground temperature trumpets underneath the plate for the duration of power failure at P2 and P6. The trumpet at P2 indicates that the ground under the plate is constantly warming down to a depth of 12 metres. At P6 temperature fluctuations can be observed and the deeper soil is not warming as much as at P2. At P6 the most critical temperatures occur within 2 meters under the plate. Figure 6.19d shows that at P6 the ground experiences cooling from the ambient air temperature as 9 months after power failure in March the ground reaches almost -5 °C naturally. However, in summer months the ground also experiences accelerated warming by the warmer air temperature. Looking at Figure 6.19c, the upper temperature field at P2 in the centre of the plate, it is evident that the ground steadily warms under the impact of the building on top. In July, a year after the failure of the cooling system, the temperature at the bottom face of the foundation at P6 is -0.7 °C and at P2 it is -0.8 °C. Thus, the ground temperature still remains below 0 °C, but has warmed more than 4 °C in one year. A ground temperature of this magnitude can be critical in view of strength and bearing capacity of the ground.

Figure 6.20 displays the development of the temperature field under the plate exemplary for June. The thermal regime just before and after one year of power failure is visible. It is evident that only a small area with ground temperatures above -4 °C remains in the subsoil, and the ground adjacent to the plate has warmed up significantly.

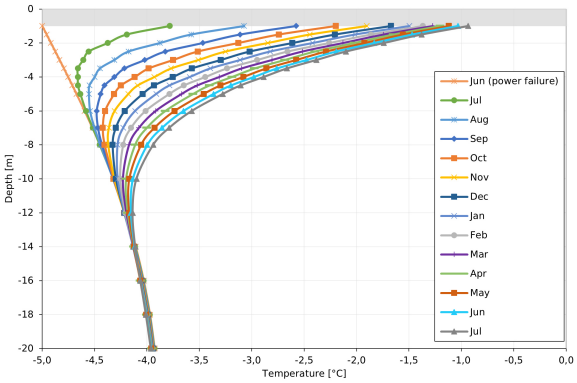

(a) Monthly temperature evolution at P2 during power failure shows a constant warming of the subsoil.

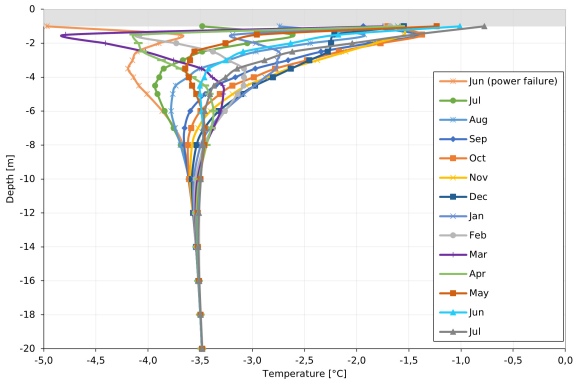

(b) Monthly temperature evolution at P6 during power failure shows that seasonal fluctuations cool and warm the ground additionally.

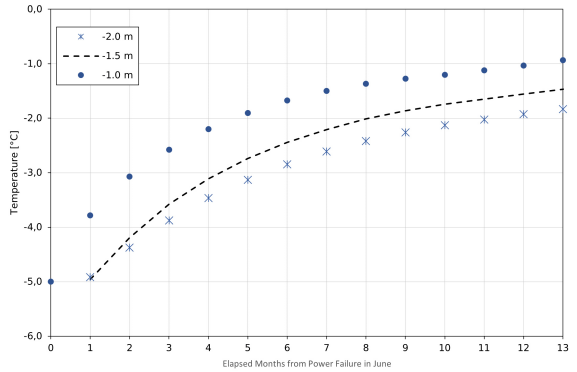

(c) P2; the ground temperature one metre below the foundation experiences significant steady warming.

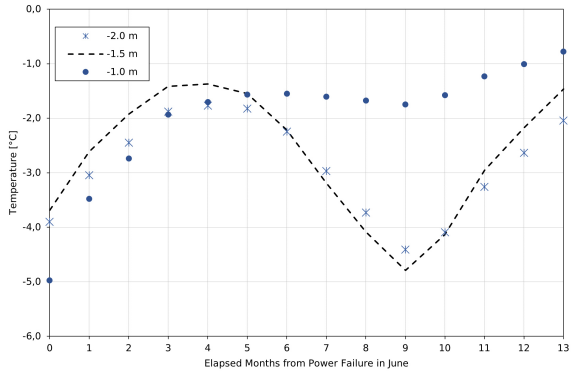

(d) P6; the ground temperature one metre below the foundation experiences significant warming; a cooling effect on the ground from the ambient air can be observed in winter months.

Figure 6.19: Temperature regime in P2 and P6 respectively during power failure of the heat-pump cooling system.

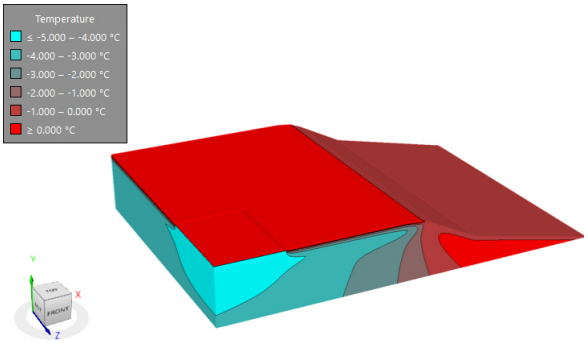

(a) Right before power failure (June).

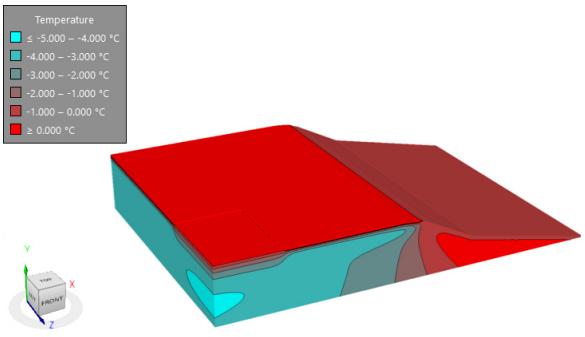

(b) One year after power failure (June).

Figure 6.20: Temperature regime for the entire model domain in a power failure scenario for the cooling system.

6.4.2 Discussion

After one year of power failure the ground temperature for a cooling temperature of -5 °C are above -1 °C in some areas under the foundation. This temperature range can be critical

in view of strength and bearing capacity of the ground. The simulation is only run for one climatic scenario, thus if the power failure occurs in a year of warmer climate the conditions can be even more critical. It is therefore of utter importance to establish a proper monitoring system to avoid damages as previously observed at other projects around Longyearbyen.

6.5 Effects of Climate Change

The effects of climate change on ground temperatures are simulated for the 50 year service lifetime of the building for a cooling temperature of -5 °C. The geometry, mesh and material properties are adopted from the first analysis, studying the ground's behaviour at a cooling temperature of -5 °C. The upper boundary conditions are discussed in more detail in the following. The time stepping is set to 27 days to cover each month of the year. The analysis starts in January 2021 and ends in December 2072, so 50 years after the hand-over of the building in 2022.

6.5.1 Forcing Data

Projected Air Temperature

Global climate models are used to project the future climatic condition based on greenhouse gas emission scenarios. The projections for a local scale are derived by empirical statistical downscaling. Often, projections are dependent on emission scenarios defined by the Intergovernmental Panel on Climate Change (IPCC). IPCC (2013) defines *Representative Concentration Pathways* (RCP) based on the concentration of greenhouse gas in the atmosphere. In this study, three scenarios, ranging from low to high emission, are addressed. RCP2.6 stands for drastic emission reduction starting from 2020, RCP4.5 stands for a slow increase until 2050 followed by reductions and RCP8.5 stands for no changes in emission rate compared to 2005 (Hanssen-Bauer et al., 2019). The numbers define the respective human-induced warming effect in Watt per square metre.

For this study no data set from climate models for projected monthly mean air temperature is available. Instanes (2016) proposes a methodology to incorporate climate warming scenarios for engineering design by combining projections from empirical downscaled models and historical local temperature data to incorporate the natural variability of temperature fluctuations. This methodology is adopted for this study, although in a simplified manner.

Projections for absolute temperature change for Svalbard Airport from 1971-2000 for 60

years are shown in Table 6.4, which are adapted from Hanssen-Bauer et al. (2019) and present the medians of the temperature ensembles, which are recommended to study consequences from climate change. The projections are stated in absolute numbers. The control period for the projections in Hanssen-Bauer et al. (2019) is 1971-2000, however temperature data dating back to 1971 are not available to the author. Also, projection for this study are only relevant for future years and not starting from 2000. Therefore the mean daily temperatures from 2001-2020 are used to obtain natural variability for the projections and the projected absolute temperature changes from Hanssen-Bauer et al. (2019) from 1971-2000 for 60 years are divided by three, as presented in Table 6.5, to be able to make projections from 2001-2020 for the next 50 years. Noteworthy is that the projections are until 2060 in Hanssen-Bauer et al. (2019) but the same values are used in this study for projections until 2072 since this covers 50 years of service lifetime for the building from 2022.

So for this study, the absolute projected change for 60 years is divided by 3 to obtain a temperature change per 20 years. Further, historic climate data from Svalbard Airport is used to ensure natural variability of the temperature. The historic daily air temperature data from 2001-2020 is used and a dataset is created by copying the data three times, so until 2080. Then the absolute change per 20 years is applied to the historic data. Thus, for example projections for 2030 are created by applying the absolute temperature change per 20 years to the temperature readings from 2010 and so on. This way a data set for future projections for the service lifetime of 50 years is compiled. The adopted methodology leads to uncertainties in regards to the forcing data for the simulation as the methodology is not commonly used in research studies.

Table 6.4: Projected annual and seasonal temperature changes for 60 years from 1971-2000 from ESD for medium percentile at Svalbard Airport, values are taken from Hanssen-Bauer et al. (2019).

	RCP2.6 [°C]	RCP4.5 [°C]	RCP8.5 [°C]
Annual	2.7	3.5	3.9
December, January, February	3.3	4.8	5.6
March, April, May	2.1	3	3.5
June, July, August	0.9	1.2	1.5
September, October, November	3.9	5	5.5

Table 6.5: Calculated projected annual and seasonal temperature changes per 20 years from 1971-2000.

	RCP2.6 [°C]	RCP4.5 [°C]	RCP8.5 [°C]
Annual	0.90	1.17	1.30
December, January, February	1.10	1.60	1.87
March, April, May	0.70	1.00	1.17
June, July, August	0.30	0.40	0.50
September, October, November	1.30	1.67	1.83

The projections in form of mean annual air temperature is shown in Figure 6.21, where it is obvious that RCP8.5 is the most critical development. The 30-year mean annual air temperature shows an increase in mean annual air temperature from -3.4 °C in 2020 to 0 °C in 2072 for RCP8.5. The projections for different time slices are shown in Figure 6.22. The mean annual air temperature steadily increases, but seasonal projections vary due to the natural variability, e.g. the projection for March 2060 is colder than for March 2050. And the variability of each year from 2001-2020 is repeated every 20 years, so 2020 is repeated in 2040 and 2060.

Figure 6.21: Historic and projected mean annual air temperature for Svalbard Airport for different representative concentration pathways until 2072. The 30-year mean projection shows a warming up to 0 °C mean annual air temperature until 2072.

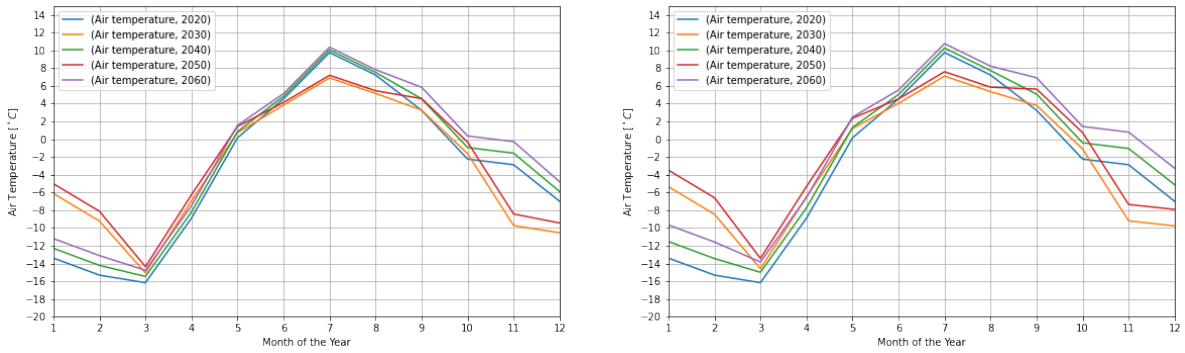

(a) RCP2.6.

(b) RCP8.5.

Figure 6.22: Projected mean monthly temperatures for RCP2.6 and RCP8.5 for different years at Svalbard Airport. The effect of natural variability is evident, e.g. July 2020 is warmer then July 2050. Also it is noticeable that the natural variability is repeated, e.g. variability from 2020 is repeated in 2040 and 2060, so every 20 years, as the temperature from the past 20 years is taken as a base and projected for the next decades.

Since the most critical situation is of interest for this study, only studies from RCP8.5 are presented here. The projected air temperature is applied in form of a step function consisting of mean monthly values for a period of 50 years as shown in Figure 6.23. The mean monthly air temperature values are applied with seasonal n-factors of 1.0. The thawing n-factor of 1.0 has shown good results for this study as discussed in subsection 5.2.7. The freezing n-factor is also set to 1.0, this generates a colder data set than prior cases with a n-factor of 0.86. However, a n-factor of 1.0 is chosen, since its development in a climate warming scenario is uncertain.

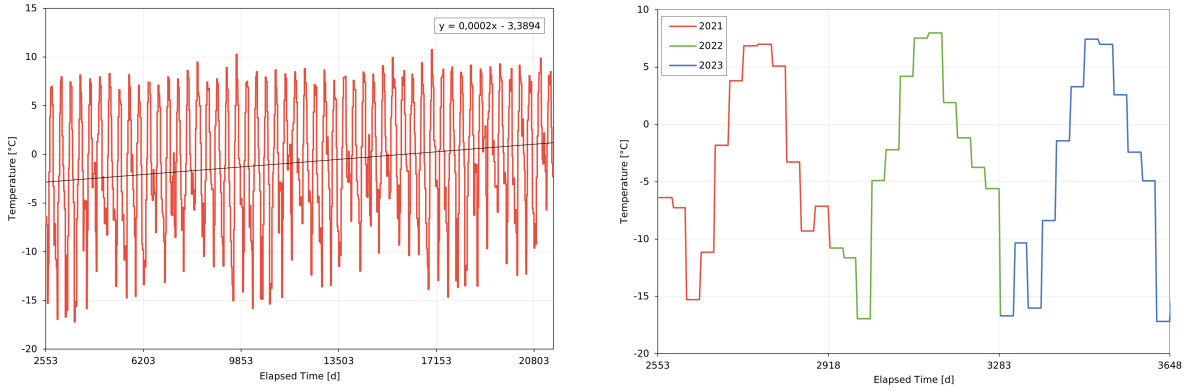

(a) Step function of applied air temperature for the entire analysis.

(b) Step function exemplary shown for 4 years.

Figure 6.23: Step function of mean monthly air temperature applied for the simulation from 2021-2072.

Projected Sea Surface Temperature

The sea surface temperature is projected to rise, but changes around Longyearbyen are small. A projection for Isfjorden shows a change of mean monthly sea surface temperature between

0 and 0.2 °C in the area of Longyearbyen until 2069. Due to this projection and the fact that not sufficient projections for other months are available, no change in sea surface temperature due to climate change is considered in this study. This can underestimate the warming effect over the next 50 years but in view of the magnitude of projected air temperature changes, the warming will be more significant from the land surface than the sea surface. Therefore the same step function as earlier elaborated is applied for this study and cycled throughout the analysis.

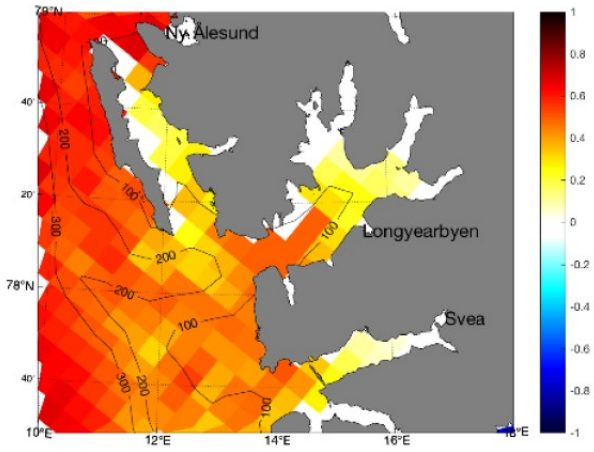

Figure 6.24: Projected change in monthly sea surface temperature for March in RCP4.5 scenario from 2010-2019 to 2060-2069 (Hanssen-Bauer et al., 2019).

6.5.2 Results

The results for the highest emission scenario RCP8.5 are presented here, as it is the worst case scenario for this study. Firstly, the temperature regime in the natural ground in H2 is investigated to check, if the ground remains frozen for this period. If the ground temperatures around the foundation area rise above freezing point, the solution would not be appropriate any more, as the area under the foundation plate would be the only remaining permafrost in the area and an extensive heat flow and moisture migration towards the plate would be generated. Furthermore, the temperature profile under the plate is investigated to quantify the effect of climate warming on the temperatures under the plate. Finally, a comparison of heat rate nowadays and in 50 years under projected climate warming is shown.

The projected climatic conditions result in a stronger warming of winter than summer months, which leads to a greater warming in respect to the minimum ground temperatures as opposed to the maximum ground temperatures, shown for H2 in Figure 6.26. A comparison of maximum ground temperatures in H2, for year 2021 and 2072, shows that the active layer increases approximately 0.5 metres from 1.5 to 2.0 metres depth. The permafrost tem-

perature at 20 m depth warms approximately 1 °C in 50 years to -3.1 °C. The minimum temperature envelope shows an extensive shift to warmer temperatures especially in the upper 2 metres, with an increase of up to 10 °C from 2021 to 2072. However, the ground adjacent to the building remains permanently frozen in summer and winter season. The thermal regime exemplary for 2026 and 2072 for the coldest and warmest month is shown in Figure 6.27, where it is obvious that the adjacent ground remains frozen even though it experiences substantial warming.

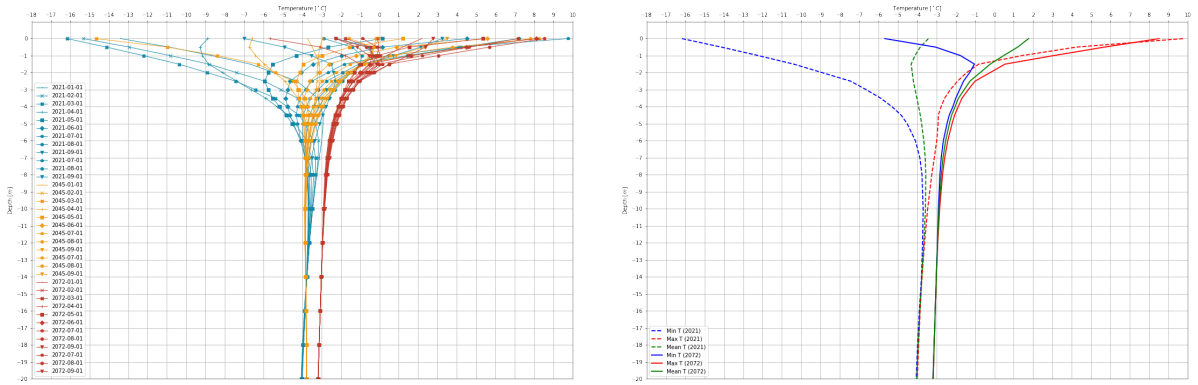

(a) Temperature trumpet for 2021, 2045 and 2072.

(b) Maximum, minimum and mean temperature envelope for 2021, 2045 and 2072.

Figure 6.25: Temperature profile in H2 for different years of the simulation shows extensive warming until 2072.

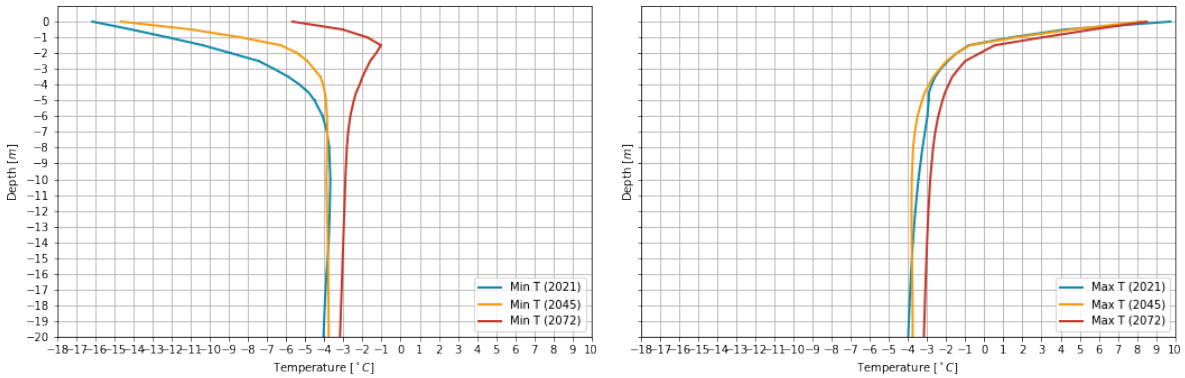

Figure 6.26: Minimum (left) and maximum (right) envelope in H2 for 2021 and 2072 shows that greater warming is experienced in winter than summer.

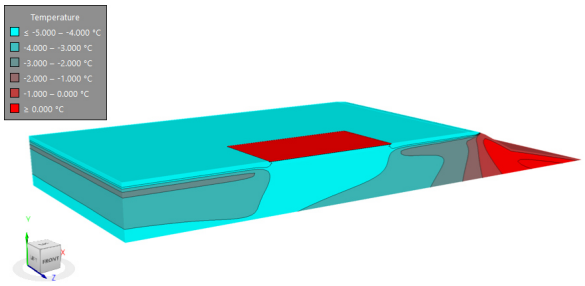

(a) March 2026.

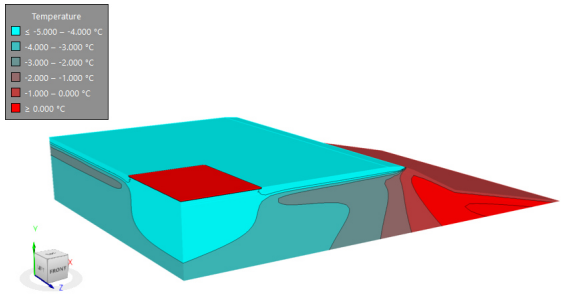

(b) March 2026.

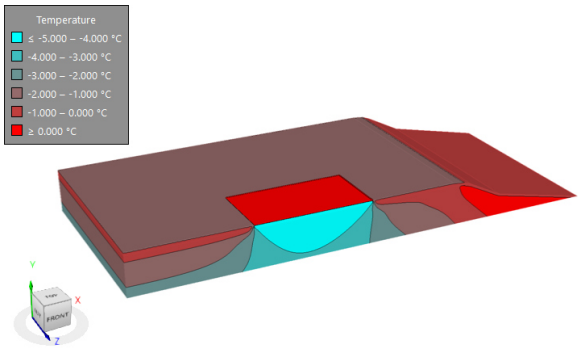

(c) March 2072.

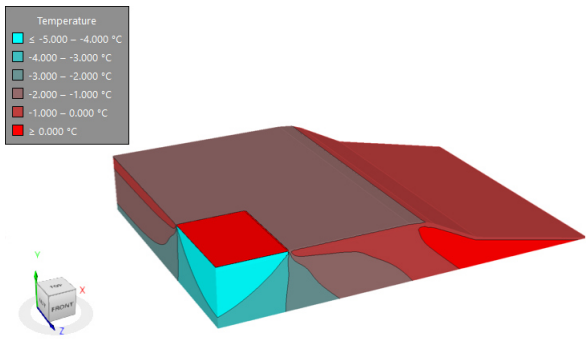

(d) March 2072.

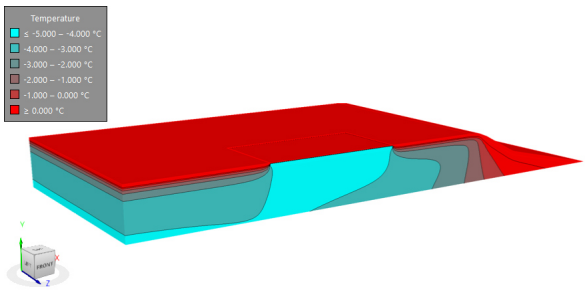

(e) End of August 2026.

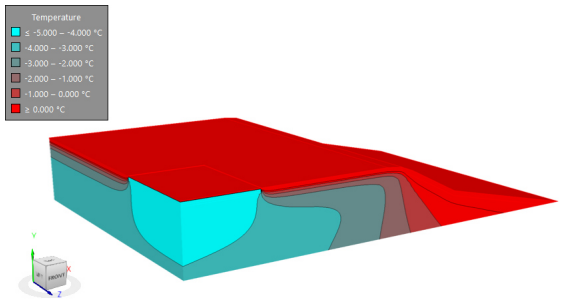

(f) End of August 2026.

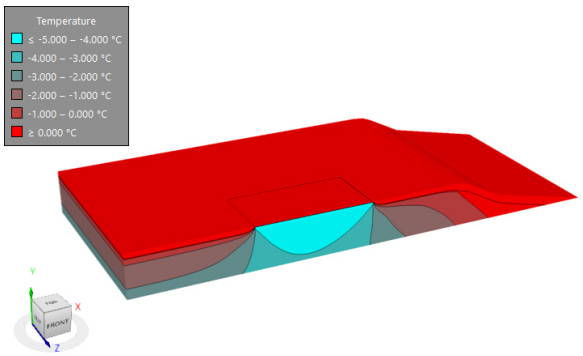

(g) End of August 2072.

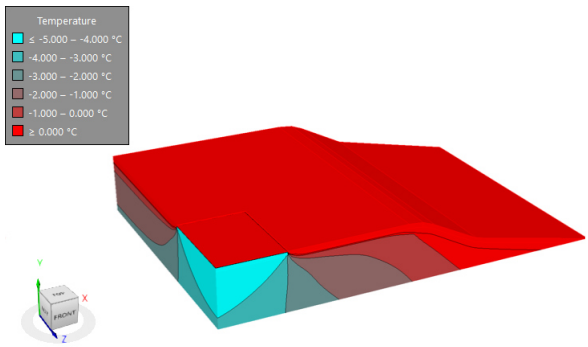

(h) End of August 2072.

Figure 6.27: Thermal regime in 2026 and 2072 respectively; substantial warming of the adjacent ground is evident in winter and summer season.

The most critical temperatures are experienced at P6. The monthly temperature profile and the maximum temperature envelope for the entire study at P6 is shown in Figure 6.28. It is evident that the most critical temperature is experienced in September, after the warming

period about half a meter under the plate. The maximum temperature at P6 lies around -1 °C.

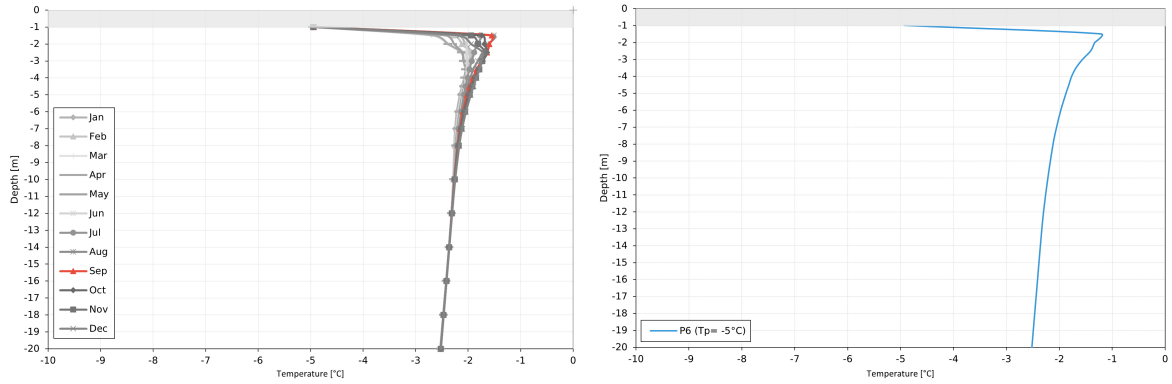

(a) Monthly temperature profile for 2072 at P6.

(b) Maximum temperature profile for 2021 - 2072 at P6.

Figure 6.28: Temperature profiles at P6 show that the most critical temperatures are experienced in August in the ground about half a meter under the plate.

A comparison of the average heat rate under climatic conditions nowadays and in the future shows a slight increase in energy transfer. The heat rate simulated at the cooling surface is multiplied by two to obtain a total number for the entire footing area. At a cooling temperature of -5 °C for climate projection for the next 50 years, the average heat rate at the cooling surface is 10.3 kW compared to 9.5 kW for the situation today. The results are summarized in Table 6.6.

Table 6.6: Average energy transfer and heat rate under climate warming for a simulation until 2072 and the difference in heat rate to conditions nowadays.

T_p [°C]	Avg. annual energy transfer [MJ/year]	Avg. daily energy transfer [MJ/day]	Heat rate $\dot{Q}_{tot}$ [kJ/sec], [kW]	$\Delta\dot{Q}_{tot}$ [kJ/sec], [kW]
-5	-32 4407	-889	-10,3	-0,8

6.5.3 Discussion

The chosen foundation solution presents a suitable solution also in light of climate change for the next 50 years. The adjacent subsoil remains permanently frozen and an increase in active layer thickness of 0.5 metres in the adjacent soil should not affect the integrity of the structure. The ground under the plate remains frozen. However, an increase of air temperature has an impact on the temperature field in the corner areas. Therefore, cooling temperature of -5 °C results in temperatures up to almost -1 °C at P6 in 2072 compared to -2.3 °C in 2021. Therefore a cooling temperature of -5°C results in very warm areas under the plate, which can become critical in view of settlements and strength loss.

6.6 Limitations

The results of this study are based on a numerical model which is verified with field temperature measurements. Numerical models are a powerful tool to simulate the real situation, its simplification is a vital part in building a model and keep the computational cost in an acceptable range. By doing so, numerous limitations apply which have been also further discussed in section 3.1.

Also, results are influenced by availability and accuracy of field measurements which can introduce uncertainties. The limitations for this study are listed to give a comprehensive overview. Steps for further improvement are proposed, if applicable:

- Soil properties and stratigraphy for the model domain is based on very limited soil investigation and might not fully represent the real situation. For higher accuracy of the results, field investigation with soil sampling for different depths should be performed, followed by laboratory analyses to determine the soil's physical and thermal properties. Deep boreholes can give a better understanding of the deeper thermal regime and the bottom of the permafrost and the influence of the geothermal heat flux which could be incorporated to define a suitable lower boundary condition.

- The vicinity to the sea can lead to a freezing point depression which is not accounted for in this study. Freezing point depressions can be large in saline soils close to the ocean. The study of salinity would give more insight into the upper limit of required cooling temperature.

- The thermistors are not calibrated prior to installation. Calibrating the thermistor strings would give certainty about the field measurements. A calibration factor can be defined with which the data can be modified while processing and prior to analysing to account for inaccuracy caused by the instrument.

- The most consistent ground temperature data set covers 1.5 years. A longer time series would be preferable to calibrate soil properties, estimate n-factors, etc. to give more confidence to results and account for the properties variability. Also, temperature readings during the time of the construction would give valuable data for comparing model results after installation of the plate.

- There is no climate data measured at the site, thus measurements from nearby meteorological stations are used (Svalbard Airport, Adventdalen). Local variations can limit

the accuracy of the model. Ground surface temperature at site are taken from measurements from thermistors at 0 m depth. These must be treated with caution, as the thermistor is set up in a plastic tube with a closed lid which can alter the temperature.

- Ideally the model should also include effects of moisture migration. When a temperature gradient exists, vapour diffuses from higher temperature zones and condenses in the colder region. Thus moisture can accumulate in areas of cold temperatures. Possible effects of moisture migration include ice built up under the plate causing frost heaving. The project area is one of the wettest areas in Longyearbyen and thus the incorporation of moisture migration can be very relevant.
- The foundation system is simplified in a manner to minimize the computational cost of the model. It is assumed that the cooling of the ground takes place homogeneously. Therefore, differences in terms of cooling propagation are not accounted for.

Chapter 7

Summary and Conclusions

This study addressed the challenges, which lie in a sustainable development of permafrost regions in the light of climate and human-induced warming of the subsoil. The warming of the ground can lead to differential settlements and ground subsidence. Special foundation solutions were discussed, which ensure the structural integrity of structures founded on permafrost. The modern solutions focus on maintaining the permafrost thermal regime. The focus during this study was put on heat-pump cooling foundations, which artificially keep the ground under a building frozen, by extracting heat from the ground through ground loops and a heat carrier fluid. The active control of the systems enables to adapt the system to changing climatic conditions.

This study concentrated on a current heat-pump cooling project in Longyearbyen, where a foundation area of 3 400 m² is permanently cooled during the lifetime of the building. A verified numerical thermal 3D model was built to investigate the ground's thermal regime in the ground and to numerically study the soil's thermal response under four different scenarios.

First, the suitability of two different cooling temperatures, to keep the ground under the foundation area frozen, was studied. Additionally, the effects of seasonal cooling to optimize the energy usage, with an operation scheme of 9 months operation and 3 months shut down, was investigated. Then, a power failure, which is the most common cause of failure for this solution in Longyearbyen, was simulated, and finally, climate projections for the service lifetime of the building were incorporated to estimate the effects of climate change for this project.

The 3D model is a thermal model purely accounting for conductive heat transfer. The cooling pipes were simulated by a constant surface temperature. This is due to the fact that

no information about the heat pump, cooling fluid and temperatures were available and also that the pipe layout is so dense, that a homogenous cooling of the ground was assumed to simplify the model. The model was verified using measured ground temperature data, however soil properties were not known and were estimated by an iterative calibration process. The accuracy of the model was quantified by comparing modelled and recorded temperature from October 2019 to December 2020.

The results are given in chapter 6 for each respective scenario. In the following, the results are summarized and discussed jointly, before this chapter closes with recommendations for further work in this field of research.

7.1 Discussion

The results studying the suitability of a cooling temperature of -5 and -10 °C respectively, show that the corner areas close to the ocean is most critical with the warmest ground temperature. Thus, a cooling temperature must be chosen in respect to ground temperature at the edge area of the plate. P6 lies within the warmest area of the plate and should be the focus point to define a suitable cooling temperature. The temperature at P6 goes up to -2.3 °C at a cooling temperature of -5 °C. The analysis was conducted under climatic conditions representing average temperature values for 2019 and 2020, the mean annual ground surface temperature equals -2.7 °C. The vicinity of the ocean makes a high salinity very probable and can lead to a significant freezing point depression which was not accounted for in this study. The ground can already experience weakening at temperatures approaching the freezing point and is very sensible to any further temperature changes. A cooling temperature of -10 °C results in a maximum temperature of -4.5 °C in the warmest area under the plate. This indicates that a temperature of -10 °C is more suitable as it leaves a larger safety margin especially in light of climate warming.

A comparison between the annual operational costs for the respective cooling temperature, show that the operational cost increases up to 20 000 NOK for a decrease in cooling form -5 to -10 °C. This also indicates that the choice of a suitable temperature is directly related to the cost efficiency of the technology. In cases, where the extracted heat is reused, the operational cost can be compensated for by the reusable heat from the system. The work that needs to be put in to run the system can be reused for direct heating or storage. Therefore a sustainable operation of this technology should focus on reusing the extracted heat and the input energy.

The consequences of power failure and a shut down of the cooling system are that ground temperatures under the plate warm as much as 4 °C in one year. Therefore, a well-controlled monitoring system should be an integral part of this technology to avoid undetected power failure.

The study of seasonal operation shows that the ground remains frozen also when the cooling system is turned off for three consecutive months in winter. This implies that the system can be turned off in the darker seasons and powered with solar energy in warmer seasons. Which consequently highlights the development possibility to a self-sustained cooling system, which can be coupled with a renewable energy source, such as solar energy, to power the system. This shows an interesting opportunity to develop the technology into a sustainable off-grid solution where electricity can be produced by harvesting solar energy in summer. However, more detailed analyses are necessary to study the most suitable cooling/no-cooling interval and its effects on the ground thermal regime. This is currently the focus of an EU funded project in Longyearbyen which aims to develop an off-grid heat-pump cooling system.

The studied projected climate warming scenario RCP8.5 for the service lifetime of the building shows that the ground thermal regime adjacent to the house will remain frozen, but ground temperatures are increasing, especially in winter. That the ground remains frozen indicates that the cooling system is a suitable solution in view of stability of the structure for the entire service lifetime. However, a cooling temperature of -5 °C leads to temperatures above -1 °C. Thus, in presence of climate warming, a cooling temperature of -5 °C becomes problematic. The ground can ultimately lose its strength when approaching the freezing point temperature of the pore water. This can lead to differential settlements as the foundation is not rigid and the building can settle at different rates which subsequently can result in cracks and risks for the structural integrity of the building.

It is important to note that results from the simulations need to be interpreted with the accuracy discussed in the validation and calibration process. The model predominantly produced colder ground temperatures. It is advised to use the results with an accuracy of ±1 °C for decision-making. In conclusion, this means that, when identifying areas of critical ground temperatures, a conservative approach is achieved by adding +1 °C to the computed temperatures presented above. Especially in view of climate change, at a cooling temperature of -5 °C, this results in very critical ground temperatures above 0 °C under the plate.

7.2 Recommendations for Further Work

This study has shown that the heat-pump cooling technology is an attractive engineering solution for permafrost regions. The system also shows to be a suitable solution in light of climate change and further research can open up the potential for an off-grid cooling solution for remote permafrost regions.

For future studies, the perspective of a seasonally operated heat-pump, coupled with solar energy to power the system, is a relevant field of research. This development then addresses the challenges of climate warming in two ways: permafrost warming is mitigated and the production of greenhouse gases is eliminated. Additionally, the technology can be an attractive solution for remote off-grid permafrost regions.

In a future optimization perspective, it is of interest to simulate the foundation design in more detail to identify governing parameters. For this purpose, the pipe layout, the heat carrier fluid properties, its velocity as well as inlet and outlet temperature are some of the parameters, which can be incorporated in numerical simulations. A detailed simulation of the cooling pipe layout, cooling fluid properties and temperatures accounts for convective heat flow caused by the moving fluid in the pipe and the temperature gradient between fluid and ground. This allows to define suitable cooling inflow temperature and generated outflow temperature to estimate the heat pump's efficiency in more detail. Also, it allows to study the effect of the pipe layout in terms of the spatial distribution of the cooling for the foundation area. In other words, whether the ground cooling is achieved homogeneously for the chosen pipe layout and whether the layout can be optimized. Additionally, a study of varying insulation thickness under the heated building can minimize the heat loss from the building and can help to optimize the cooling system.

In general, the development of a widely accepted design method for heat-pump cooling systems on permafrost can aid to achieve a sustainable and reliable application of the system.

Appendix A

Acronyms

ALT Active Layer Thickness

AT Air Temperature

DZAA Depth of Zero Annual Amplitude

FEM Finite Element Method

GSHP Ground Source Heat Pump

GST Ground Surface Temperature

GT Ground Temperature

HCF Heat Carrier Fluid

MAAT Mean Annual Air Temperature

MAGST Mean Annual Ground Surface Temperature

MAGT Mean Annual Ground Temperature

MMGT Mean Monthly Ground Temperature

PDE Partial Differential Equation

REV Representative Elementary Volume

RMSE Root Mean Squared Error

RCP Representative Concentration Pathway

SEB Surface Energy Balance

TTOP Temperature Top Of Permafrost

ZAA Zero Annual Amplitude

Appendix B

Additional Information

B.1 Thermal Properties from Literature

Table B.1: Selected thermal properties from literature shows a wide variation of thermal properties.

Material	Density kg/m³	Thermal Conductivity [W/(m.K)]	Specific Heat Capacity [kJ/(kg.K)]	Volumetric Heat Capacity [MJ/(m³.K)]	Source
Air	1.25	0.026	1.00	0.00	(Andersland and Ladanyi, 2004)
Water	999.87	0.56	4.19	4.19	(Andersland and Ladanyi, 2004)
Ice at 0°C	900	2.21	2.09	1.88	(Andersland and Ladanyi, 2004)
Snow loose	85	0.08	2.09	0.18	(Andersland and Ladanyi, 2004)
Snow dense	500	0.7	2.09	1.05	(Andersland and Ladanyi, 2004)
Polystyrene, foam	30	0.035	1.25	0.04	(Andersland and Ladanyi, 2004)
BEWI XPS	-	0.036	-	-	(BEWI, nd)
Concrete	2200	1.3 - 1.7	0.90	1.97	(French, 2007)
Concrete	2100	1.5	-	-	(Goodrich and Plunkett, 1990)
Concrete	2500	1.7	0.67	1.68	(Smith, 1996)
Sandy soil, dry	1600	0.3	0.80	1.28	(Williams and Smith, 1989)
Sandy soil, sat	2000	2.2	1.48	2.96	(Williams and Smith, 1989)
Gravel, dry	1800	0.4-0.9	0.85	1.53	(VDI, 2019)
Silty Soil	1200	0.96	-	-	(Goodrich and Plunkett, 1990)
Sand, dry	2000	1.1	0.8	1.60	(Smith, 1996)
Sand, thawed, sat	2000	3.2	1.21	2.42	(Smith, 1996)
Sand, frozen, sat	2000	4.1	0.88	1.76	(Smith, 1996)
Clay, dry	1700	0.9	0.92	1.56	(Smith, 1996)
Clay, thawed, sat	1700	1.6	1.76	2.99	(Smith, 1996)
Clay, frozen, sat	1700	2.1	1.34	2.28	(Smith, 1996)

B.2 Construction Drawings

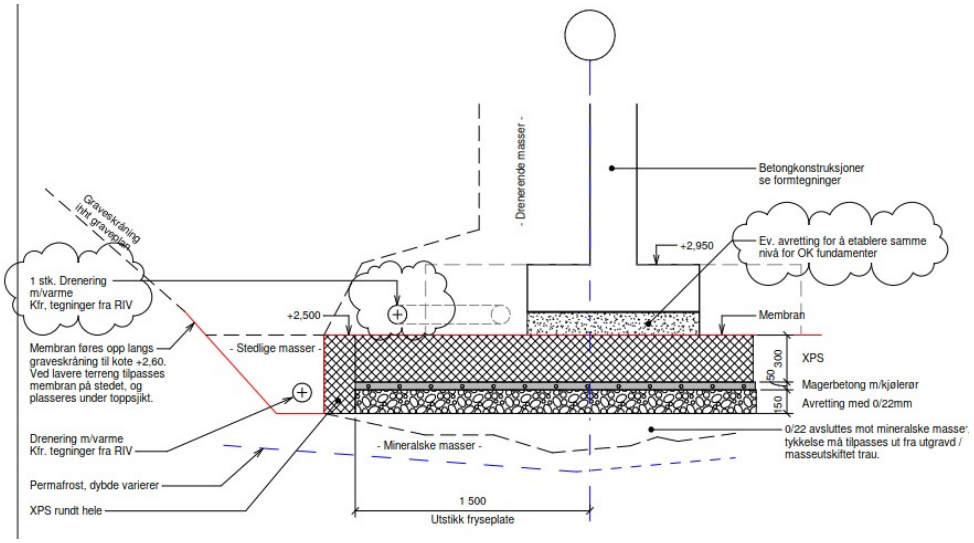

Figure B.1: Foundation design (retrieved online from the Interaxo project database with permission from Braun, R.-H.).

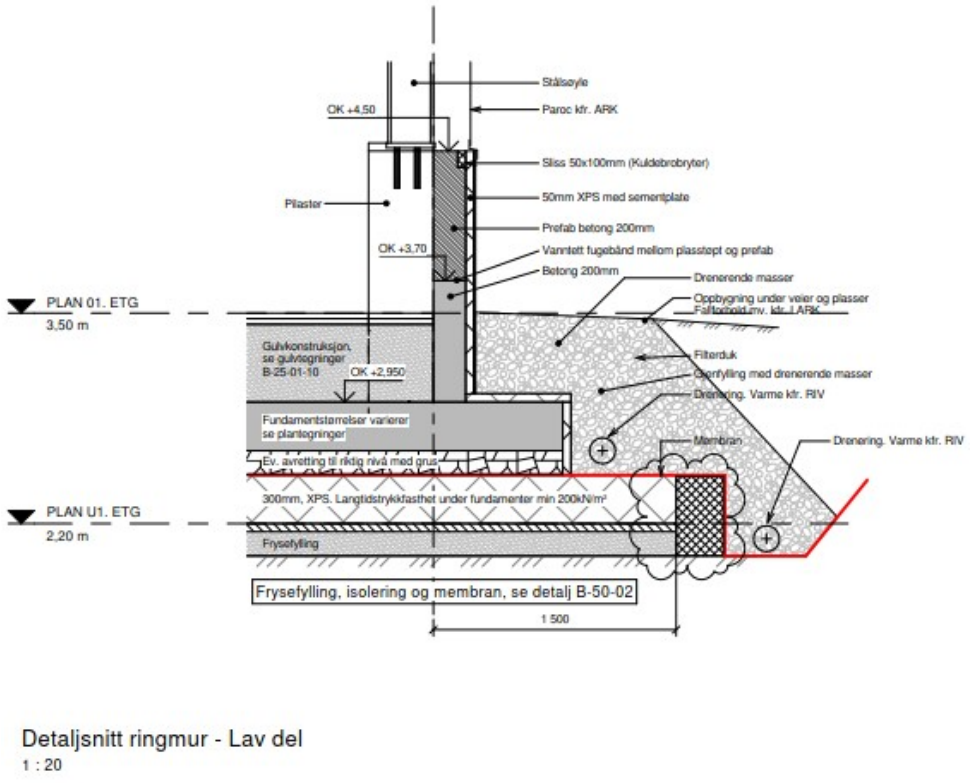

Figure B.2: Foundation design (retrieved online from the Interaxo project database with permission from Braun, R.-H.).

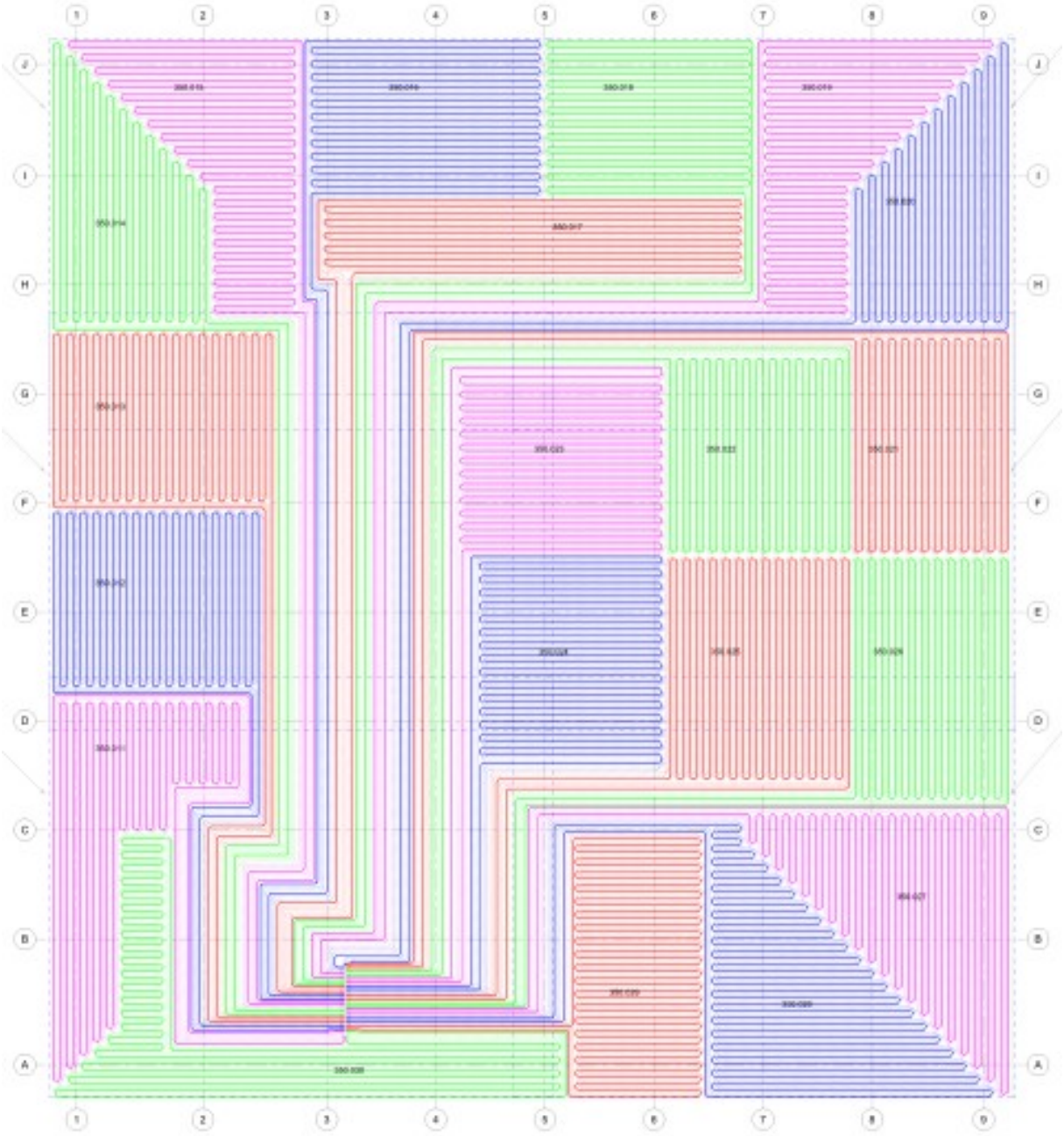

Figure B.3: Cooling pipe layout in the foundation design (retrieved online from the Interaxo project database with permission from Braun, R.-H.).

B.3 Calibration of Soil Properties

The calculation results for parameter set v08 is presented in a tabular manner in Table B.2.

Table B.2: Thermal properties for soil parameter set v08. Temperature is given in positive values below freezing point of 0 °C.

Temperature [°C]	W_u [%]	Θ_u [-]	Φ [-]	k_eff [W/(m.°C)]	k_{eff} [](kJ/sec)/(m.°C)]
0.00	100.00	1.00	1.00	1.43	0.00143
0.01	25.54	0.52	1.00	1.43	0.00143
0.01	24.65	0.50	1.00	1.43	0.00143
0.01	23.89	0.49	1.00	1.43	0.00143
0.05	14.74	0.30	1.00	1.43	0.00143
0.10	11.97	0.24	1.00	1.43	0.00143
0.20	9.72	0.20	0.86	1.50	0.00150
0.30	8.61	0.18	0.76	1.55	0.00155
0.40	7.90	0.16	0.70	1.58	0.00158
0.50	7.39	0.15	0.66	1.60	0.00160
1.00	6.00	0.12	0.53	1.66	0.00166
1.50	5.31	0.11	0.47	1.70	0.00170
2.00	4.87	0.10	0.43	1.72	0.00172
2.50	4.56	0.09	0.40	1.73	0.00173
3.00	4.32	0.09	0.38	1.74	0.00174
3.50	4.12	0.08	0.37	1.75	0.00175
4.00	3.96	0.08	0.35	1.76	0.00176
4.50	3.82	0.08	0.34	1.77	0.00177
5.00	3.70	0.08	0.33	1.77	0.00177
5.50	3.60	0.07	0.32	1.78	0.00178
6.00	3.51	0.07	0.31	1.78	0.00178
6.50	3.42	0.07	0.30	1.79	0.00179
7.00	3.35	0.07	0.30	1.79	0.00179
7.50	3.28	0.07	0.29	1.79	0.00179
8.00	3.22	0.07	0.29	1.80	0.00180
8.50	3.16	0.06	0.28	1.80	0.00180

9.00	3.10	0.06	0.28	1.80	0.00180
9.50	3.05	0.06	0.27	1.81	0.00181
10.00	3.01	0.06	0.27	1.81	0.00181
10.50	2.96	0.06	0.26	1.81	0.00181
11.00	2.92	0.06	0.26	1.81	0.00181
11.50	2.88	0.06	0.26	1.81	0.00181
12.00	2.85	0.06	0.25	1.82	0.00182
12.50	2.81	0.06	0.25	1.82	0.00182
13.00	2.78	0.06	0.25	1.82	0.00182
13.50	2.75	0.06	0.24	1.82	0.00182
14.00	2.72	0.06	0.24	1.82	0.00182
14.50	2.69	0.05	0.24	1.82	0.00182
15.00	2.66	0.05	0.24	1.83	0.00183
15.50	2.64	0.05	0.23	1.83	0.00183
16.00	2.61	0.05	0.23	1.83	0.00183
16.50	2.59	0.05	0.23	1.83	0.00183
17.00	2.56	0.05	0.23	1.83	0.00183
17.50	2.54	0.05	0.23	1.83	0.00183
18.00	2.52	0.05	0.22	1.83	0.00183
18.50	2.50	0.05	0.22	1.83	0.00183
19.00	2.48	0.05	0.22	1.84	0.00184
19.50	2.46	0.05	0.22	1.84	0.00184
20.00	2.44	0.05	0.22	1.84	0.00184

B.4 Thermal Model Days

Time slices of elapsed time and its corresponding date in the simulation process:

Table B.3: List of days used for the thermal modelling (1/6).

Date	Elapsed Time	Date	Elapsed Time	Date	Elapsed Time
01/10/2019	2099	01/01/2023	3286	01/04/2026	4471
01/11/2019	2130	01/02/2023	3317	01/05/2026	4501
01/12/2019	2160	01/03/2023	3345	01/06/2026	4532
01/01/2020	2191	01/04/2023	3376	01/07/2026	4562
01/02/2020	2222	01/05/2023	3406	01/08/2026	4593
01/03/2020	2250	01/06/2023	3437	01/09/2026	4624
01/04/2020	2281	01/07/2023	3467	01/10/2026	4654
01/05/2020	2311	01/08/2023	3498	01/11/2026	4685
01/06/2020	2342	01/09/2023	3529	01/12/2026	4715
01/07/2020	2372	01/10/2023	3559	01/01/2027	4746
01/08/2020	2403	01/11/2023	3590	01/02/2027	4777
01/09/2020	2434	01/12/2023	3620	01/03/2027	4805
01/10/2020	2464	01/01/2024	3651	01/04/2027	4836
01/11/2020	2495	01/02/2024	3682	01/05/2027	4866
01/12/2020	2525	01/03/2024	3710	01/06/2027	4897
01/01/2021	2556	01/04/2024	3741	01/07/2027	4927
01/02/2021	2587	01/05/2024	3771	01/08/2027	4958
01/03/2021	2615	01/06/2024	3802	01/09/2027	4989
01/04/2021	2646	01/07/2024	3832	01/10/2027	5019
01/05/2021	2676	01/08/2024	3863	01/11/2027	5050
01/06/2021	2707	01/09/2024	3894	01/12/2027	5080
01/07/2021	2737	01/10/2024	3924	01/01/2028	5111
01/08/2021	2768	01/11/2024	3955	01/02/2028	5142
01/09/2021	2799	01/12/2024	3985	01/03/2028	5170
01/10/2021	2829	01/01/2025	4016	01/04/2028	5201
01/11/2021	2860	01/02/2025	4047	01/05/2028	5231
01/12/2021	2890	01/03/2025	4075	01/06/2028	5262
01/01/2022	2921	01/04/2025	4106	01/07/2028	5292
01/02/2022	2952	01/05/2025	4136	01/08/2028	5323
01/03/2022	2980	01/06/2025	4167	01/09/2028	5354
01/04/2022	3011	01/07/2025	4197	01/10/2028	5384
01/05/2022	3041	01/08/2025	4228	01/11/2028	5415
01/06/2022	3072	01/09/2025	4259	01/12/2028	5445
01/07/2022	3102	01/10/2025	4289	01/01/2029	5476
01/08/2022	3133	01/11/2025	4320	01/02/2029	5507
01/09/2022	3164	01/12/2025	4350	01/03/2029	5535
01/10/2022	3194	01/01/2026	4381	01/04/2029	5566
01/11/2022	3225	01/02/2026	4412	01/05/2029	5596
01/12/2022	3255	01/03/2026	4440	01/06/2029	5627

Table B.4: List of days used for the thermal modelling (2/6).

Date	Elapsed Time	Date	Elapsed Time	Date	Elapsed Time
01/07/2029	5657	01/10/2032	6844	01/01/2036	8031
01/08/2029	5688	01/11/2032	6875	01/02/2036	8062
01/09/2029	5719	01/12/2032	6905	01/03/2036	8090
01/10/2029	5749	01/01/2033	6936	01/04/2036	8121
01/11/2029	5780	01/02/2033	6967	01/05/2036	8151
01/12/2029	5810	01/03/2033	6995	01/06/2036	8182
01/01/2030	5841	01/04/2033	7026	01/07/2036	8212
01/02/2030	5872	01/05/2033	7056	01/08/2036	8243
01/03/2030	5900	01/06/2033	7087	01/09/2036	8274
01/04/2030	5931	01/07/2033	7117	01/10/2036	8304
01/05/2030	5961	01/08/2033	7148	01/11/2036	8335
01/06/2030	5992	01/09/2033	7179	01/12/2036	8365
01/07/2030	6022	01/10/2033	7209	01/01/2037	8396
01/08/2030	6053	01/11/2033	7240	01/02/2037	8427
01/09/2030	6084	01/12/2033	7270	01/03/2037	8455
01/10/2030	6114	01/01/2034	7301	01/04/2037	8486
01/11/2030	6145	01/02/2034	7332	01/05/2037	8516
01/12/2030	6175	01/03/2034	7360	01/06/2037	8547
01/01/2031	6206	01/04/2034	7391	01/07/2037	8577
01/02/2031	6237	01/05/2034	7421	01/08/2037	8608
01/03/2031	6265	01/06/2034	7452	01/09/2037	8639
01/04/2031	6296	01/07/2034	7482	01/10/2037	8669
01/05/2031	6326	01/08/2034	7513	01/11/2037	8700
01/06/2031	6357	01/09/2034	7544	01/12/2037	8730
01/07/2031	6387	01/10/2034	7574	01/01/2038	8761
01/08/2031	6418	01/11/2034	7605	01/02/2038	8792
01/09/2031	6449	01/12/2034	7635	01/03/2038	8820
01/10/2031	6479	01/01/2035	7666	01/04/2038	8851
01/11/2031	6510	01/02/2035	7697	01/05/2038	8881
01/12/2031	6540	01/03/2035	7725	01/06/2038	8912
01/01/2032	6571	01/04/2035	7756	01/07/2038	8942
01/02/2032	6602	01/05/2035	7786	01/08/2038	8973
01/03/2032	6630	01/06/2035	7817	01/09/2038	9004
01/04/2032	6661	01/07/2035	7847	01/10/2038	9034
01/05/2032	6691	01/08/2035	7878	01/11/2038	9065
01/06/2032	6722	01/09/2035	7909	01/12/2038	9095
01/07/2032	6752	01/10/2035	7939	01/01/2039	9126
01/08/2032	6783	01/11/2035	7970	01/02/2039	9157
01/09/2032	6814	01/12/2035	8000	01/03/2039	9185

Table B.5: List of days used for the thermal modelling (3/6).

Date	Elapsed Time	Date	Elapsed Time	Date	Elapsed Time
01/04/2039	9216	01/07/2042	10402	01/10/2045	11589
01/05/2039	9246	01/08/2042	10433	01/11/2045	11620
01/06/2039	9277	01/09/2042	10464	01/12/2045	11650
01/07/2039	9307	01/10/2042	10494	01/01/2046	11681
01/08/2039	9338	01/11/2042	10525	01/02/2046	11712
01/09/2039	9369	01/12/2042	10555	01/03/2046	11740
01/10/2039	9399	01/01/2043	10586	01/04/2046	11771
01/11/2039	9430	01/02/2043	10617	01/05/2046	11801
01/12/2039	9460	01/03/2043	10645	01/06/2046	11832
01/01/2040	9491	01/04/2043	10676	01/07/2046	11862
01/02/2040	9522	01/05/2043	10706	01/08/2046	11893
01/03/2040	9550	01/06/2043	10737	01/09/2046	11924
01/04/2040	9581	01/07/2043	10767	01/10/2046	11954
01/05/2040	9611	01/08/2043	10798	01/11/2046	11985
01/06/2040	9642	01/09/2043	10829	01/12/2046	12015
01/07/2040	9672	01/10/2043	10859	01/01/2047	12046
01/08/2040	9703	01/11/2043	10890	01/02/2047	12077
01/09/2040	9734	01/12/2043	10920	01/03/2047	12105
01/10/2040	9764	01/01/2044	10951	01/04/2047	12136
01/11/2040	9795	01/02/2044	10982	01/05/2047	12166
01/12/2040	9825	01/03/2044	11010	01/06/2047	12197
01/01/2041	9856	01/04/2044	11041	01/07/2047	12227
01/02/2041	9887	01/05/2044	11071	01/08/2047	12258
01/03/2041	9915	01/06/2044	11102	01/09/2047	12289
01/04/2041	9946	01/07/2044	11132	01/10/2047	12319
01/05/2041	9976	01/08/2044	11163	01/11/2047	12350
01/06/2041	10007	01/09/2044	11194	01/12/2047	12380
01/07/2041	10037	01/10/2044	11224	01/01/2048	12411
01/08/2041	10068	01/11/2044	11255	01/02/2048	12442
01/09/2041	10099	01/12/2044	11285	01/03/2048	12470
01/10/2041	10129	01/01/2045	11316	01/04/2048	12501
01/11/2041	10160	01/02/2045	11347	01/05/2048	12531
01/12/2041	10190	01/03/2045	11375	01/06/2048	12562
01/01/2042	10221	01/04/2045	11406	01/07/2048	12592
01/02/2042	10252	01/05/2045	11436	01/08/2048	12623
01/03/2042	10280	01/06/2045	11467	01/09/2048	12654
01/04/2042	10311	01/07/2045	11497	01/10/2048	12684
01/05/2042	10341	01/08/2045	11528	01/11/2048	12715
01/06/2042	10372	01/09/2045	11559	01/12/2048	12745

Table B.6: List of days used for the thermal modelling (4/6).

Date	Elapsed Time	Date	Elapsed Time	Date	Elapsed Time
01/01/2049	12776	01/04/2052	13961	01/07/2055	15147
01/02/2049	12807	01/05/2052	13991	01/08/2055	15178
01/03/2049	12835	01/06/2052	14022	01/09/2055	15209
01/04/2049	12866	01/07/2052	14052	01/10/2055	15239
01/05/2049	12896	01/08/2052	14083	01/11/2055	15270
01/06/2049	12927	01/09/2052	14114	01/12/2055	15300
01/07/2049	12957	01/10/2052	14144	01/01/2056	15331
01/08/2049	12988	01/11/2052	14175	01/02/2056	15362
01/09/2049	13019	01/12/2052	14205	01/03/2056	15390
01/10/2049	13049	01/01/2053	14236	01/04/2056	15421
01/11/2049	13080	01/02/2053	14267	01/05/2056	15451
01/12/2049	13110	01/03/2053	14295	01/06/2056	15482
01/01/2050	13141	01/04/2053	14326	01/07/2056	15512
01/02/2050	13172	01/05/2053	14356	01/08/2056	15543
01/03/2050	13200	01/06/2053	14387	01/09/2056	15574
01/04/2050	13231	01/07/2053	14417	01/10/2056	15604
01/05/2050	13261	01/08/2053	14448	01/11/2056	15635
01/06/2050	13292	01/09/2053	14479	01/12/2056	15665
01/07/2050	13322	01/10/2053	14509	01/01/2057	15696
01/08/2050	13353	01/11/2053	14540	01/02/2057	15727
01/09/2050	13384	01/12/2053	14570	01/03/2057	15755
01/10/2050	13414	01/01/2054	14601	01/04/2057	15786
01/11/2050	13445	01/02/2054	14632	01/05/2057	15816
01/12/2050	13475	01/03/2054	14660	01/06/2057	15847
01/01/2051	13506	01/04/2054	14691	01/07/2057	15877
01/02/2051	13537	01/05/2054	14721	01/08/2057	15908
01/03/2051	13565	01/06/2054	14752	01/09/2057	15939
01/04/2051	13596	01/07/2054	14782	01/10/2057	15969
01/05/2051	13626	01/08/2054	14813	01/11/2057	16000
01/06/2051	13657	01/09/2054	14844	01/12/2057	16030
01/07/2051	13687	01/10/2054	14874	01/01/2058	16061
01/08/2051	13718	01/11/2054	14905	01/02/2058	16092
01/09/2051	13749	01/12/2054	14935	01/03/2058	16120
01/10/2051	13779	01/01/2055	14966	01/04/2058	16151
01/11/2051	13810	01/02/2055	14997	01/05/2058	16181
01/12/2051	13840	01/03/2055	15025	01/06/2058	16212
01/01/2052	13871	01/04/2055	15056	01/07/2058	16242
01/02/2052	13902	01/05/2055	15086	01/08/2058	16273
01/03/2052	13930	01/06/2055	15117	01/09/2058	16304

Table B.7: List of days used for the thermal modelling (5/6).

Date	Elapsed Time	Date	Elapsed Time	Date	Elapsed Time
01/10/2058	16334	01/01/2062	17521	01/04/2065	18706
01/11/2058	16365	01/02/2062	17552	01/05/2065	18736
01/12/2058	16395	01/03/2062	17580	01/06/2065	18767
01/01/2059	16426	01/04/2062	17611	01/07/2065	18797
01/02/2059	16457	01/05/2062	17641	01/08/2065	18828
01/03/2059	16485	01/06/2062	17672	01/09/2065	18859
01/04/2059	16516	01/07/2062	17702	01/10/2065	18889
01/05/2059	16546	01/08/2062	17733	01/11/2065	18920
01/06/2059	16577	01/09/2062	17764	01/12/2065	18950
01/07/2059	16607	01/10/2062	17794	01/01/2066	18981
01/08/2059	16638	01/11/2062	17825	01/02/2066	19012
01/09/2059	16669	01/12/2062	17855	01/03/2066	19040
01/10/2059	16699	01/01/2063	17886	01/04/2066	19071
01/11/2059	16730	01/02/2063	17917	01/05/2066	19101
01/12/2059	16760	01/03/2063	17945	01/06/2066	19132
01/01/2060	16791	01/04/2063	17976	01/07/2066	19162
01/02/2060	16822	01/05/2063	18006	01/08/2066	19193
01/03/2060	16850	01/06/2063	18037	01/09/2066	19224
01/04/2060	16881	01/07/2063	18067	01/10/2066	19254
01/05/2060	16911	01/08/2063	18098	01/11/2066	19285
01/06/2060	16942	01/09/2063	18129	01/12/2066	19315
01/07/2060	16972	01/10/2063	18159	01/01/2067	19346
01/08/2060	17003	01/11/2063	18190	01/02/2067	19377
01/09/2060	17034	01/12/2063	18220	01/03/2067	19405
01/10/2060	17064	01/01/2064	18251	01/04/2067	19436
01/11/2060	17095	01/02/2064	18282	01/05/2067	19466
01/12/2060	17125	01/03/2064	18310	01/06/2067	19497
01/01/2061	17156	01/04/2064	18341	01/07/2067	19527
01/02/2061	17187	01/05/2064	18371	01/08/2067	19558
01/03/2061	17215	01/06/2064	18402	01/09/2067	19589
01/04/2061	17246	01/07/2064	18432	01/10/2067	19619
01/05/2061	17276	01/08/2064	18463	01/11/2067	19650
01/06/2061	17307	01/09/2064	18494	01/12/2067	19680
01/07/2061	17337	01/10/2064	18524	01/01/2068	19711
01/08/2061	17368	01/11/2064	18555	01/02/2068	19742
01/09/2061	17399	01/12/2064	18585	01/03/2068	19770
01/10/2061	17429	01/01/2065	18616	01/04/2068	19801
01/11/2061	17460	01/02/2065	18647	01/05/2068	19831
01/12/2061	17490	01/03/2065	18675	01/06/2068	19862

Table B.8: List of days used for the thermal modelling (6/6).

Date	Elapsed Time	Date	Elapsed Time
01/07/2068	19892	01/10/2071	21079
01/08/2068	19923	01/11/2071	21110
01/09/2068	19954	01/12/2071	21140
01/10/2068	19984	01/01/2072	21171
01/11/2068	20015	01/02/2072	21202
01/12/2068	20045	01/03/2072	21230
01/01/2069	20076	01/04/2072	21261
01/02/2069	20107	01/05/2072	21291
01/03/2069	20135	01/06/2072	21322
01/04/2069	20166	01/07/2072	21352
01/05/2069	20196	01/08/2072	21383
01/06/2069	20227	01/09/2072	21414
01/07/2069	20257	01/10/2072	21444
01/08/2069	20288	01/11/2072	21475
01/09/2069	20319	01/12/2072	21505
01/10/2069	20349	01/01/2073	21535
01/11/2069	20380		
01/12/2069	20410		
01/01/2070	20441		
01/02/2070	20472		
01/03/2070	20500		
01/04/2070	20531		
01/05/2070	20561		
01/06/2070	20592		
01/07/2070	20622		
01/08/2070	20653		
01/09/2070	20684		
01/10/2070	20714		
01/11/2070	20745		
01/12/2070	20775		
01/01/2071	20806		
01/02/2071	20837		
01/03/2071	20865		
01/04/2071	20896		
01/05/2071	20926		
01/06/2071	20957		
01/07/2071	20987		
01/08/2071	21018		
01/09/2071	21049		

B.5 Model Performance in the Upper 5 Metres

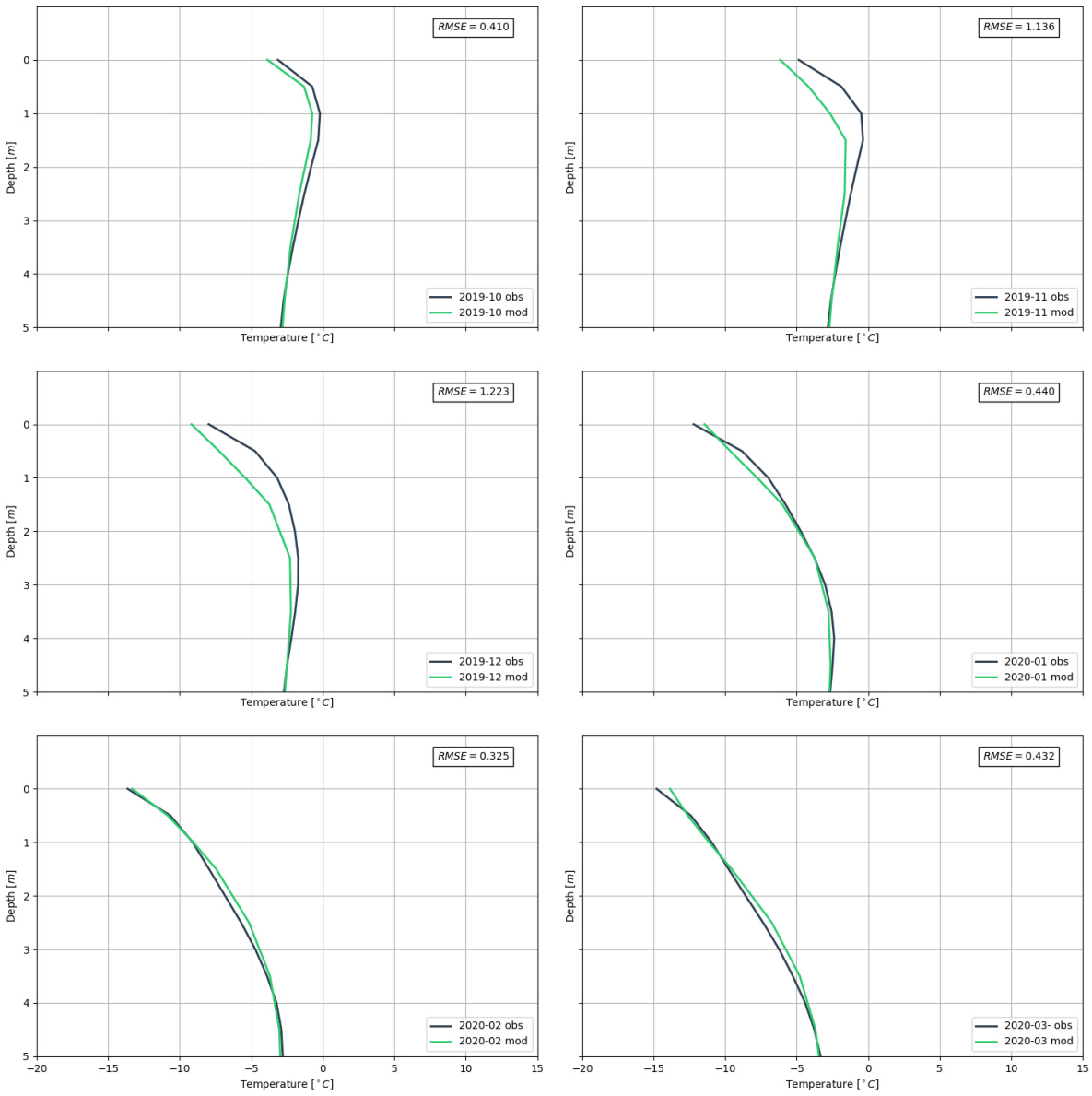

Figure B.4: Modelled versus recorded ground temperature for the upper 5 metres in H2 (Oct 19 - Mar 20).

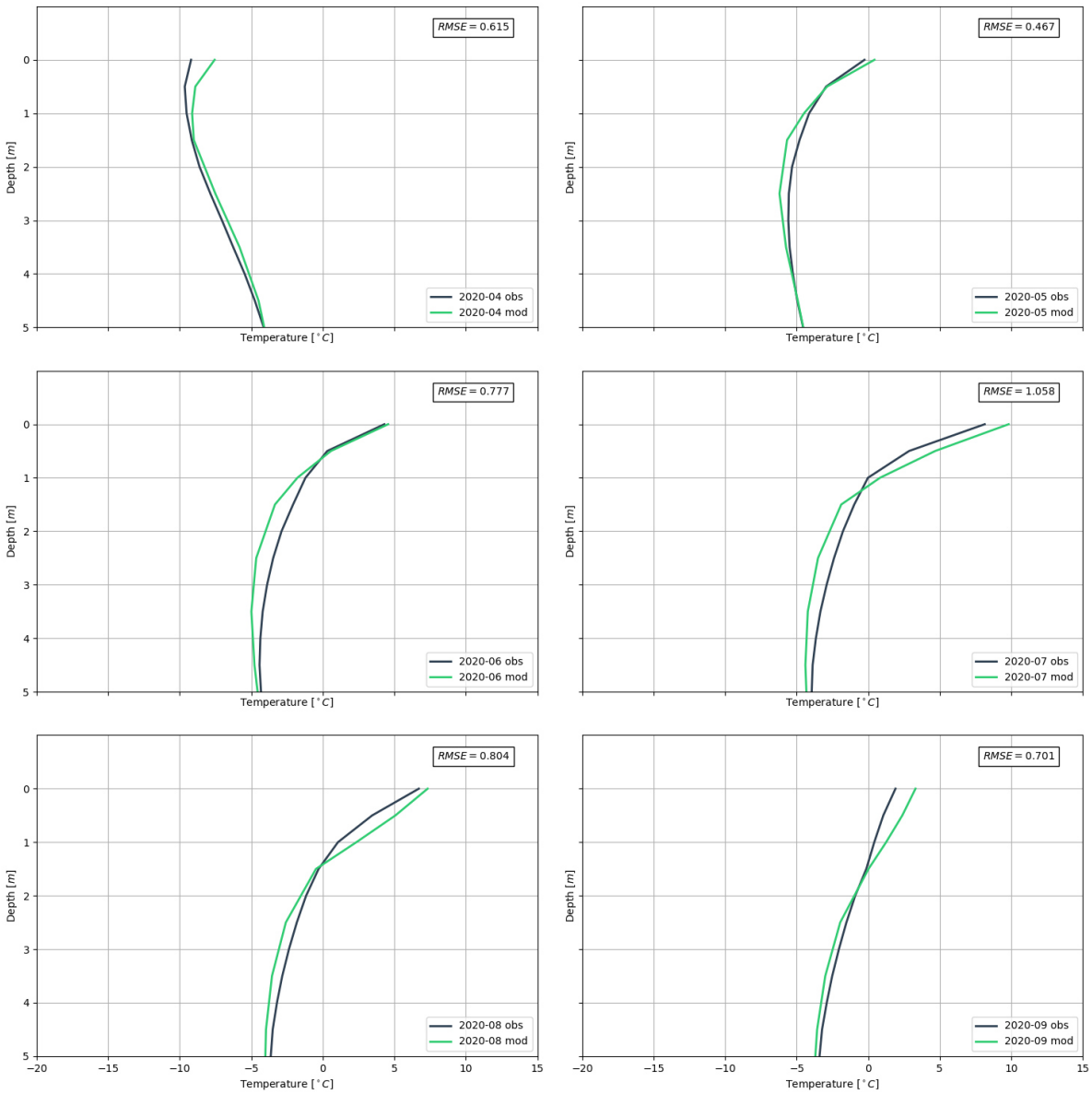

Figure B.5: Modelled versus recorded ground temperature for the upper 5 metres in H2 (Apr 20 - Sep 20).

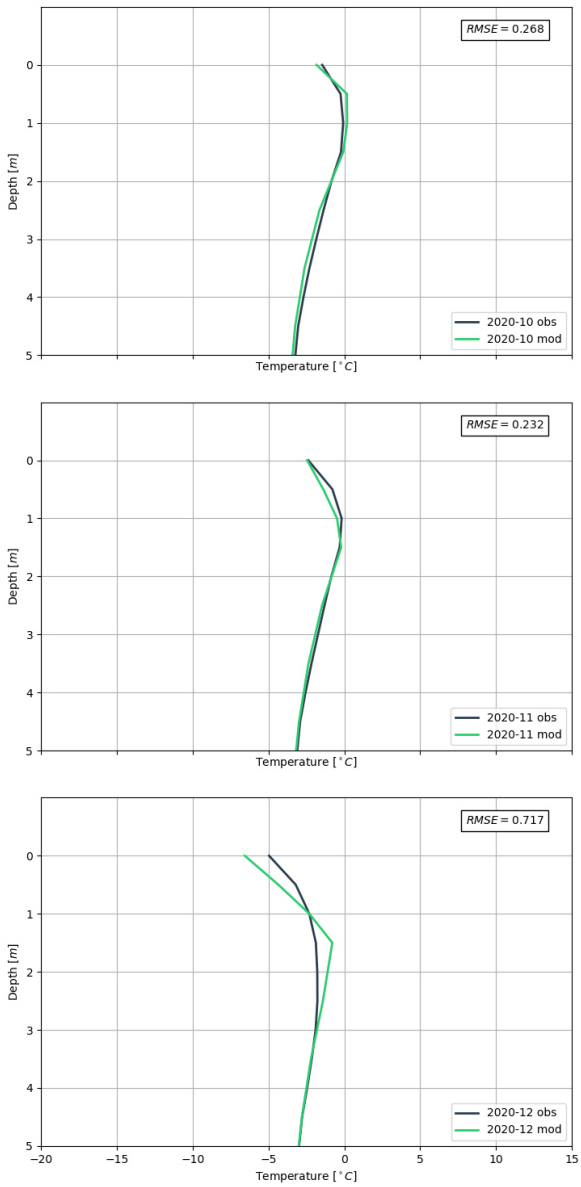

Figure B.6: Modelled versus recorded ground temperature for the upper 5 metres in H2 (Oct 20 - Dec 20).

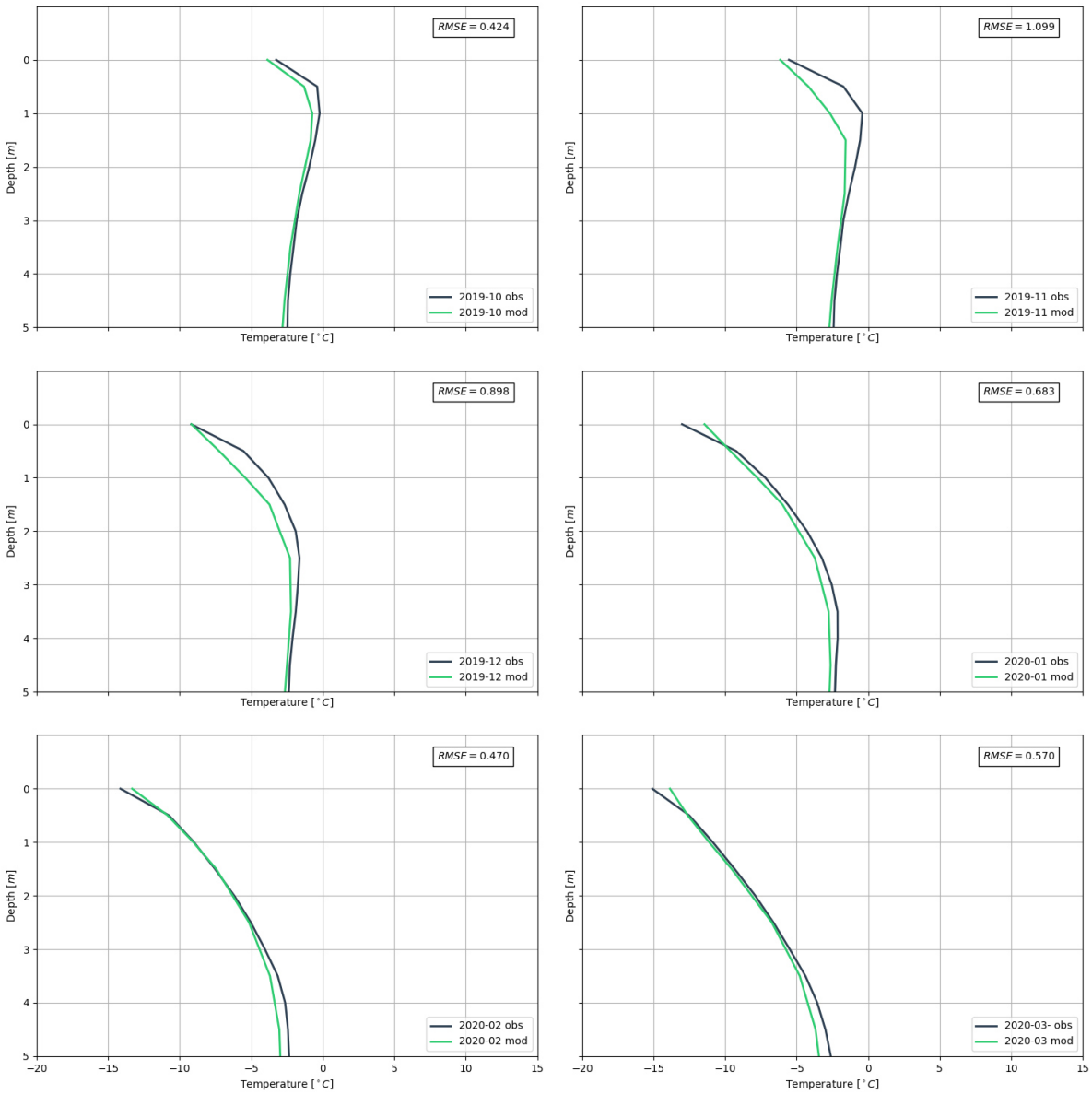

Figure B.7: Modelled versus recorded ground temperature for the upper 5 metres in H1 (Oct 19 - Mar 20).

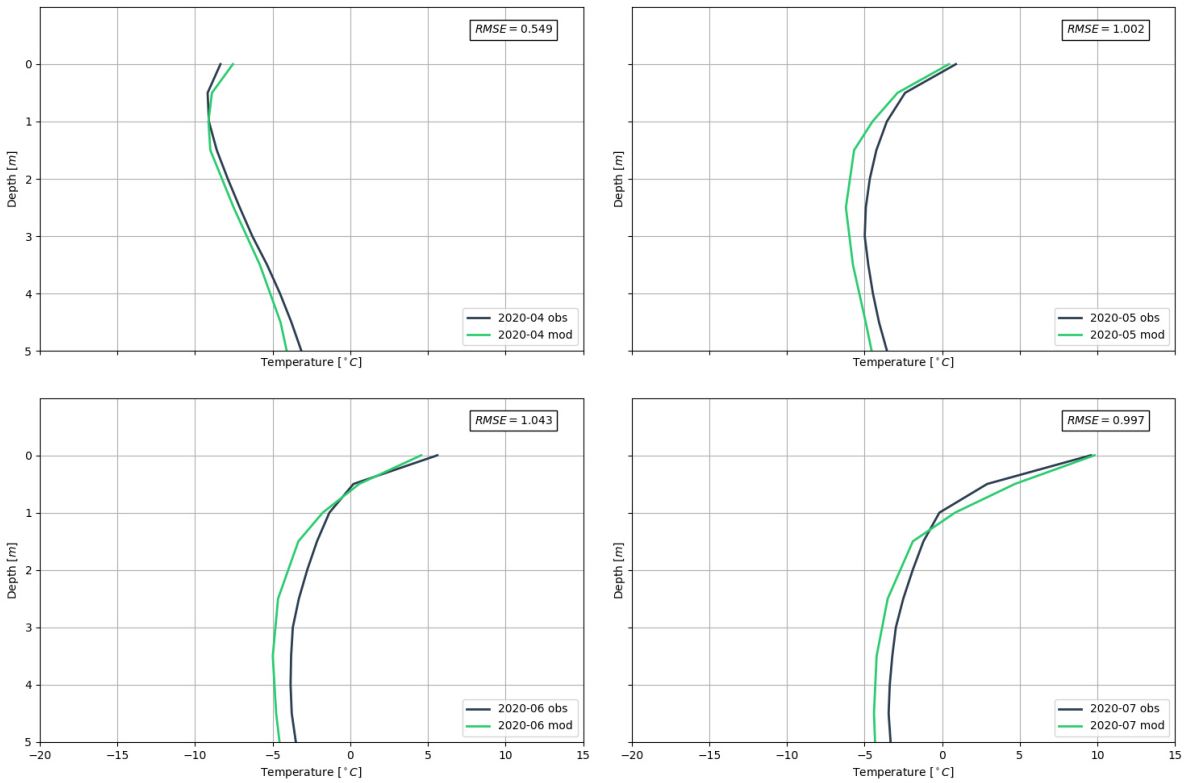

Figure B.8: Modelled versus recorded ground temperature for the upper 5 metres in H2 (Apr 20 - Jul 20).

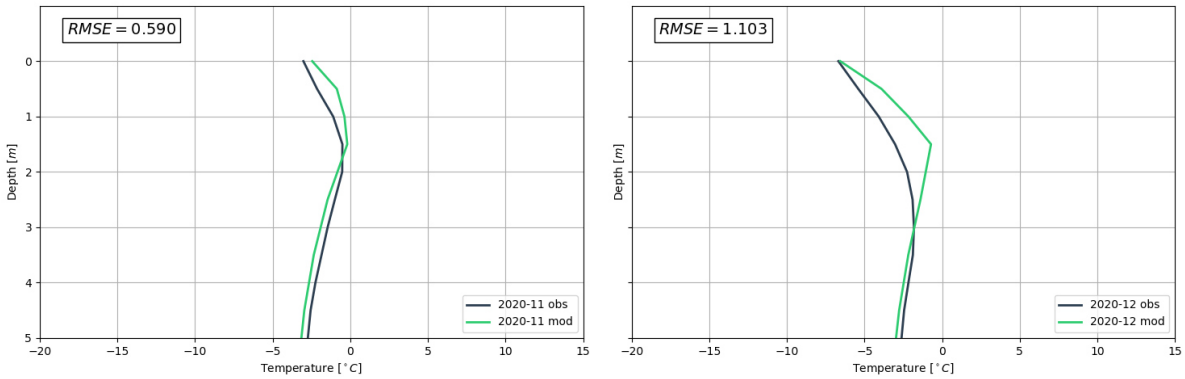

Figure B.9: Modelled versus recorded ground temperature for the upper 5 metres in H4 (Nov 20 - Dec 20).

B.6 Temperature Regime for a Cooling Temperature of -5 °C

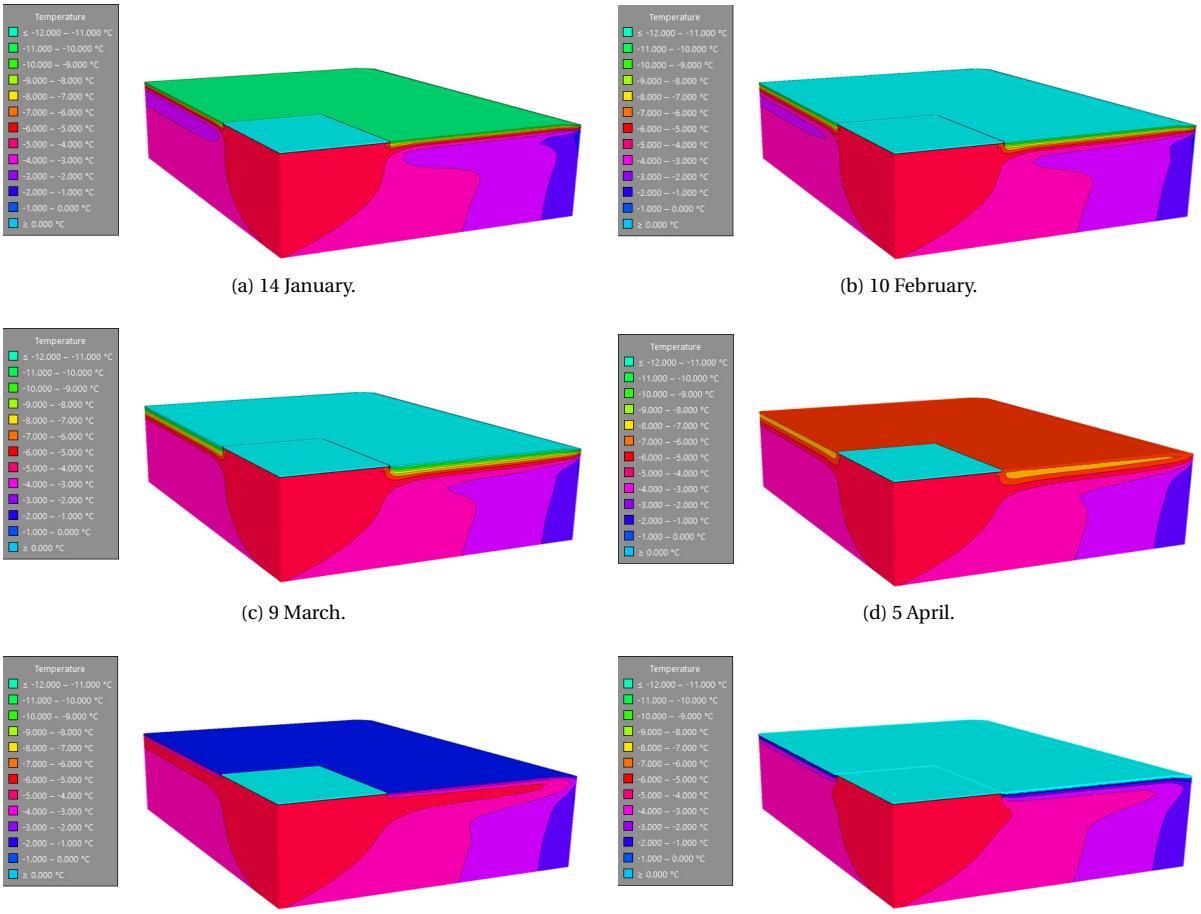

(a) 14 January.

(b) 10 February.

(c) 9 March.

(d) 5 April.

(e) 29 May.

(f) 25 June.

Figure B.10: Visualization of the temperature field at different points in time from January to June after 10 years of cooling at -5 °C.

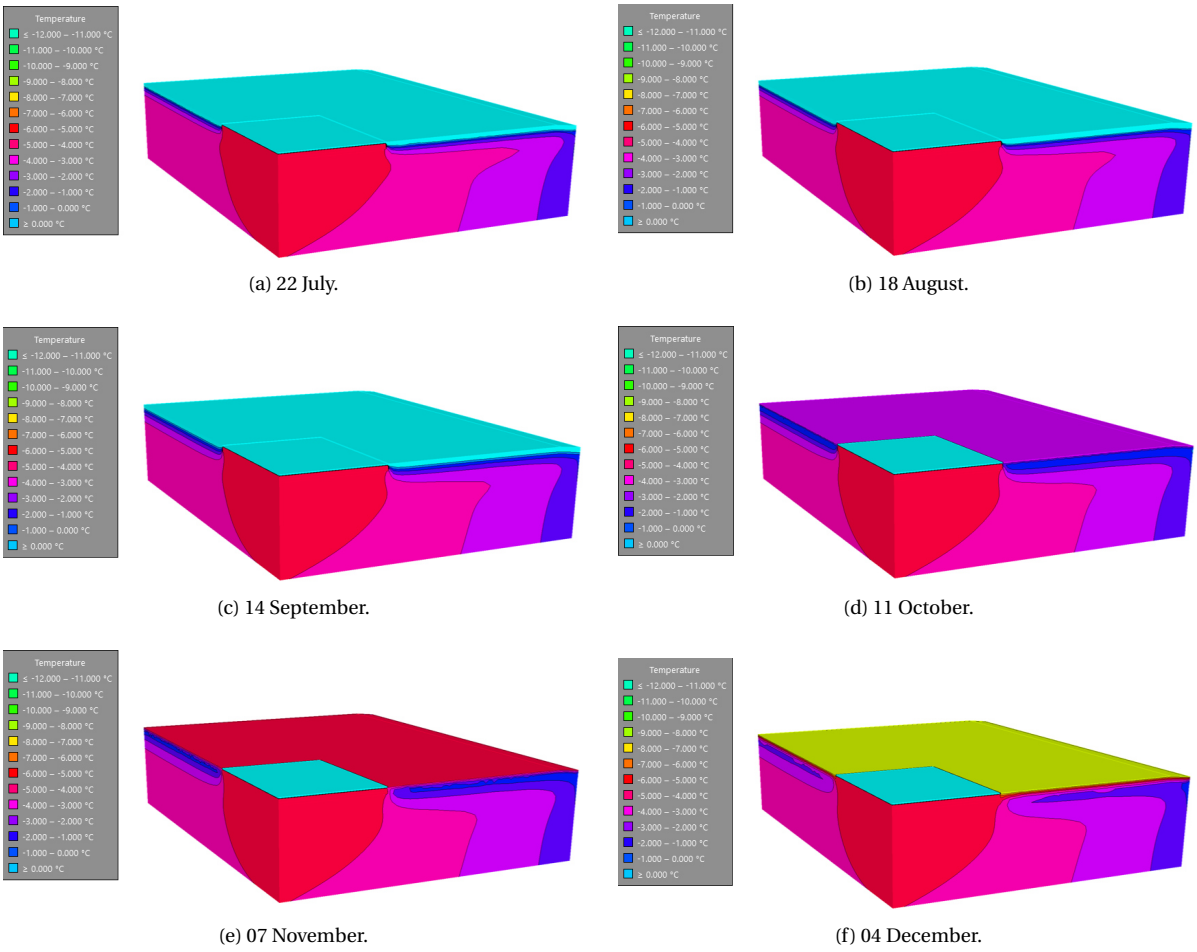

(a) 22 July.

(b) 18 August.

(c) 14 September.

(d) 11 October.

(e) 07 November.

(f) 04 December.

Figure B.11: Visualization of the temperature field at different points in time from July to December after 10 years of cooling at -5 °C.

Bibliography

Abu-Hamdeh, N. H. (2003). Thermal Properties of Soils as affected by Density and Water Content. *Biosystems Engineering*, 86(1):97–102.

AMAP (2021). Arctic Climate Change Update 2021: Key Trends and Impacts. Summary for Policy-makers. Report, Arctic Monitoring and Assessment Programme (AMAP).

Andersland, O. B. and Ladanyi, B. (2004). *Frozen Ground Engineering*. John Wiley and Sons Ltd, second edition.

BEWI (n.d.). Datasheet: XPS Extraordinary Insulation . Report.

Boeckh, P. and Wetzel, T. (2018). *Waermeuebertragung: Grundlagen und Praxis*. Springer-Verlag.

Brandl, H. (2013). Thermo-active Ground-Source Structures for Heating and Cooling. *Procedia Engineering*, 57:9–18.

Brown, J., Ferrians Jr, O. J., Heginbottom, J. A., and Melnikov, E. S. (1997). *Circum-Arctic map of permafrost and ground-ice conditions*. Circum-Pacific Map Series CP-45. Geological Survey in Cooperation with the Circum-Pacific Council for Energy and Mineral Resources, Washington, DC: U.S.

Brown, R. J. E. (1970). *Permafrost in Canada*. University of Toronto Press.

Brown, R. J. E. and Kupsch, W. O. (1974). Permafrost terminology. Report, National Research Council of Canada. Associate Committee on Geotechnical Research.

Burke, E. J., Zhang, Y., and Krinner, G. (2020). Evaluating permafrost physics in the Coupled Model Intercomparison Project 6 (CMIP6) models and their sensitivity to climate change. *The Cryosphere*, 14(9):3155–3174.

Burn, C. and Smith, C. (1988). Observations of the "Thermal Offset" in Near-Surface Mean Annual Ground Temperatures at Several Sites near Mayo, Yukon Territory, Canada. *ARCTIC*, 41.

Christiansen, H. H., Gilbert, G., Demidov, N., Guglielmin, M., Isaksen, K., Osuch, M., and Boike, J. (2019). Permafrost temperatures and active layer thickness in Svalbard during 2017/2018 (PermaSval). *Van den Heuvel et al. (eds): SESS report 2019, Svalbard Integrated Arctic Earth Observing System, Longyearbyen*, pages 237–249.

Clarke, E. S. (2007). Permafrost Foundation: State of the Practice. Report 0784409471, Technical Council on Cold Regions Engineering Monograph.

Dickie, G. (2021). The World's Northernmost Town Is Changing Dramatically. Available online: https://www.scientificamerican.com/article/the-worlds-northernmost-town-is-changing-dramatically/. Accessed on: 20 June 2021.

Esch, D. C. (2004). *Thermal Analysis, Construction, and Monitoring Methods for Frozen Ground*. American Society of Civil Engineers.

Farouki, Omar, T. (1981). The thermal properties of soils in cold regions. *Cold Regions Science and Technology*, 5(1):67–75.

Faste, A. H. and Moholdt, G. (2021). Merged NPI-ArcticDEM Svalbard digital elevation model. Available online: https://doi.org/10.21334/npolar.2020.a660ff0c. Accessed on: 01 April 2021.

Foerland, E., Benestad, R., Hanssen-Bauer, I., Haugen, J., and Engen-Skaugen, T. (2011). Temperature and Precipitation Development at Svalbard 1900–2100. *Advances in Meteorology*, 2011.

Francis, J. A., Vavrus, S. J., and Cohen, J. (2017). Amplified Arctic warming and mid-latitude weather: new perspectives on emerging connections. *WIREs Climate Change*, 8(5):e474.

French, H. M. (2007). *The Periglacial Environment*. John Wiley and Sons Ltd, 3 edition.

GEO-SLOPE International Ltd (2014). *Thermal Modelling with TEMP/W*. GEO-SLOPE International Ltd, Calgary, AB, Canada.

GeoPrecision (n.d.). THERMISTOR-STRING.COM. Available online: https://www.thermistor-string.com/. Accessed on: 20 May 2021.

GEOSLOPE International, Ltd. (2020). Heat and mass transfer modeling with GeoStudio 2020 (First Edition). Report, GEOSLOPE International, Ltd.

GeoStudio (n.d.). Example Files. Available online: https://www.geoslope.com/learning/support-resources/example-files?q=verification&v=11.1.0.00000. Accessed on: 12 June 2021.

Gjermundsen, A., Graff, L., Bentsen, M., Breivik, L., Debernard, J., Makkonen, R., Olivié, D., Seland, O., Zieger, P., and Schulz, M. (2021). How representative is Svalbard for future Arctic climate evolution? An Earth system modelling perspective (SvalCLIM). *Moreno-Ibáñez et al (eds) SESS report 2020, Svalbard Integrated Arctic Earth Observing System, Longyearbyen*, pages 38–59.

Goodrich, L. E. and Plunkett, J. C. (1990). Performance of heat pump chilled foundations. *Proceeding of the Fifth Canadian Permafrost Conference, Nordicana no54*, pages 409–418.

Hanssen-Bauer, I., Førland, E., Hisdal, H., Mayer, S., Sandø, A., Sorteberg, A., Adakudlu, M., Andresen, J., Bakke, J., Beldring, S., Benestad, R., van der Bilt, W., Bogen, J., Borstad, C., Breili, K., Breivik, O., Børsheim, K., Christiansen, H., Dobler, A., and Wong, W. (2019). Climate in Svalbard 2100. *A knowledge base for climate adaptation*.

Harris, S., Brouchkov, A., and Guodong, C. (2017). *Geocryology: Characteristics and Use of Frozen Ground and Permafrost Landforms (1st ed.)*. CRC Press.

Hartmann, D. L. (2015). *Global physical climatology*, volume 103. Newnes.

Hjort, J., Karjalainen, O., Aalto, J., Westermann, S., Romanovsky, V., Nelson, F., Etzelmüller, B., and Luoto, M. (2018). Degrading permafrost puts Arctic infrastructure at risk by mid-century. *Nature Communications*, 9.

Humlum, O., Instanes, A., and Sollid, J. (2003). Permafrost in Svalbard: A review of research history, climatic background and engineering challenges. *Polar Research*, 22:191–215.

Instanes, A. (2006). Impacts of a changing climate on Infrastructure: Buildings, Support Systems, and Industrial Facilities. In *2006 IEEE EIC Climate Change Conference*, pages 1–4.

Instanes, A. (2010). The development of infrastructure on permafrost in Svalbard. *Frost i Jord 2010*, page 13.

Instanes, A. (2016). Incorporating climate warming scenarios in coastal permafrost engineering design – Case studies from Svalbard and northwest Russia. *Cold Regions Science and Technology*, 131:76–87.

Instanes, A. and Anisimov, O. (2008). Climate Change and Arctic Infrastructure. In Kane, D. L. and Hinkel, K. M., editors, *Proceedings of the Ninth International Conference on Permafrost*, volume 1. Institute of Northern Engineering, University of Alaska Fairbanks.

Instanes, A. and Mjureke, D. (2005). Svalbard airport runway. Performance during a climate-warming scenario. *Proceedings of the international conferences on the bearing capacity of roads, railways and airfields*.

Instanes, A. and Rongved, J. L. (2009). Frysefundamentering på Svalbard - mer enn 20 års erfaringer (in Norwegian). In Kristiansen, J., Engen, A., Olsson, R., and Engen, S., editors, *Geoteknikkdagen*. Norsk Geoteknisk Forening.

Instanes, A. and Rongved, J. L. (2019). Climate change and geotechnical design in permafrost and frozen ground. *Proceedngs of the 17th European Conference on Soil Mechanics and Geitechnical Engineering*.

Instanes, B. (1988). Foundation Design on Permafrost with Heat Pumps. *Fifth International Conference Permafrost*, 3.

Instanes, B. and Instanes, A. (2008). Foundation Design Using a Heat Pump Cooling System. In *Proceedings of the Ninth International Conference on Permafrost*, volume 1. Institute of Northern Engineering, University of Alaska Fairbanks.

IPCC (2013). *Climate Change 2013: The Physical Science Basis. Contribution of Working Group I to the Fifth Assessment Report of the Intergovernmental Panel on Climate Change*. Cambridge University Press, Cambridge, United Kingdom and New York, NY, USA.

Jaroslav, O., Sebastian, W., Annett, B., Nikolai, B., Hanne, H. C., Avirmed, D., Reynald, D., Bo, E., Bernd, E., Alexander, K., Artem, K., Andreas, K., Marina, O. L., Antoni, G. L., Santosh, K. P., Vladimir, R., Robert, G. W., Andreas, W.-N., Tonghua, W., Jambaljav, Y., and Defu, Z. (2019). Northern Hemisphere permafrost map based on TTOP modelling for 2000-2016 at 1km2 scale. *Earth-Science Reviews*, 193:299–316.

Johansen, O. (1977). Thermal conductivity of soils. Report, Cold Regions Research and Engineering Lab Hanover NH.

Kersten, M. S. (1949). Thermal properties of soils, Engineering Experiment Station Bulletin 28. *University of Minnesota, Minneapolis, MN*.

Klene, A., Nelson, F., Shiklomanov, N., and Hinkel, K. (2001). The N-Factor in Natural Landscapes: Variability of Air and Soil-Surface Temperatures, Kuparuk River Basin, Alaska, U.S.A. *Arctic Antarctic and Alpine Research*, 33:140–148.

Lachenbruch, A. H. (1970). Thermal considerations in permafrost. *Proceedings of the Geological Seminar on the North Slope of Alaska*.

Linell, K. A. (1973). Long-term effects of vegetative cover on permafrost stability in an area of discontinuous permafrost. *Proceedings of Permafrost: North American contribution to the Second International Conference*, pages 688–693.

Longva arkitekter (n.d.). Ti ars arbeid bærer frukter. Available online: https://svalbardposten.no/ti-ars-arbeid-barer-frukter/19.11841. Accessed on: 22 March 2021.

Mathisen, G. (2020). Fryser bakken med grønn energi. Available online: https://nemitek.no/dag-arne-husdal-energisparing-svalbard/fryser-bakken-med-gronn-energi/139421. Accessed on: 17 April 2021.

Meyer, J., Pride, D., O'Toole, J., Craven, C., and Spencer, V. (2011). Ground-Source Heat Pumps in Cold Climates . Report, ACEP and CCHRC.

Midttoemme, K., Jochmann, M., Henne, I., Wangen, M., and Thomas, P. (2015). Is Geothermal Energy an Alternative for Svalbard? In *SES, The Third Sustainable Earth Science Conference & Exhibition*.

Molmann, T., Bergheim, B., and Valeriote, M. (1998). Svalbard airport geotechnical study: Engineering methodology and results. In *Seventh International Conference*, volume 5 of *Collection Nordicana*, pages 745–755.

Nord Pool (n.d.). Day-ahead prices. Available online: https://www.nordpoolgroup.com/Market-data1/Dayahead/Area-Prices/NO/Daily1/?view=table. Accessed on: 03 June 2021.

Norwegian Mapping Authority Kartverket (n.d.). Norgeskart. Available online: https://norgeskart.no/!?project=norgeskart&layers=1002&zoom=16&lat=8685465.80&lon=512314.92. Accessed on: 02 June 2021.

NSIDC (2020). Cryosphere Glossary. Available online: https://nsidc.org/cryosphere/glossary/term/frost-action. Accessed on: 10 March 2021.

Perlshtein, G. Z., Guly, S. A., and Buyskih, A. A. (2001). *Some prospects for heat pump applications in permafrost engineering*, volume 76 of *Permafrost Response on Economic Development, Environmental Security and Natural Resources*. Springer, Dordrecht.

QWare (n.d.). What Is A Ground Source Heat Pump? Available online: https://www.qwarecmms.com/files/theme/images/ground-source-heat-pump.jpg. Accessed on: 08 May 2021.

Ramage, J., Jungsberg, L., Wang, S., Westermann, S., Lantuit, H., and Heleniak, T. (2021). Population living on permafrost in the Arctic. *Population and Environment*, pages 1–17.

Regjeringen (2021). Ny energiloesning for Longyearbyen. Available online: https://www.regjeringen.no/no/aktuelt/ny-energilosning-for-longyearbyen/id2827886/. Accessed on: 01 July 2021.

Riseborough, D., Shiklomanov, N., Etzelmüller, B., Gruber, S., and Marchenko, S. (2008). Recent advances in permafrost modelling. *Permafrost and Periglacial Processes*, 19(2):137–156.

Romanovsky, V. E., Smith, S. L., and Christiansen, H. H. (2010). Permafrost thermal state in the polar Northern Hemisphere during the international polar year 2007–2009: a synthesis. *Permafrost and Periglacial Processes*, 21(2):106–116.

Rongved, J. L. and Instanes, A. (2012). Foundation Engineering in Svalbard, 1950-2012. In Hinkel, K. M., editor, *Tenth International Conference on Permafrost*, volume Volume 1: International Contributions, pages 341–346. The Northern Publisher.

Sargent, R. G. (2013). Verification and validation of simulation models. *Journal of Simulation*, 7(1):12–24.

Schaefer, K. (2021). Methane and Frozen Ground. Available online: https://nsidc.org/cryosphere/frozenground/methane.html. Accessed on: 8 May 2021.

SCS Technical Committee on Model Credibility (1979). Terminology for model credibility. *SIMULATION*, 32(3):103–104.

Sheshpari, M. and Khalilzad, S. (2016). A Review on Permafrost Geotechnics, Foundation Design And New Trends. *International Journal of Research in Engineering and Science*, 4:59–71.

Shur, Y. and Goering, D. (2009). *Climate Change and Foundations of Buildings in Permafrost Regions*, volume 16 of *Permafrost Soils*. Springer, Berlin.

Shur, Y. and Slavin-Borovskiy, V. (1993). N-factor maps of Russian permafrost region. *Proceedings of the Sixth International Conference on Permafrost*, 2:564–568.

Singh, R. M., Sani, A. K., and Amis, T. (2019). *An overview of ground-source heat pump technology*. Managing Global Warming, An Interface of Technology and Human Issues. Academic Press.

Skogseth, R., Olivier, L. L. A., Nilsen, F., Falck, E., Fraser, N., Tverberg, V., Ledang, A. B., Vader, A., Jonassen, M. O., Søreide, J., Cottier, F., Berge, J., Ivanov, B. V., and Falk-Petersen, S. (2020). Variability and decadal trends in the Isfjorden (Svalbard) ocean climate and circulation – An indicator for climate change in the European Arctic. *Progress in Oceanography*, 187.

Smith, D. W. (1996). *Cold Regions Utilities Monograph*. American Society of Civil Engineers.

Smith, S. L., Burgess, M. M., Riseborough, D., and Mark Nixon, F. (2005). Recent trends from Canadian permafrost thermal monitoring network sites. *Permafrost and Periglacial Processes*, 16(1):19–30.

Statistics Norway (n.d.). Population of Svalbard. Available online: https://www.ssb.no/en/befolkning/folketall/statistikk/befolkningen-pa-svalbard. Accessed on: 06 June 2021.

Statsbyg (n.d.). Svalbard globale froehvelv. Available online: https://www.statsbygg.no/prosjekter-og-eiendommer/svalbard-globale-frohvelv. Accessed on: 10 May 2021.

Stenbeak-Nielson, H. C. and Sweet, L. R. (1975). Heating with ground heat: an energy saving method for home heating. *The Northern*, 7(1):20–25.

Swenson, H. A. and Baldwin, H. L. (1965). A primer on water quality. Report, USGS.

Thacker, B., S.W.Doebling, Hemez, F., Anderson, M., Pepin, J. E., and Rodriguez, E. (2004). Concepts of Model Verification and Validation (No. LA-14167). *Los Alamos National Lab., Los Alamos, NM (US)*.

The Norwegian Meteorological Institute (MET Norway) (n.d.). Available online: https://seklima.met.no/observations/. Accessed on: 01 March 2021.

Tian-fei, H. and Zu-run, Y. (2021). Potential applications of solar refrigeration systems for permafrost cooling in embankment engineering. *Case Studies in Thermal Engineering*, 26.

Tice, A. R., Anderson, D. M., and Banin, A. (1976). *The prediction of unfrozen water contents in frozen soils from liquid limit determinations*. Department of Defense, Army, Corps of Engineers, Cold Regions Research and Engineering Laboratory.

Van Huissteden, J. (2020). *Thawing Permafrost*. Springer International Publishing.

VDI (2019). VDI 4640 Blatt 2. Thermal use of the underground - Ground source heat pump systems. Report, Engl. VDI-Gesellschaft Energie und Umwelt.

Vieira, A., Alberdi-Pagola, M., Christodoulides, P., Javed, S., Loveridge, F., Nguyen, F., Cecinato, F., Maranha, J., Florides, G., Prodan, I., Van Lysebetten, G., Ramalho, E., Salciarini, D., Georgiev, A., Rosin-Paumier, S., Popov, R., Lenart, S., Erbs Poulsen, S., and Radioti, G. (2017). Characterisation of Ground Thermal and Thermo-Mechanical Behaviour for Shallow Geothermal Energy Applications. *Energies*, 10(12).

Williams, P. J. and Smith, M. W. (1989). *The Frozen Earth: Fundamentals of Geocryology*. Studies in Polar Research. Cambridge University Press, Cambridge.

Zarling, J. P. and Yarmak, E. (2007). Refrigerated Foundations. In *Permafrost Foundation: State of the Practice*, pages 65–82. ASCE.

Zhang, G. and Horne, W. T. (2012). Thermal design of shallow building foundations in permafrost regions. *Proceedings of the International Conference on Cold Regions Engineering*, pages 337–347.

Sarah Theresa Heller

NTNU
Norwegian University of
Science and Technology

DTU Cold Climate Engineering
UNIS